

Alma Mater Studiorum – Università di Bologna

DOTTORATO DI RICERCA IN

Meccanica e Scienze Avanzate dell'ingegneria

Ciclo XXVII

Settore Concorsuale di afferenza: 09/A1

Settore Scientifico disciplinare: ING-IND/04

**EFFECT OF LASER SHOCK PEENING ON FATIGUE CRACK
PROPAGATION OF AERONAUTICAL STRUCTURES**

Presentata da: Sara TADDIA

Coordinatore Dottorato

Relatore

Prof. Vincenzo PARENTI CASTELLI

Prof. Enrico TROIANI

Esame finale anno 2015

Alla mia famiglia

Contents

Contents	ii
List of Figures	v
List of Tables	xii
1 Introduction to Fatigue	1
1.1 Fatigue Design Overview	1
1.2 Introduction to Fatigue	3
1.3 Linear Elastic Fracture Mechanics	5
1.4 Crack in stress Field: Plane stress and Plane Strain conditions	7
1.5 Crack Tip Evaluation	8
1.6 Fracture Toughness	8
1.7 Crack Growth description	9
1.8 Crack Growth Analytical Predictions	11
1.9 Threshold and overload plasticity affecting the growth	12
1.9.1 Center Cracked Panel	14
1.9.2 Edge Cracked Panel	14
1.10 Plastic Zone arising at crack tip	17
1.11 Effect of Residual Stresses on Crack Growth	20
Bibliography	24
2 Laser Shock Peening	25
2.1 Laser Physics	25
2.1.1 Laser Components	26
2.2 The photon emission process	28
2.2.1 Q-Switching	28
2.2.2 Solid State Lasers	28
2.3 Laser Shock Peening	28
2.3.1 Laser Systems	30
2.3.2 Opaque Overlay	30
2.3.3 Transparent overlay	31

2.4 Motivation	36
Bibliography	37
3 LSP Numerical Simulations	39
3.1 Laser Peening Treatment	39
3.2 Comparison with Shot Peening	39
3.3 LSP Numerical Modeling	40
3.4 Existing Models for LSP Numerical Simulation	42
3.4.1 Explicit/Implicit LSP Analysis	42
3.4.2 ShockLas Prediction Tool	43
3.5 Johnson-Cook Modeling Technique	44
3.6 Eigenstrain Method	77
3.7 Kinematic Hardening	84
3.8 Conclusions	90
Bibliography	92
4 Afgrow Fatigue Life prediction	94
4.1 Afgrow Software	94
4.2 Geometry of the analyzed configurations	94
4.3 Implemented loading condition	95
4.4 Material description	95
Bibliography	107
5 Analytical Fatigue Life Prediction	108
5.1 Introduction	108
5.1.1 Geometry definition and experimental procedure	108
5.1.2 Parametric analysis on geometric parameters influence	112
5.1.3 Conclusions	112
Bibliography	114
6 RS measurement	116
6.1 Measurement Techniques	116
6.1.1 Residual Stress	116
6.1.2 Contour Method	117
6.1.3 Incremental Hole Drilling	118
6.1.4 Neutron Diffraction Method	120
6.1.5 X-Ray Diffraction Method	124
6.2 Material characterization	129
Bibliography	132
7 Experimental RS measurements by XRD	133
7.1 X-Ray Diffraction Measurement Technique	133
7.2 Comparison between different laser set up parameters	142
Bibliography	153

8 Analytical Fatigue Predictions	154
Bibliography	171
9 Friction Stir Welding	172
9.1 Welded joints	172
9.2 Background	173
9.3 Analytical Model	174
9.4 Output parameters and Comparison with the Experimental Results	175
Bibliography	177
Bibliography	178
10 LSP in LEAF	179
10.1 Introduction	179
Bibliography	193
11 Conclusions	195
11.1 Conclusions	195
Bibliography	197
11.2 Metallography	198
11.3 Microstructure in Aluminum Alloys	199
11.3.1 Specimen Preparation	199
11.4 Hardness and Roughness Coupon Characterization	204
11.4.1 Testing Procedure: hardness	204
11.4.2 Roughness	206
Bibliography	208

List of Figures

1.1	Milestone case histories in aircraft structural integrity	1
1.2	Summary of accidents and design developments for civil and military aircraft	2
1.3	What is Fatigue	3
1.4	S N Curve	3
1.5	S-N Curve example varying with R	4
1.6	Different Phases of Fatigue Life	4
1.7	Crystallographic aspects regarding fatigue	5
1.8	Stress Flow around a Crack	6
1.9	Stress Field around a crack Tip	8
1.10	Fracture Toughness dependence on the coupon thickness	9
1.11	Fracture Toughness dependence on the coupon machining and crack orientation	9
1.12	Crack Growth Rate against the Stress Intensity Factor	10
1.13	Plastic Zone at Crack Tip at 180 MPa	12
1.14	Plastic Zone at Crack Tip at 90 MPa	13
1.15	Specimen Configuration	13
1.16	Short Crack Behaviour vs Long Cracks one	14
1.17	Centre Cracked Panel	15
1.18	Edge Crack configuration	15
1.19	Stress acting on a fuselage	16
1.20	Plastic Zone at Crack Tip	17
1.21	Energy Balance between K and R	18
1.22	R-curve in plane stress and plane strain	18
1.23	RS measured at Elettra at 18KeV in LSPeened panel	19
1.24	Plastic Zone LSPeened symmetric Configuration	19
1.25	Plastic Zone of Crack approaching an Asymmetric laser parren .	20
1.26	main parameters involved in each fatigue life period	20
1.27	crack initiation and growth	21
1.28	crack initiation and growth on S-N curve	21
2.1	Laser Components	26

2.2	Laser Working Principle 1	26
2.3	Laser Working Principle 2	27
2.4	Laser Working Principle 3	27
2.5	Laser scanning and stepping directions	34
3.1	Braisted and Brockman LSP numerical procedure	42
3.2	Shocklas Scheme	44
3.3	Partition and Overlap adopted for a tested laser peening configuration	45
3.4	Laser Pulse temporal profile	47
3.5	Laser pressure profile, numerical shape adopted	47
3.6	Single Peen geometry used for mesh sensitivity studies	49
3.7	Stress-Strain Curve for JC parameters found in the literature vs new for curve continuity	50
3.8	Shock Wave Profile found in the literature	51
3.9	Pressure temporal profile	52
3.10	Relation between laser power and pressure loading	52
3.11	BCs in relaxation step	53
3.12	Specimen Geometry, Single Central Shot	53
3.13	Residual stress at top and bottom ablative layer surfaces	54
3.14	displacement parameter evaluated at top and bottom ablative layer surface	54
3.15	Peeq at top and bottom ablative layer surfaces	55
3.16	Elpd evaluated on top and bottom ablative layer surfaces	55
3.17	Procedure to evaluate the temperature effect	56
3.18	Johnson - Cook influencing parameters	56
3.19	Numerically implemented pressure pulse profile	56
3.20	Temperature on front and back ablative layer surface	57
3.21	Temperature on top and back ablative layer surface	57
3.22	Temperature on top and back ablative layer surface at 6e-07	57
3.23	Temperature on top and back ablative layer surface at 2.5e-04	58
3.24	temperature on top and back of the ablative layer surface at the end of the analysis, relax step	58
3.25	Temperature evolution on the so called 'main 'coupon part	58
3.26	Displacement evolution on the ablative layer top surface	59
3.27	Displacement at back ablative layer surface	59
3.28	Specimen displacement evolution on main coupon part	59
3.29	Comparison between the displacement parameter on main coupon part with experimental results	60
3.30	Residual stress achieved on main coupon part compared to the experimental results	60
3.31	Displacement evolution on main specimen part	60
3.32	ALLIE energy	61
3.33	ALLKE energy	61
3.34	ALLPD	61
3.35	Loading Distribution	64
3.36	BCs Relax Step	64
3.37	Shooting Configuration, 3 layers, geometry	65
3.38	Shooting sequence, 3 layers as coverage	66
3.39	Shooting geometry, 4 layers coverage	66

3.40	Shooting sequence, 4 layer coverage	67
3.41	Shooting geometry, 5 layers as coverage	67
3.42	Shooting sequence, 5 layers coverage	67
3.43	Residual stress measurement paths	68
3.44	residual stress field achieved for different laser setting parameters on 6 mm coupon thickness	68
3.45	Residual Stress on 6 mm thick coupon, 4 layers coverage	68
3.46	Residual Stress on 6 mm thick coupon, 5 layers coverage	69
3.47	Residual stress on 6 mm thick coupon, 2 GW/cm ²	69
3.48	Residual stress on 6 mm thick coupon, 3GW/cm ²	69
3.49	Residual stress on 6 mm thick coupon, 4GW/cm ²	70
3.50	Residual stress on 6 mm thick coupon, 5GW/cm ²	70
3.51	Residual stress field on 6 mm thick coupon aside the laser shot	70
3.52	residual stress on 6 mm thick coupon, along specimen width	70
3.53	Residual stress on 8 mm thick coupon, 3 layers	70
3.54	Residual stress on 8 mm thick coupon, 4 layers coverage	71
3.55	Residual stress on 8 mm thick coupon, 5 layers coverage	71
3.56	residual stress on 8 mm thick coupon, 2 GW/cm ²	71
3.57	Residual stress on 8 mm thick coupon, 3 GW/cm ²	72
3.58	residual stress on 8 mm thick coupon, 4 GW/cm ²	72
3.59	residual stress on 8 mm thick coupon, 5 GW/cm ²	72
3.60	Residual stress on 12.5 mm thick coupon, 3 layers coverage	73
3.61	Residual stress on 12.5 mm thick coupon, 4 layers coverage	73
3.62	Residual stress on 12.5 mm thick coupon, 5 layers coverage	73
3.63	residual stress on 12.5 mm thick coupon, 2 GW/cm ²	74
3.64	residual stress on 12.5 mm thick coupon, 3 GW/cm ²	74
3.65	residual stress on 12.5 mm thick coupon, 4 GW/cm ²	74
3.66	residual stress on 12.5 mm thick coupon, 5 GW/cm ²	74
3.67	Eigenstrain Method	77
3.68	Eigenstrain procedure	77
3.69	Partition adopted for Eigenstrain Method application	79
3.70	Strain Components achieved via Explicit Analysis to be used as input in subsequent Standard Analysis	81
3.71	Example of strain values to be used as input in the Standard Analysis, each attributed to the proper partition level	82
3.72	Residual Stress comparison between JC with Ablative Layer and Eigenstrain approach	82
3.73	Displacement Eigenstrain vs Experimental	83
3.74	Temperature Profile Eigenstrain Analysis	83
3.75	kinematic hardening model with three back-stresses	86
3.76	cyclic hardening with plastic shakedown	87
3.77	Residual Stress comparison between JC and KH approach	89
3.78	Through the thickness residual stress comparison between JC and KH approach	89
3.79	Displacement parameter, comparison between the KH and JC approach	89
4.1	Afgrow Standard crack Solutions: Internal Through crack	95
4.2	tabular look-up data for Al 2024-T351	96
4.3	baseline validated result for Al 2024-T351	96

4.4	Residual stress definition within Afgrow	98
4.5	Model for SIF evaluation	98
4.6	Available Weight Function	99
4.7	Specimen Configuration involving four 5 mm laser stripes	99
4.8	residual stress configuration for specimen characterized by 5 mm width laser stripes	100
4.9	Improvement in fatigue life with 5 mm stripes on 400*160*2 mm coupon	100
4.10	Specimen configuration characterized by 10 mm wide laser stripes	101
4.11	Stress configuration adopted for coupon characterized by 10 mm wide stripes	101
4.12	Crack Growth improvement for configuration based on 10 mm wide stripes	102
4.13	Specimen 400*800*2 mm, with 5 mm wide laser stripes	102
4.14	Residual stress in 400*800*2 mm coupon, laser stripes 5 mm wide	102
4.15	fatigue life improvement for coupon configuration 400*800*2 mm	103
4.16	Specimen configuration 400*800*2 mm, laser patterns 10 mm wide	103
4.17	Residual stress inserted in coupon 400*800*2 mm, laser stripes 10 mm wide	104
4.18	Crack growth improvement for coupon 400*800*2 mm, laser stripes 10 mm wide	104
4.19	Specimen configuration 400*800*2 mm, laser stripes 20 mm wide	104
4.20	Residual stress field in 400*800*2 mm coupon geometry, laser stripes 20 mm wide	105
4.21	Crack growth benefit in 400*800*2 mm coupon, laser stripes 20 mm wide	105
5.1	FCP specimen configuration	109
5.2	Fatigue Life, Paris Curve; experimental LSP coupon vs Baseline	109
5.3	non dimensional a/N curves, compared with baseline.	110
5.4	Numerical and analytical evaluation of Residual Stress Field . . .	111
5.5	Effect due to LSP, comparison between the test results and the analitical evaluations	111
5.6	Fatigue Life Estimation with Terada and Tada modeling technique	113
6.1	residual stress are linked to crystal lattices distances	117
6.2	Contour Method Principle	118
6.3	Electrical Discharge Machining	118
6.4	Incremental Hole Drilling	119
6.5	Bragg's Law Principle 1	120
6.6	Bragg's Law Principle 2	121
6.7	Bragg's Law 3	121
6.8	Bragg's Law Principle 4	121
6.9	Counts	122
6.10	Lattice Planes reflecting neutrons	123
6.11	Nuclear Reactor Working Principle	123
6.12	Young modulus associated with corresponding lattice plane in aluminum	123
6.13	Surface X-Ray parameters	124
6.14	residual Stress X-Ray calculations	124

6.15	Synchrotron X-Ray radiation	125
6.16	Electrons in a synchrotron	125
6.17	Synchrotron Gauge Volume	126
6.18	Residual Stress measurement optical system in devoted beam . .	126
6.19	Peak Choice	126
6.20	Bragg's Law Parameters	127
6.21	Diffractometer	128
6.22	Young Modulus definition	129
6.23	Force Distance curve for two materials, difference in the elastic modulus	130
6.24	Cubic Crystal System	130
6.25	Miller Indices, eg.	130
7.1	Parameters for X-Ray Diffraction of aluminum alloys	134
7.2	Residual Stresses measured are perpendicular to the hitting X-Ray beam	136
7.3	Finding the zero θ position	137
7.4	Peak Location	137
7.5	Coupon alignment	139
7.6	Coupon in measurement location, 1	139
7.7	coupon in measurement location, 2	140
7.8	Elettra in Basovizza	140
7.9	Elettra Synchrotron	140
7.10	Elettra, residual stress measurement beam	141
7.11	fixing the coupon	141
7.12	fixing the coupon, 2	141
7.13	Angles involved in X-Ray measurements	142
7.14	Specimen Configuration	143
7.15	Residual Stress Summary at 12 KeV	143
7.16	Residual Stress Plot at 12 KeV	144
7.17	Residual stress Summary at 15 KeV	144
7.18	residual stress Plot at 15 KeV	144
7.19	Residual Stress Summary at 18 KeV	144
7.20	Residual Stress plot at 18 KeV	145
7.21	Laser Geometry Effect, 15 KeV	145
7.22	Laser Pattern Distance from Edge Effect, 15 KeV	146
7.23	Laser Pattern Width Effect, 15 KeV	146
7.24	Coverage Effect, 15 KeV	147
7.25	Coverage Effect, 18 KeV	147
7.26	Laser power Effect, 15 KeV	148
7.27	Laser Power Effect, 18 KeV	148
7.28	Single Side Shot vs Double Side Shot Configuration, 15 KeV . .	149
7.29	measurement points on WITS coupon	150
7.30	measurements points on UPM coupon, front side	150
7.31	measurement point on the UPM coupon, back side	150
7.32	Residual Stress achieved at UPM vs Residual Stress achieved at WITS, 15 KeV	151
8.1	LSP configurations tested at 12KeV, 0.004 mm depth, thickness .	154
8.2	Edge Crack configuration	155

8.3	Residual Stress achieved by each LSP configuration tested at 12 KeV	155
8.4	Beta Factor, configuration number 23, 12 KeV energy level . . .	155
8.5	SIF, configuration 23, 12 KeV	156
8.6	Paris Curve, configuration 23, 12 KeV	156
8.7	a N Curve, configuration 23, 12 KeV	156
8.8	rs 21	158
8.9	beta 21	158
8.10	sif 21	158
8.11	paris 21	159
8.12	an 21	159
8.13	3 rs	160
8.14	beta 3	160
8.15	sif 3	160
8.16	3 paris	161
8.17	3 an all	161
8.18	3 an part	162
8.19	rs 11	163
8.20	beta 11	163
8.21	sif 11	163
8.22	an 11	163
8.23	19 rs	164
8.24	19 beta	164
8.25	19 sif	165
8.26	19 paris	165
8.27	19 an all	165
8.28	19 an part	166
8.29	rs 17	167
8.30	17 beta	167
8.31	17 sif	167
8.32	17 paris	168
8.33	17 an	168
9.1	possible defects in welding	172
9.2	residual stress induced by welding	172
9.3	Symmetric Crack Configuration	173
9.4	Eccentric Crack Configuration	173
9.5	Investigated Configuration	174
9.6	Residual Stress Distribution for FSW, LSP, FSW plus LSP as estimated by the model	175
9.7	Stress Intensity Factor, comparison between the baseline and the predicted one	176
9.8	Paris Curve	176
9.9	Fatigue Crack Propagation Rate	176
10.1	Deformation of the plastic zone for thick and thin panels	181
10.2	Crack Propagation Mechanism	182
10.3	SIF vs time	183
10.4	Fatigue crack propagation rate vs SIF (double logarithmic scale)	183
10.5	Stress distribution between skin and stiffeners	184

10.6 Fuselage stress components; hoop plus bending	186
10.7 Typical fuselage damage scenarios	186
10.8 LEAF investigated damage scenarios	186
10.9 Stiffened panel with crack propagating beyond broken stringer; (a) sketch, (b) modeled loading condition	187
10.10 Reaction forces directions for intact and broken stiffeners	188
10.11 Secondary bending effect due to stiffeners eccentricity	190
10.12 LEAF logo	191
10.13 LEAF interface, including LSP treatment	191
11.1 Baseline coupons, analyzed views, top, side, plane	198
11.2 Scanning and stepping configurations analyzed	198
11.3 Acid effect on coupon	202
11.4 Optics measurement reference	202
11.5 Grains measure at 20x for Al 2024-T351, untreated area	202
11.6 Elongated grains in untreated Al 2024-T351 coupon, 10x optic	203
11.7 Grains shape outside the treated area, 20x	203
11.8 Grains shape aside the laser shot, 20x optics	203
11.9 Grains shape of laser peened area, 20x	204
11.10 Vickers Test Principle	205
11.11 Vickers Testing Machine at Lab	205
11.12 Coupon devoted to Vickers Test	206
11.13 Vickers measurement	206
11.14 Laser Scanning and Stepping direction definition	207

List of Tables

3.1	Numerical Parameters adopted in the first modeling attempt . .	48
3.2	JC parameters, Al 7050-T7451	48
3.3	JC parameters, Al 7050-T7451, continuous stress-strain curve . .	50
3.4	JC parameters, Al 7050-T7451	63
3.5	JC parameters, Ablative	64
3.6	Investigated Configurations	65
3.7	Investigated Configurations	66
3.8	Investigated Configurations	66
3.9	Residual Stress field achieved on 6 mm thick coupon	75
3.10	Residual Stress field achieved on 8 mm thick coupon	75
3.11	Residual Stress field achieved on 12.5 mm thick coupon	76
3.12	Summary of the more compressive and deeper residual stresses achieved	76
3.13	Amplitude Definition	80
3.14	KH parameters, Al 7050-T7451, 1 back-stress	88
3.15	KH parameters, Al 7050-T7451, 3 back-stress, plastic	88
3.16	KH parameters, Al 7050-T7451, 3 back-stress, cyclic hardening .	88
4.1	Geometry configurations investigated via Afdrow Software	94
4.2	Experimental values of da/dN and ΔK used for simulations . . .	97
5.1	Percentage variation of the fatigue life referred to the baseline, laser pattern 10 mm	112
5.2	Percentage variation of the fatigue life referred to the baseline, laser pattern 33 mm	112
6.1	Residual Stress Technique	117
6.2	Pro and Cons of Contour Method	118
6.3	Pro and Cons of Incremental Hole Drilling	119
6.4	Pro and Cons of air abrasive jet machining	120
6.5	Pro and Cons of Nuclear reactor source and Spallation Source . .	122
6.6	Pro and Cons X-Ray Diffraction Method	128

8.1	Coupon 23 Laser Set up Parameters	157
8.2	Coupon 21 Laser Set up Parameters	157
8.3	Coupon 3 Laser Set up Parameters	162
8.4	Coupon 11 Laser Set up Parameters	162
8.5	Coupon 19 Laser Set up Parameters	166
8.6	Coupon 17 Laser Set up Parameters	166
8.7	Comparison on fatigue performance between coupons 23 and 21, 12 KeV	169
8.8	Comparison on fatigue performance between coupons 3 and 11, 15 KeV	169
8.9	Comparison on fatigue performance between coupons 19 and 17, 18 KeV	169
9.1	FSW Al 7075-T7351	174
11.1	Sanding paper used for side and top view coupons	200
11.2	Polishing steps	201

Abstract

Laser Shock Peening (LSP) is a surface enhancement treatment which induces a significant layer of beneficial compressive residual stresses up to several mm underneath the surface of metal components in order to improve the detrimental effects of crack growth behavior rate in it.

The aim of this thesis is to predict the crack growth behavior of thin Aluminum specimens with one or more LSP stripes defining a compressive residual stress area. The LSP treatment has been applied as crack retardation stripes perpendicular to the crack growing direction, with the objective of slowing down the crack when approaching the LSP patterns.

Different finite element approaches have been implemented to predict the residual stress field left by the laser treatment, mostly by means of the commercial software Abaqus/Explicit.

The AFGROW software has been used to predict the crack growth behavior of the component following the laser peening treatment and to detect the improvement in fatigue life comparing to the specimen baseline.

Furthermore, an analytical model has been implemented on the Matlab software to make more accurate predictions on fatigue life of the treated components.

An educational internship at the Research and Technologies Germany- Hamburg department of Airbus helped to achieve knowledge and experience to write this thesis.

The main tasks of the thesis are the following:

- To up to date Literature Survey related to laser shock peening in metallic structures
- To validate the FE models developed against experimental measurements at coupon level
- To develop design of crack growth slow down in centered and edge cracked tension specimens based on residual stress engineering approach using laser peened patterns transversal to the crack path
- To predict crack growth behavior of thin aluminum panels
- To validate numerical and analytical results by means of experimental tests

CHAPTER 1

Introduction to Fatigue

1.1 Fatigue Design Overview

Among the design processes that affect aircraft structural integrity, fatigue is a very important area of concern. Fatigue is a process of progressive permanent structural material damage, where a component is subjected to repeated cyclic stresses associated with operating loads. Therefore it is a failure mode that occurs as a result of large number of load cycles. The history of engineering structures has been marked by several fatigue failures, however the connection between the cyclic loading and the failure was noted only in 19th century, when for the first time the failure mechanism was named material fatigue. In this period noteworthy engineering research and experimental works were done by August Wohler who was investigating the fatigue failure in railroad axles for the German Railway Industry. In particular, in the Aeronautic world, the happening of serious accidents caused by fatigue failure influenced the development of new design methods. This case histories and their influence can be found in the following ?? and ??:

<i>year</i>	<i>aircraft failure</i>	<i>influence, follow-up</i>
1954	DeHavilland Comet; two aircraft crashed owing to fuselage explosions.	General awareness of finite aircraft fatigue life as an important issue for passenger safety. Attention drawn to full-scale fatigue testing.
1969	F-111; wing failure due to undetected material flaw.	Aircraft should be damage tolerant. Fatigue cracking due to initial damage should be considered.
1977	Boeing 707; tailplane lost owing to fatigue failure in spar.	Old aircraft become more fatigue-critical, <i>geriatric aircraft</i> .
1988	Boeing 737; aircraft lost part of fuselage skin structure owing to multiple fatigue cracks in spar splices.	Multiple Site fatigue Damage (MSD) can occur in <i>ageing aircraft</i> , especially in lap joints of the pressurized structure.

Figure 1.1: Milestone case histories in aircraft structural integrity

1.1. FATIGUE DESIGN OVERVIEW

Accidents	Design developments	
1950s 1954 Comet fuselage failures - design details ; stress concentrations 1960s 1969 F111 wing pivot failure- manufacturing defects 1970s 1976 H-S748 wing failure 1977 B 707 stabiliser 1979 DC10 Chicago 1980s 1988: Aloha airlines loses most of upper fuselage in flight due to widespread and multiple site fatigue damage 1990s	Civil aircraft Safe Life 1959: first directives on fail safe aircraft design Safe life design continues as an option together with fail safe 1980 recommendations for damage Tolerance for large civil aircraft 1978, 1981 Introduction of supplemental inspections for ageing aircraft Post 1988 Major investigations and recommendations for inspection, maintenance and repair of ageing aircraft Continued investigations into ageing aircraft fatigue, corrosion and fracture behaviour 1990s Gradual elimination of safe life parts from large civil aircraft, In 2005, only the Undercarriage and engines remain Safe life Attempts to require that civil helicopters become damage tolerant	Military Aircraft Safe Life Safe life continues as an option 1974: MIL A-83444 Damage tolerance plus fail- safe for USAF; Europe continues with Safe life

Figure 1.2: Summary of accidents and design developments for civil and military aircraft

The above mentioned design philosophies can be summarized in three main approaches.

- Safe Life approach. Is the first design philosophy developed in early 1950s, sometimes called also finite life. With this approach, in fact, the structure is supposed to be crack free and the estimation of the whole life of an aircraft is to be based on the component with lowest fatigue life.
- Fail safe approach. This design philosophy arose in late 1950s after the Comet accident happened in 1954. The design assumption is that failure will eventually occur but when it does the device, system or process will fail in a safe manner. In other words, with this philosophy, an aircraft is designed to have an adequate life free from damage but operation is permitted even beyond the life at which such damage may develop. This is usually obtained by applying redundancy of structural members and granting load transfer capability.
- Damage tolerance approach. This concept was introduced in late 1970s to ensure aircraft structural integrity. The fundamental difference from the other approaches is that, with this philosophy small cracks and flaws are supposed to be already present in the structures as manufactured and they can propagate during the operating life. To implement the damage tolerance concept it is therefore essential to clearly define parameters like initial crack lengths and inspection periods. Components must be accessible for inspections without dismantling and an accurate inspection plan must be assessed. Moreover crack growth rate and residual strength in the presence of long cracks calculations are needed. Another key-point of this philosophy is the opportunity to consider crack arrest or retardation

1.2. INTRODUCTION TO ~~FATIGUE~~ CHAPTER 1. INTRODUCTION TO FATIGUE

and the related strategy to realize them, like, for example, application of compressive residual stresses. This approach is currently used in civil aircraft design.

1.2 Introduction to Fatigue

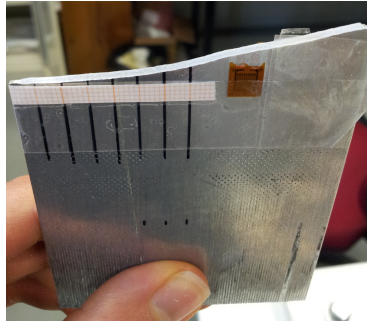


Figure 1.3: What is Fatigue

Picture ?? shows a coupon loaded in tension, which after carrying hundreds of cycles to fatigue resulting in flat shiny surfaces of the growing crack, failed statically in tension, thus reporting two opaque 45 degrees crack surfaces.

Fatigue phenomenon is initiated under cyclic loading at stress levels below the monotonic failure stress and results in permanent structural deformations, less load bearing capability and may lead to failure. An aspect to be taken into account is that fatigue has economic consequences that is:

- inspection, repair, replacement
- finding replacement items during unavailability
- avoiding fatigue failure on similar items

An important parameter involved in fatigue phenomena is the loading ratio, which is define as:

$$R = \frac{\sigma_{min}}{\sigma_{max}} \quad (1.1)$$

The fatigue performance can be evaluated by means of the S-N curve, that is applied load vs cycles to fatigue ?? and ??

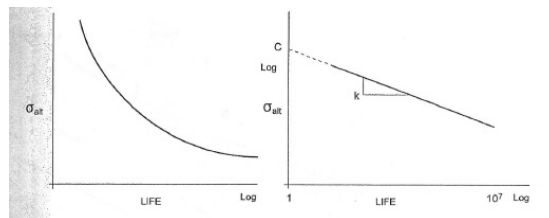


Figure 1.4: S N Curve

1.2. INTRODUCTION TO CHAPTER 1. INTRODUCTION TO FATIGUE

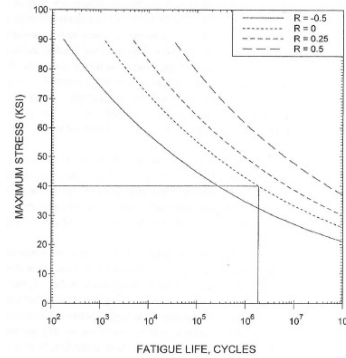


Figure 1.5: S-N Curve example varying with R

S-N curve summarizes Wohler's law, that is:

‘material can be induced to fail by many repetitions of stresses, all of which are lower than the static strength. The stress amplitudes are decisive for the destruction of the cohesion of the material. The maximum stress is of influence only in so far as the higher it is, the lower are the stress amplitudes which lead to failure. ’

Different phases can be found in fatigue life, that is ??:

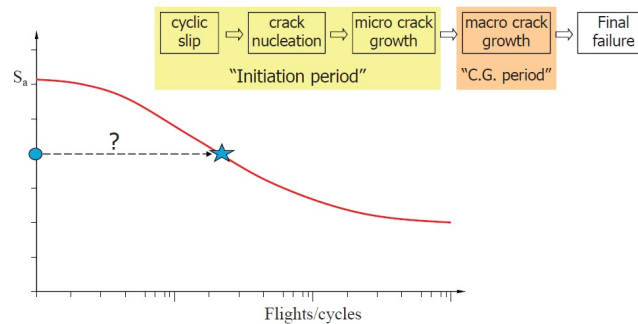


Figure 1.6: Different Phases of Fatigue Life

Attention must be paid that the S-N curve comprises also the initiation of damage. This aspect will be taken into account in further chapter describing how fatigue test have been implemented on 2024-T351 aluminum alloy so to initiate the damage taking it from a cut scratch to a sharp tip crack of the desired initial dimension to fatigue.

Initiation is an important part of fatigue life. Some important aspects are connected to the crack initiation time, that is:

- even a single loading cycle is sufficient to create micro-cracks
- crack extension in each subsequent loading cycle
- intrusion mechanism implies de-cohesion between atoms
- initiation is regarded as a surface phenomenon




1.3. LINEAR ELASTIC FRACTURE MECHANICS

After initiation, which is a surface phenomenon, crack growth period involves the extension of a crack penetrating in the material, thus the crack growth resistance depends on the material as a bulk property and is no longer a surface phenomenon.

There are several aspects affecting the fatigue mechanism, such as:

- crystallographic nature of the material
- crack initiation at inclusions
- crack growth boundaries and thresholds
- number of crack nuclei
- surface finishing
- macro crack growth and striations
- environmental effects
- cyclic loading condition, tension or torsion

Regarding the crystallographic aspect, the type of crystal lattice can affect the slip system, as in ??:

Material	Lattice	E_{\max} [111] (GPa)	E_{\min} [100] (GPa)	Ratio
α -Fe (ferrite)	Body Centered Cubic 	284.5	132.4	2.15
Al	Face Centered Cubic 	75.5	62.8	1.2
Cu	Face Centered Cubic 	190.3	66.7	2.85


Mg & α -Ti: Hexagonal Close Packed 

Figure 1.7: Crystallographic aspects regarding fatigue

This way, the aluminum alloys ease of cross slip is easy, while that of nickel and copper alloys is difficult.

1.3 Linear Elastic Fracture Mechanics

After the F-111 crashes the damage tolerance procedure began to be used to make predictions on structures fatigue life, studying the crack growth, starting from a defect, even if not detectable in the component of interest, supposed to be present, as is for the majority of manufacturing products, which can develop in defects that, due to the loading conditions, geometry and stress field, can lead to the failure of the structure.

The field of Fracture mechanics can be divided into two groups.

- LINEAR ELASTIC FRACTURE MECHANICS, which describes the fatigue life behavior of a small crack tip plasticity area surrounded by a predominant elastic field.
- ELASTO-PLASTIC FRACTURE MECHANICS, which is suitable to describe the behavior of a crack tip growing in a mainly plastic field.

The majority of aeronautical structures behavior can be described by means of LEFM.

It is a well known example to compare the stress field with the fluid flow. Consider a plate loaded in tension on its bottom and upper part, and a hole placed in its middle. Let's be plates edges far enough to not influence the stress distribution around the hole. The result will be that the flow line going from the upper to the bottom plate side will have to collapse closer to each other in correspondence to the hole maximum width, going again parallel after leaving that point. At the hole's sides the plate will experience three times the stress present in other specimen points. The stress field amplitude is influenced by the hole's radius. this is particularly evident in the case of an ellipse, as depicted in the following picture ??:

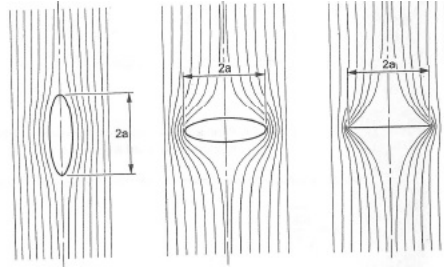


Figure 1.8: Stress Flow around a Crack

As a general rule, in correspondence to the minor crack tip radius, the flow is forced to concentrate, thus leading to a stress concentration. This way, a crack tip characterized by zero radius, gives rise to an infinite stress concentration factor. This problem has been overwhelmed by Inglis in 1973, who proposed to simulate the crack as an elliptical stress concentration to be calculated as:

$$\sigma_{local} = \sigma \left[1 + 2 \sqrt{\frac{a}{\rho}} \right] \quad (1.2)$$

where:

- ρ is the radius at the ellipse tip
- a , is half the horizontal axis length of the ellipse

A step further in the development of the damage tolerance project criterion, was given by Griffith, who stated that elastic solid failure could be predicted by means of a minimum potential energy theory. This way, as a superimposition of effects:

$$U = U_0 + U_a + U_\gamma - F \quad (1.3)$$

where:

- U_0 is the elastic energy of an uncracked unloaded plate
- U_a is the elastic energy variation due to the crack insertion
- U_γ represents the elastic surface energy variation due to the crack presence

- F is the work done by the external forces

The various energies can be expressed as follows:

$$U_a = \frac{\pi\sigma^2 a^2}{E} \quad (1.4)$$

$$U_\gamma = 2(2a\gamma_e) \quad (1.5)$$

where γ_e is the elastic surface energy of the material. In equilibrium condition, with $F=0$, U_0 , following directly from its definition, doesn't vary with the crack extension. following from the above equation, for a crack increase, there must be a balance between the energy release rate U_a and the surface energy U_γ . the above mentioned equation can thus be written as:

$$\frac{\pi\sigma^2 a}{E} = 2\gamma_e \quad (1.6)$$

where:

- $$\frac{\pi\sigma^2 a}{E} = G \quad (1.7)$$

and is regarded as the crack driving force;

- $$2\gamma_e = R \quad (1.8)$$

and is regarded as the resistance to the crack extension

In order to have the crack extension, being at balance $G=R$, G must reach a critical value:

$$\frac{\pi\sigma^2 a}{E} = G_c \quad (1.9)$$

being γ_e and E material properties. After that, Irwin introduced an important parameter for the stress field evaluation, thus the stress intensity K , which can be written as:

$$K = \sigma\sqrt{\pi a} \quad (1.10)$$

1.4 Crack in stress Field: Plane stress and Plane Strain conditions

As can be seen in the ??

the crack cause the stress field to give rise 2D surface state of stress. Since a load cannot be transferred across the crack surfaces, this gives rise to two unloaded zones at top and bottom crack surfaces.

When considering the component thickness, a 3D state of stress arises thus leading to two main conditions:

- Plane Stress
- Plane Strain

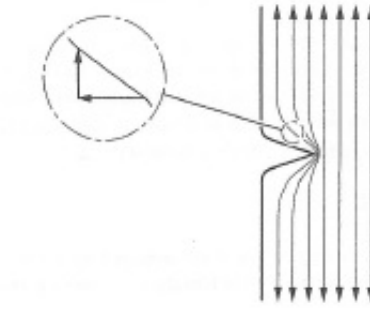


Figure 1.9: Stress Field around a crack Tip

In case of plane stress condition, the instability plane is 45 degrees inclined in respect to the tensile stress; whereas, in case of plane strain, the fracture instability will occur on a plane which is normal to the tensile stress. Under uniaxial stress, the relation between shear stress and yielding is:

$$\tau = \frac{F_{ty}}{2} \quad (1.11)$$

1.5 Crack Tip Evaluation

To evaluate the stress conditions at the crack tip, an important parameter, identified as stress intensity factor, has to be defined. In case of infinite plate with central crack, this dimensionless parameter can be written as:

$$K_0 = \sigma \sqrt{\pi a} \quad (1.12)$$

in order to take into account the specimen borders influence, the Stress Intensity Factor (SIF) has to be represented as:

$$K_0 = \beta \sigma \sqrt{\pi a} \quad (1.13)$$

where:

$$\beta = \frac{K_I}{K_0} \quad (1.14)$$

β is regarded as a geometry factor and I is the loading direction, which, if tensile, causes the crack opening.

1.6 Fracture Toughness

As explained before, in order to have the crack extension, the force G_c , known as fracture toughness, has to reach a critical value. The fracture toughness can be identified as, K_{IC} and K_C , depending on the crack being under plane strain or plane stress respectively. The fracture toughness depends:

- thickness

1.7. CRACK GROWTH DESCRIPTION. INTRODUCTION TO FATIGUE

- material orientation
- material strength

As can be seen from the picture ??:

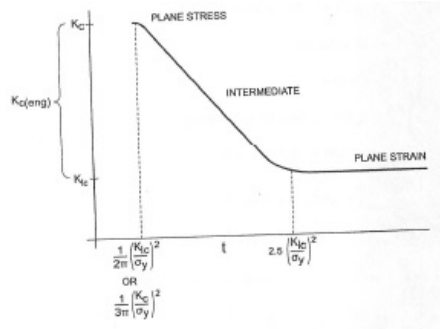


Figure 1.10: Fracture Toughness dependence on the coupon thickness

The fracture toughness decreases increasing the specimen thickness. An other important parameter to describe fatigue life of a component, is the correspondent orientation between the loading and the crack direction. In order o better understand it is useful to introduce the following picture, ??:

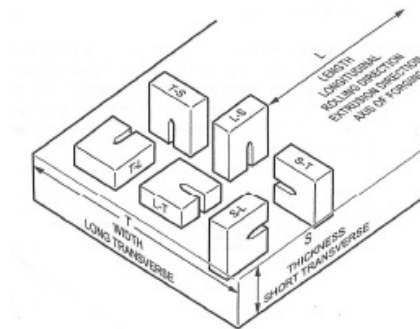


Figure 1.11: Fracture Toughness dependence on the coupon machining and crack orientation

In the picture above, the first letter refers to the loading direction, whereas the second, to the crack orientation. This aspect will be recalled in the following chapters when evaluating the fatigue life performances of the cracked coupon under tensile loading. In that case it will be also highlighted the importance of the clad treatment in affecting, thus acting as a crack growth promoter, the component fatigue life.

1.7 Crack Growth description

Paris associated the stress intensity factor concept to crack growth, via the following law:

1.7. CRACK GROWTH DESCRIPTION. INTRODUCTION TO FATIGUE

$$\frac{da}{dN} = C\Delta K^n \quad (1.15)$$

where:

$$\Delta K = K_{max} - K_{min} \quad (1.16)$$

It is important to notice that Paris law is valid only for a particular region of the crack growth description, as reported in the following picture??:

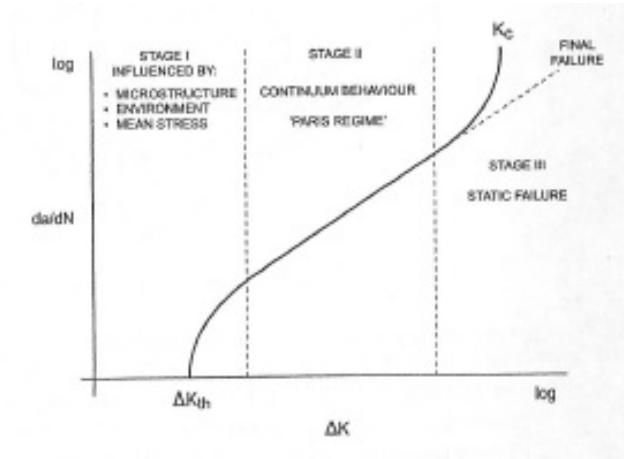


Figure 1.12: Crack Growth Rate against the Stress Intensity Factor

Subsequent and more detailed models have been developed, and can be summarized as follows:

$$\frac{da}{dN} = c_w[\Delta K(1 - R)^{m-1}]^n \quad (1.17)$$

which is the Walker equation. In this relation:

- C_w is the value of $\frac{da}{dN}$ at $R=0$ and $\Delta K=1\text{ksi}\sqrt{\text{in}}$
- exponent $0 < m < 1$, the curve shifting decreases while m increases
- n is the Paris exponent

Then, the Forman equation was developed to describe the upper part, right region, of the $\frac{da}{dN}$ vs ΔK curve, describing the crack behavior going up to failure. This equation can be written as:

$$\frac{da}{dN} = \frac{C_f \Delta K^n}{((1 - R)K_c - \Delta K)} \quad (1.18)$$

where:

- c_f is $\frac{da}{dN}(K_c - 1)$ at $R=0$ and $\Delta K=1\text{ksi}\sqrt{\text{in}}$
- K_c is the critical stress intensity factor

1.8. CRACK GROWTH ANALYTICAL PREDICTIONS TO FATIGUE

Finally, in order to better understand the studies on fatigue components described in the following chapters, the Nasgrow equation is reported:

$$\frac{da}{dN} = C \left[\frac{1-f}{1-R} \right]^n \frac{1 - \frac{\Delta K_{th}}{\Delta K}}{(1 - \Delta K_{max} K_{crit})^q} \quad (1.19)$$

where:

- C is the Paris coefficient
- n is the Paris exponent
- p and q are the Nasgrow equation exponents
- ΔK_{th} is the threshold stress intensity range
- R is the loading ratio
- K_{max} is the maximum stress intensity
- K_{crit} is the stress intensity factor

1.8 Crack Growth Analytical Predictions

Following from the Paris Law, a coupon fatigue life can be estimated as:

$$dN = \frac{da}{C(\Delta\sigma\sqrt{\pi a})^n} \quad (1.20)$$

thus leading to:

$$N = \frac{1}{C\Delta\sigma} \int_{a_0}^{a_f} \frac{da}{(\sqrt{\pi a})^n} \quad (1.21)$$

The integral increments can be defined as equal or as a percentage of the growing crack. Defining the increments as equally spaced, has the advantage of reducing the computational time costing, but can result in loss of accuracy in terms of SIF crack growing evaluation. On the other hand, implementing the increment in terms of crack growth percentage can lead to a more accurate SIF evaluation, even if causing an increment in computational time. The evaluation reported above can be implemented taking into account the geometry factor β , as:

$$N = \frac{1}{C(\Delta\sigma\sqrt{\pi})^n} \int_{a_0}^{a_f} \frac{da}{(\beta\sqrt{a})^n} \quad (1.22)$$

In order to have a growing crack, the threshold value of Δk must be reached. If under a loading application a crack shows no growth, it is safer to induce a loading increment or, leaving the load as is, increase the crack length; then if the crack under investigation, experiencing the previously superimposed conditions, starts to grow, this means it was only under the threshold value. The threshold parameter is loading ratio dependent. It's noteworthy to define the crack closure behavior, thus referring to the chance of the crack to not completely close during fatigue cycle, giving rise to an effective Δk , which is only a reduced value of

the expected one. Proceeding in these introductory definitions, it is important to highlight that a crack, while growing, forms a plastic region at its tip. This region acts as crack growth retarder, as it is composed of yield material which bulges into the crack, enabling the expected crack growth during a fatigue cycle. LEFM approach cannot be used to describe the crack growth of a short crack, since, differently from a big one, this experiences the micro-structure not as an average of the surrounding elastic field; thus the attempt to describe a short crack growth by means of LEFM, leads to erroneous predictions. This case, a crack can be also included in the plastic zone formed by a bigger neighboring crack. In this optics, a flight overload, coming for eg. from a turbulent flight, can lead to the formation of a bigger then expected plastic zone at the crack tip, thus acting as a crack retarder. The retardation effect is function of material and thickness as well.

1.9 Threshold and overload plasticity affecting the growth

The threshold value, which is dependent on R , represents a value below which there is no crack growth. At each loading application, the crack tip experiences the formation of a plastic zone in which to grow. As a consequence when a crack is subjected to a bigger load, then the plastic zone at the tip is bigger than that forming when a lower load is applied. A model predicting the plastic zone dimension that forms at the crack tip has been implemented on the matlab giving the following results ?? and ??:

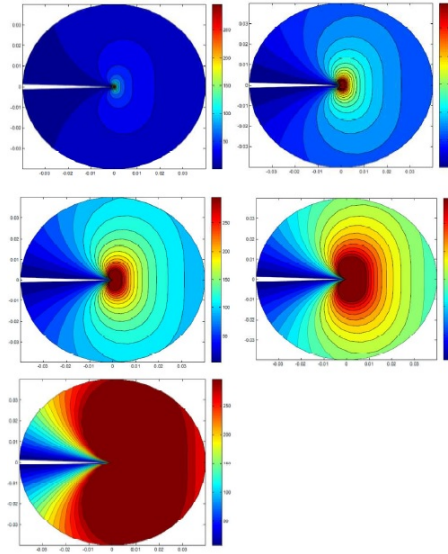


Figure 1.13: Plastic Zone at Crack Tip at 180 MPa

Predictions ?? and ?? are referred to an edge crack growing in an aluminum 2024-T351 panel thickness 1.4 mm ??:

As can be seen from ?? and ?? the plastic zone growing at the crack tip at 180 MPa is definitely bigger than that at 90 MPa. This aspect is confirmed from

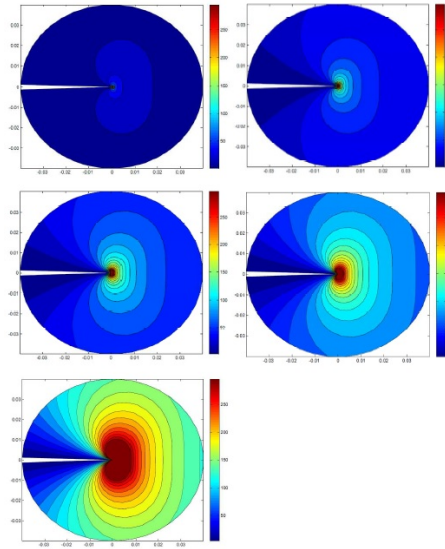


Figure 1.14: Plastic Zone at Crack Tip at 90 MPa

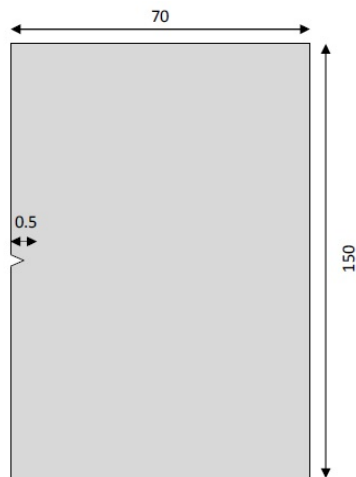


Figure 1.15: Specimen Configuration

the experimental tests implemented in Forli, Bologna University, where it took only 30000 cycle for the scratch to grow in a sharp 4 mm crack at 180 MPa, $R=0.2$, frequency 5 MPa, whereas it took 100000 cycles for the crack to start growing again after having reduced the load to 90 MPa to be representative of a fuselage loading condition.

The value of 180 MPa has been chosen since looking at Wohler curve, thus S-N curve, it has been highlighted that crack propagation cannot occur at lower loads (since S-N curve, as above mentioned, take into account also the crack initiation period). The plastic zone growing at the crack tip is a function of the stress intensity factor and the yield strength of the material. During flights, overloads contribute to the development of a bigger plastic zone at the crack tip which results in a crack growth retardation.

Nevertheless, short cracks can grow also at loads under the threshold limit, as reported in the literature, and can be seen in ??:

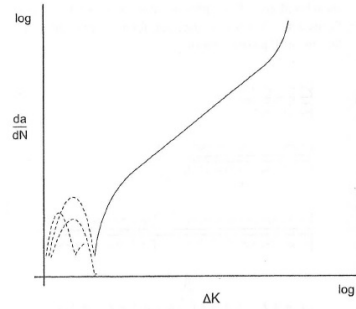


Figure 1.16: Short Crack Behaviour vs Long Cracks one

The dashed line in ?? describes the behavior of short cracks whereas the solid line, that of long cracks. Since a micro-crack can be contained in the plastic notch area or in a grain of metal, its behavior cannot be described by LEFM.

1.9.1 Center Cracked Panel

The stress intensity factor for an infinite centre cracked panel or for on in which the crack length is very small if compared with the panel width, is close to one; even if this value starts to increase when the crack dimension are comparable whit the panel ones. The standard equation for the stress intensity factor can be written as ??:

$$K = \beta \sigma \sqrt{\pi a} \quad (1.23)$$

Being equation ?? referred to ??:

There are several tabulated equations and graphs describing the β parameter for a center cracked panel, as well as for an edge cracked one or whatever.

1.9.2 Edge Cracked Panel

An edge crack can be seen like part of what before was a centre cracked panel divided in half, like ??:

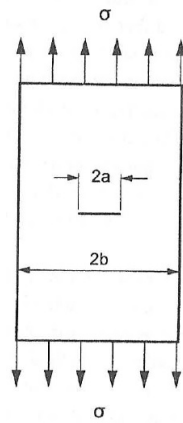


Figure 1.17: Centre Cracked Panel

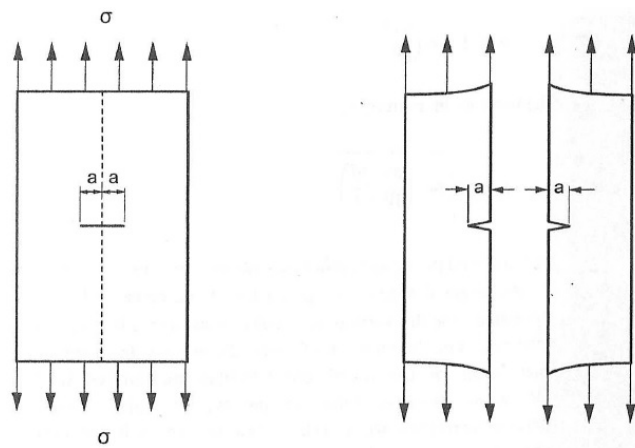


Figure 1.18: Edge Crack configuration

The stress intensity factor for an edge cracked panel is higher than that for a centered cracked one since the crack faces are free to open more than in a center cracked configuration, as can be seen from ???. The additional displacement characterizing the crack surfaces results in bigger displacements allowed, thus higher stress intensity factor. Thickness changes can have a great influence on the stress intensity factor, since bigger thicknesses contribute to a smaller SIF.

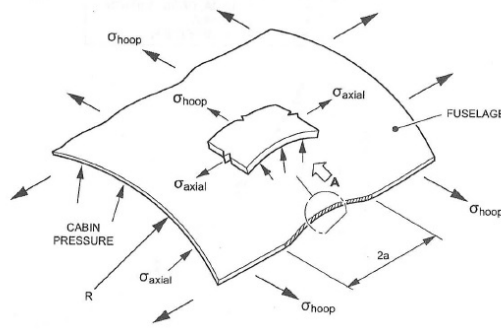


Figure 1.19: Stress acting on a fuselage

Looking at the reported figure ??, different stresses are acting on cracks depending on the direction in respect to the fuselage, such as:

- longitudinal cracks are loaded in hoop stress
- circumferential cracks are loaded in axial stresses resulting from both bending and pressure action

The interaction between the aforementioned loading conditions, result in the crack out of plane bulging. The bulging factor takes into account the effect of the fuselage curvature on the stress intensity acting at the crack tip, which is bigger than that of an analogous crack in a flat panel, since displacement involved are bigger. ??:

$$\beta_{bulge} = \frac{K_{curve}}{K_{flat}} \quad (1.24)$$

The crack tip bulging has been firstly described by Khun:

$$\beta_{khun} = 1 + C \frac{a}{R} \quad (1.25)$$

where C is a constant value set at 9.2. Then Swift proposed a value of 10 for the parameter C based on his studies on DC-10. After Folias introduced a more generic equation to describe the bulging factor for a longitudinal and circumferential crack on a cylinder introducing a shell curvature parameter λ :

$$\lambda = \frac{a}{\sqrt{Rt}} \sqrt[4]{12(1 - \nu^2)} \quad (1.26)$$

in which:

- R is the radius of curvature

- t is the shell thickness
- a is half the crack length

Finally Erdogan enlarged this formulation covering a larger range of λ .

1.10 Plastic Zone arising at crack tip

The plastic zone is an area of low stiffness. The magnitude of the plastic zone plus the crack length gives an estimation of the remaining coupon elastic area. When the area interested by the plastic zone is comparable to that of half the remaining ligament, the LEFM is no longer valid. Attention must be paid, according to Irwin, in distinguish between the crack length and the effective crack length which includes the plastic zone size, thus ??:

$$a_{eff} = a + \Delta a \quad (1.27)$$

where Δa accounts for the stresses above $\sigma_{0.2}$ in the elastic case. Based on ??:

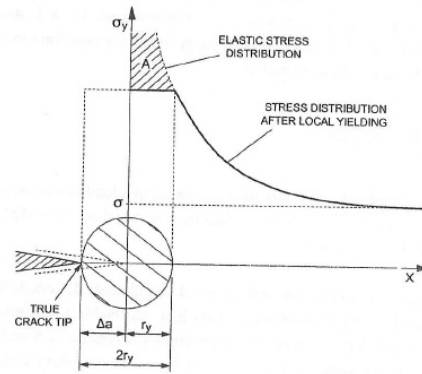


Figure 1.20: Plastic Zone at Crack Tip

Assuming:

- circular plastic zone area
- consider stress distribution along x axis
- material elastic- perfectly plastic

The Irwing- Westengard equation can be written as ??:

$$\sigma_y = \frac{K}{\sqrt{2\pi r}} \quad (1.28)$$

which can be written as ??:

$$r_y = \frac{1}{2\pi} \left(\frac{K}{\sigma_{0.2}} \right)^2 \quad (1.29)$$

and being:

1.10. PLASTIC ZONE ARISING AT CRACK TIP IN INTRODUCTION TO FATIGUE

$$K = \sigma \sqrt{\pi a_{eff}} \quad (1.30)$$

$$\sigma_{0.2} \sqrt{2r_y} = \sigma \sqrt{(a + \Delta a)} \quad (1.31)$$

Since all the stresses have to be transmitted, the area A must equal $\sigma_{0.2} \Delta a$, giving at end:

$$\Delta a + r_y = 2r_y \quad (1.32)$$

The plastic zone arising at crack tip in thick structures is very small, leading to a value of $C=6$, whereas for thin sheets, being the crack tip under plane stress, the plastic zone is bigger since the yield stress is smaller. Such a behavior can be roughly and graphically estimated by the crack growth resistance curve, thus the R-curve. Instability K_c , which depends upon material properties opposing to crack growth, occurs when K_i , the stress intensity factor at crack tip, increases more then K_r , ??,??:

$$K_r = \beta \sigma \sqrt{\pi(a_0 + \Delta a)} \quad (1.33)$$

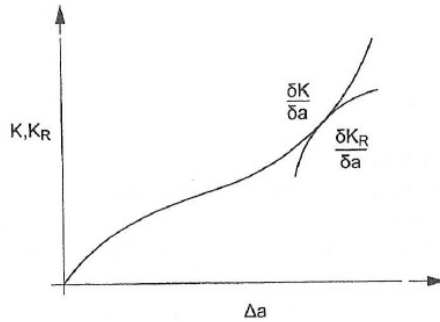


Figure 1.21: Energy Balance between K and R

R-curve is experimentally determined and accounts for the effective crack length ??. The R-curve for plane stress and plane strain differ in shape like ??:

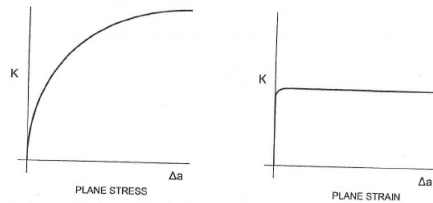


Figure 1.22: R-curve in plane stress and plane strain

R-curve shape depends not only on the material thickness but also on the material itself; aluminum 7000 series R-curve is steeper than that of 2000 series.

1.10. PLASTIC ZONE ARISING AT THE CRACK TIP IN INTRODUCTION TO FATIGUE

Crack Growth can be lowered if using mechanical treatment such as laser shock peening. An evaluation of the plastic zone arising at the crack tip on a baseline, as well as on a LSPeened configuration, using the residual stresses introduced by the treatment and measured at Elettra Synchrotron in Trieste, is reported below ???. A laser peened symmetric configuration is compared with the predicted plastic zone shape arising from the interaction between the growing crack tip and an LSP oblique pattern in order to see how a different plastic zone shape can constitute a preferential path for the growing crack. ??, ??:

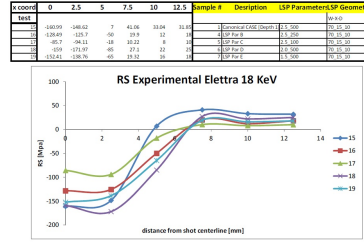


Figure 1.23: RS measured at Elettra at 18KeV in LSPeened panel

reported in ?? are the residual stresses measured at Elettra for some tested laser peening settings.

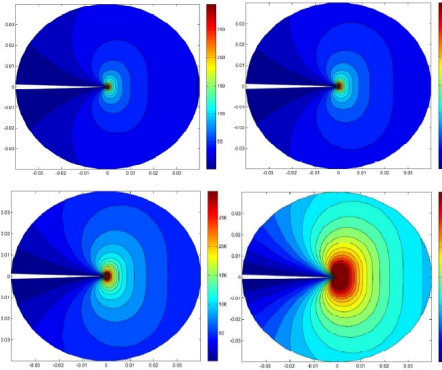


Figure 1.24: Plastic Zone LSPeened symmetric Configuration

Figure ?? shows the plastic zone growing as the crack tip approaching the laser peening pattern. Adopted parameters for the simulation are:

- laser pattern width = 10 mm
- laser pattern length = 100 mm
- yield = 310 MPa
- external load magnitude = 90 MPa
- initial crack length = 5 mm
- compressive residual stress induced by LSP = 150 MPa
- panel thickness = 1.4 mm

1.11. EFFECT OF RESIDUAL STRESSES ON CRACK GROWTH FATIGUE

- panel length = 150 mm
- panel width = 70 mm

Figure ?? refers to a symmetric shot configuration while the following ??, refers to an oblique laser pattern:

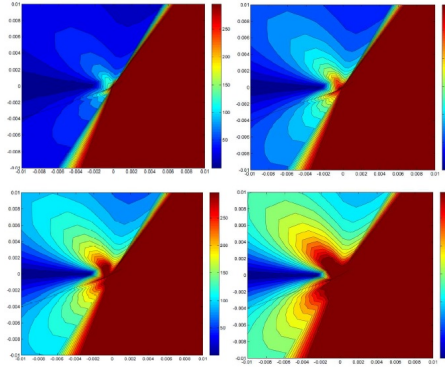


Figure 1.25: Plastic Zone of Crack approaching an Asymmetric laser pattern

Looking at ?? it can be seen how the plastic zone due to the interaction of the growing crack tip and the laser pattern gives rise to an asymmetric plastic area; this configuration can constitute a preferential path for the crack in which to grow. Summarizing, fatigue evaluation of a structure can be divided in two main periods:

- fatigue initiation
- fatigue life

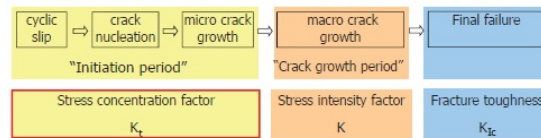


Figure 1.26: main parameters involved in each fatigue life period

1.11 Effect of Residual Stresses on Crack Growth

Residual stresses (RS) are those which remains in a body that is stationary and at equilibrium with its surroundings. They can be either compressive or tensile in nature but compressive stresses are sometimes introduced deliberately to improve fatigue resistance. As the design of engineering components becomes less conservative, there is an increasing interest in how residual stress affects mechanical properties. This is because structural failure can be caused by the combined effect of residual and applied stresses. In practice, it is not likely that any manufactured component would be entirely free from residual stresses

HAAS PRESSES IN CONTROL TO GROW WITH FATIGUE

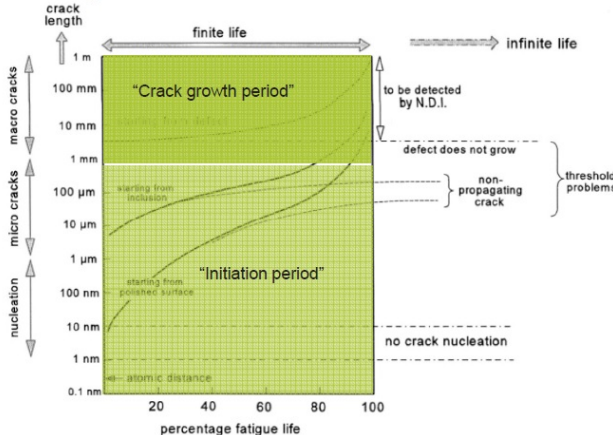


Figure 1.27: crack initiation and growth

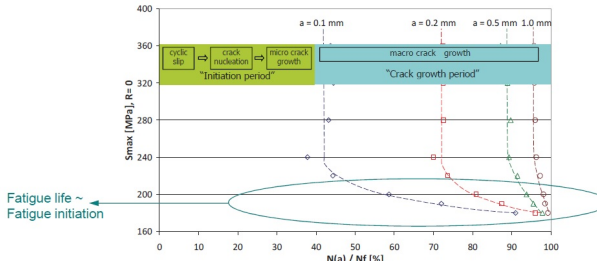


Figure 1.28: crack initiation and growth on S-N curve

1.11. EFFECT OF RESIDUAL STRESSES ON CRACK GROWTH FATIGUE

introduced during processing. Furthermore, in natural or artificial multiphase materials, residual stresses can arise from differences in thermal expansivity, yield stress, or stiffness. Considerable effort is currently being devoted to the development of a basic framework within which residual stresses can be incorporated into design in aerospace, nuclear, and other critical engineering industries. Depending on the scale over which they equilibrate, residual stresses are categorized into three different types.

- Macroscopic Stresses, which are homogeneous over a length scale representative of the dimension of the material or component and the net forces due to these stresses is balanced over the same scale length.
- Intergranular stresses exist at the grain scale, and are generally present to some extent in all polycrystalline materials. This type of stress appears in the structure due to inhomogeneous plastic flow or thermal mismatch at the grain level, or the presence of more than one phase (precipitates) or phase transformation in the structure.
- Atomic stresses exist over atomic dimensions and balance within a length scale comparable with the grain size. Examples of these stresses are those caused by dislocations and point defects.

Many processing techniques introduce a significant amount of residual stress in the structure. Moreover, when these components are in use these existing residual stresses can be modified or new stresses can be created locally. The new state of the stresses interacts with the existing micro-cracks modifying their crack growth process and, in the worst case, leading to premature or sometimes catastrophic failure of the parts.

On the other hand, compressive residual stresses can significantly improve fatigue behavior. In fact, a proven method for reducing the fatigue related problems in metallic structures is to drive compressive residual stresses into the affected area by means of Laser Shock Peening (LSP) technique. This surface treatment is very effective in bulk structures, improving life performances of fatigue sensitive aeronautical components, such as jet engines turbine blades or helicopter gearboxes. The LSP process is based on a high-power pulsed laser beam of very short duration (1 to 10 ns) focused on the surface to be treated, which is covered by a coating (ablative layer, usually black paint or a very thin aluminum foil). The laser beam hits the ablative layer, which partially evaporates into the plasma state. A transparent layer, usually water, is required over the coating and prevents the plasma expansion, thus resulting in a compressive shock wave propagating into the metal. The shock waves are essential for locally inducing plasticization of the metal and the establishment of the compressive residual stresses. Test results available in the bibliography show that the residual compressive stresses induced by LSP increase the fatigue life of bulk metallic components, whereas quite limited studies have been presented on the fatigue crack growth in thin components. The beneficial effect of LSP in terms of fatigue crack growth on compact tension specimens with crack tips very close or inside to the laser shot pattern has been assessed, while an investigation on the effect of the LSP on the fatigue crack propagation of a macro-crack approaching the LSP treated area is still missing. As a consequence of the self-balancing residual stress field induced by the LSP in the thin-gauge panel, the chosen LSP pattern

1.11. EFFECT OF RESIDUAL STRESSES ON CRACK GROWTH FATIGUE

configuration (distance of the crack tip to the laser shot, width of the laser pattern) can affect significantly the fatigue crack propagation performances of the panel. Therefore, the aim of this thesis work is to investigate the effect of the residual stress distribution introduced by the LSP on the crack growth in thin panels. These stress distributions have been assessed by means of experimental tests and finite element simulations. Their effects on the crack growth has been analytically evaluated to perform a sensitivity study in order to determine which LSP parameters can influence the crack growth rate.

Bibliography

- [1] Les Bent *Practical Airframe Fatigue and Damage Tolerance* 2010.
- [2] H.J. Schmidt. *Damage tolerance technology for current and future aircraft structure*, Plantema Memorial Lecture presented to the 23rd ICAF Symposium, Hamburg, Germany, June 2005.
- [3] W. Schtz. *A history of fatigue*, Engineering Fracture Mechanics 54: 263-300, 1996.
- [4] J. Schijve. *Fatigue of Structures and Materials*, Springer ed., 2009.
- [5] D. Broek. *The practical use of fracture mechanics*, Springer Ed., 1986.

CHAPTER 2

Laser Shock Peening

2.1 Laser Physics

Laser devices use the stimulated emission of electromagnetic radiation to emit light. Laser emit light coherently, this aspect allows a laser beam to stay focused to a tight spot over long distances. Laser can also have temporal coherence, which allows it to have a narrow spectrum, thus to emit a single color of light and produce pulses of light as short as a femtosecond. Laser can be used for cutting and welding materials as well as to introduce deep compressive residual stresses in metal components thus, eventually, increasing their fatigue life. Spatial coherence makes it possible for lasers to have a narrow diffraction limited beam, focused on small spots, which can be concentrated at its power to large distances. Lasers are characterized by temporal coherence as well. Wavelength in vacuum is what characterizes lasers. Laser electromagnetic radiation can be at any frequency, so not only at visible light but also infrared, ultraviolet, X-Ray and so on.

An electrical discharge takes place between an anode and a cathode connected by a tube. At both end of the laser cavity are mirrors, one of which is fully reflecting while the other is just partially reflecting. The small portion of light which is transmitted from the front mirror is the laser beam. The laser is a source of coherent light, which is characterized by coherence (all emitted photons are the same phase), monochromaticity (laser light characterized by a well defined wavelength) and collimation (ability of laser light to stay confined in a thin beam even at large distances). Photons in the tube must be very well aligned since any of them which is bounced on the wall will not contribute to the laser beam. In order to have a lasing action, a high temperature is requested to have a larger number of electron at a high energy level, in respect to that of atoms at a lower energy level. The process with which atoms are taken to a higher energy level is pumping, and it's supplied by an external electrical or optical source. Laser systems used to implement Laser Shock Peening are characterized by YAG (neodymium ions in a yttrium-aluminum-garnet host glass) rods. In order to create inversion, it is necessary to pump only and selectively the upper energy

level, and not the lower one.

2.1.1 Laser Components

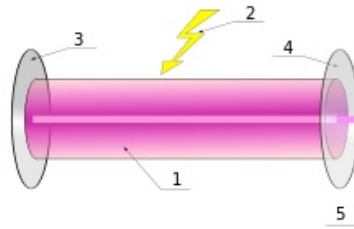


Figure 2.1: Laser Components

The main laser components are depicted in the picture above ?? and can be summarized as:

- 1. Gain Medium
- 2. Laser Pumping Energy
- 3. High Reflector
- 4. Output Coupler
- 5. Laser Beam

To explain the laser working principle we can refer to pictures ??, ??, ??:

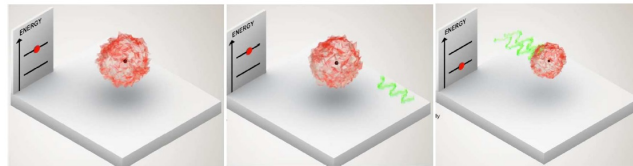


Figure 2.2: Laser Working Principle 1

A flash lamp or an other laser source provides energy to the gain medium, which is a material able to amplify light by stimulated emission. The light which passes through the gain medium is amplified, thus increasing in power. Remember that the energy of an atom is characterized by different energy levels. When an atom is excited, its energy suddenly raises to the next energy level. If a photon is sent with the proper energy to an excited atom, this last falls into its lower energy level and emits a photon which is identical to the first one. This principle is the basic for the laser behavior. In a laser, in-fact, excited atoms are put between two mirrors. A first photon stimulates an atom which emits a second photon, and so on, thanks to the presence of the mirrors which allow the photon to go to and fro. At the end all the photons are identical, with the same energy, thus some color and a unique direction. This gives rise to the laser emitted beam, with this energy passing through a narrow beam. Some lasers

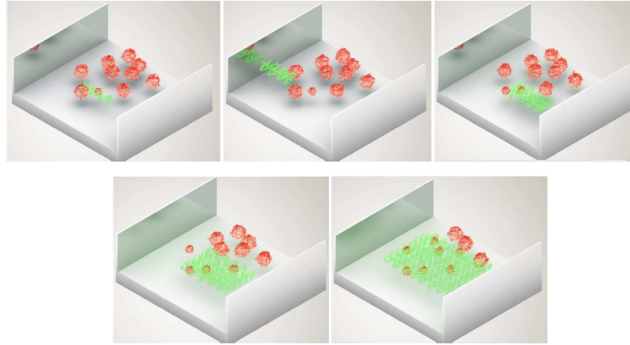


Figure 2.3: Laser Working Principle 2

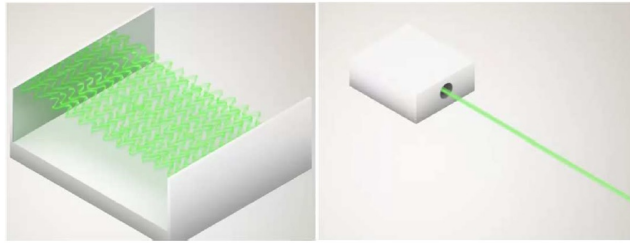


Figure 2.4: Laser Working Principle 3

contain other elements which affect the properties of the emitted light, such as the polarization, wavelength, and shape of the beam. Electrons are always found at a specific energy level of an atom. The energy absorption by an electron, due to the heat light source, allows it to change energy level. Anyway, this condition doesn't last forever since the electron decays emitting a photon, this being called emission phenomenon. So the transition from a higher to a lower energy state produces an additional photon. The gain medium of a laser is a material of controlled purity, size, concentration, shape, which amplifies the beam by the emission process described. The resonator consists of two mirrors between which a coherent beam of light travels in both directions, reflecting back on itself so that an average photon will pass through the gain medium repeatedly before it is emitted from the output aperture or lost to diffraction or absorption. At each stimulated emission, the atom goes from its excited to ground state, reducing the gain of the medium. This process results in the achievement of an equilibrium condition between gain and cavity losses, thus determining the laser operating point. Wavelength, phase and polarization of the light generated by emission and the input signal are similar. Laser exhibiting power output continuous over time are said to work on a continuous mode, whereas others working on different time scale are said to be working in a pulsed mode. A continuous laser can work as a pulsed one just switching it on and off. regarding the pulsed laser, Q-Switched applications are more referred to the peak pulse power, rather than on energy characterizing the laser pulse, thus resulting in pulses of the shorter possible duration (order of femtoseconds, 10^{-15} sec).

2.2 The photon emission process

A photon coming to an excited atom can stimulate it to emit an other photon characterized by the same wavelength and phase of the incident one, leaving this way two photons of the same properties and direction. Since the emitted photons are equal in terms of wavelength and directions, this constitutes the basic for the laser light, thus monochromaticity and coherence.

2.2.1 Q-Switching

Q-Switched mode is achieved when the losses introduced in the resonator exceed the gain of the medium, thus giving rise to a loss in the ‘Q’, quality, of the cavity which is at the basis of this principle. After the energy stored in the laser medium has reached its maximum, the loss mechanism is removed thus allowing lasing to begin. This process results in a short high energy power pulse.

2.2.2 Solid State Lasers

These lasers are characterized by the doping of a crystalline or glass rod with ions providing the required energy state. An external source optically pumps these materials with a shorter wavelength in respect to the lasing one. Many materials can be used as dopant in solid state lasers, including Yttrium Aluminum garnet (Nd:YAG). Independently from the used dopant material, solid state lasers can produce high powers in the infrared spectrum at 1064 nm. Nd:YAG lasers allow to achieve high powers in ultra short pulses.

2.3 Laser Shock Peening

As reported by Clauer in the first international conference on laser shock peening, the first generation of shock waves in laboratory is due to White, in 1962. This time, the shock waves were generated by electron bombardment and electromagnetic wave absorption. The experiments have been conducted in vacuum chamber and the laser power densities achieved were of $44 \frac{GW}{cm^2}$. In 1970, Anderholm, adopted a transparent layer to increase the pressure peak induced by the laser treatment. In early times, the attempt to model the laser material interaction have been made by means of LILA and TOODY codes. Due to the compressive residual stress field induced by the laser treatment, many efforts have been made in the attempt to understand its benefit on fatigue and corrosion phenomena. LSP was used in industrial production for the first time in the 90's on F101 fan blades to reduce FOD. Nowadays, many industries are looking towards the lowering down of the processing costs and to the development of portable systems to perform laser treatment in situ during manufacturing or repair operations. despite the first laser peening patent filed in 1974, it is only twenty years later that General electric Aviation , by means of a laser system developed by LSPT Ohio, applied the laser shock peening treatment to aircraft engine components. Industrial applications have been further developed by Metal Improvement Company, regarding the engine blades for Rolls Royce and Toshiba,

2.3. LASER SHOCK PEENING CHAPTER 2. LASER SHOCK PEENING

for preventing stress corrosion cracking in nuclear reactors. Also in this work of thesis will be described the benefit introduced by laser shock peening treatment in repair of thin aluminum structures representative of fuselage skin, when fatigue hot spots are identified. Due to its capability of introducing a deep compressive residual stress field, laser shock peening can be used to induce crack turning, thus preventing fuselage structures from explosive decompression. Experiments conducted by Fairand and Wilcox in 1972 proved that LSP on dog-bone 7050 Al alloy tensile specimen, can increase the yield strength of the material from 20 to 29%. In the years going from 1977 to 1982, attempts were made to move from laser peening applications at laboratory scale to the industrial production level. In 1978, the first residual stress measurement have been done on laser peened Al 7075-T6 highlighting the large amount of compressive residual stress induced by LSP. After these results, in 1979, fatigue capability of laser shock peening to neutralize pre-existing fatigue damages was demonstrated on Al 2024-T351. From '80s on, all the effort from scientific community and industries was focused on the development of a LSP system suitable for industrial applications (ie. high repetition rate pulse). Pulsed laser with energies exceeding 10 J per pulse and pulse duration of 10-20 seconds, which are the specifications requested to introduce shock waves into the material, were limited to low repetition rates. In 1983, Wagner Castings Co. supported by Battelle Memorial Institute, developed a laser system with reduced size and faster repetition rates in respect to the currently available at that time for the laser shock peening process. These new laser systems were characterized by high energy per pulse, 50 J/pulse, at 20 nsec pulse duration; pulse rate in the order of 1 Hz. these laser systems represented the first prototype of laser shock peening systems for industrial applications. In the following years, great efforts have been made to understand the best laser peening configuration to extend fatigue life of aeronautical components. The first massive industrial application of laser shock peening treatment has been made by General Electrics Aviation in 1997 relatively to the production of engine fan blades on the F101. These production could operate from 4 to 8 hour continuously with no surface preparation, thus no ablative medium presence.

In 1999, Toshiba started laser peening process without coating, to be used for stress corrosion cracking (SCC) in core shrouds in boiling water reactors. The main differences between the laser peening system developed in the USA and that developed by Toshiba, were the pulse duration, between 5 and 10 nsec for the system developed in Japan, as well as lower pulse energy (100-200 mJ), which implies the adoption of very small spot diameters, typically 1 mm.

As already mentioned, due to the laser capability to introduce high compressive residual stresses in the treated components, LSP can be used to increase fatigue life of aeronautical components. Knowing the residual stress field, the component geometry, the loads and the material properties, it is possible to predict the location of fatigue crack initiation and life at which it occurs. Once the crack location and material crack growth properties are known, Linear Elastic Fracture Mechanics (LEFM), can be used to predict fatigue crack growth and crack trajectory. Aircraft structures can be designed taking into account the chance to insert compressive residual stress by means of technologies such as laser shock peening, in order to redirect the crack initiation and growth to less severe areas and in preferable path, which can be more easily accessed during maintenance. Nevertheless, as will be demonstrated further in this work of thesis, the use of laser peening technology at a design phase can be difficult, since benefit

in fatigue life can be achieved depending on the crack length and its distance from the laser pattern; this aspect can be easily understood if thinking that aside the laser pattern, characterized by compressive residual stress, a tensile area arises to restore equilibrium. Tensile residual stresses are well known as crack growth promoter. The peened strap has to be placed in such a way to obstacle rather than facilitate crack growth. Considering all this aspect a benefit in fatigue can be more easily achieved when using LSP as a repair solution. Crack retardation induced by means of LSP treatment, not involving the use of extra fasteners, allows to reduce the overall weight of the structure, thus resulting in less consumption and environmental benefits. Also, the fatigue initiation resistance of an integral structure is considerably increased because of the reduction of number of fasteners, since LSP doesn't result in adding of material or introduction of holes. Starting from this considerations, a possible solution can be the use of residual stress stripes across the crack path, to slow down and eventually redirect the crack growing through the LSP stripes.

2.3.1 Laser Systems

The Laser systems needed to perform the peening treatment involve minimum energies of 20 Joules/pulse, whereas the standard in the industries is 3 Joule/pulse. An important parameter which controls the the produced shock wave, thus the pressure peak achieved and subsequently the compressive residual stress induced in the target, is the laser wavelength.

Important factors in the laser choice to implement the peening treatment are cost savings, efficiency, maintenance and replacement requirements.

Laser parameters which are regarded as the most important ones in the achievement of the best compressive residual stress field to increase the component fatigue life, are the wavelength, pulse frequency, spot dimension, and other, like the laser power intensity which will be presented more in detail in further sections. Of great importance is also the optical delivery system and its arrangement, since focusing the laser beam on the component to be treated, it affects the efficiency of the technology when not resulting in loss of energy due to reflection phenomena taking place due to the incorrect choice of the medium.

An other important factor is the laser beam size, which determines the laser spot size hitting the component to be treated, thus resulting in a different compressive residual stress field induced. Different choice of the laser spot size characterizes the major LSP suppliers, such as Toshiba, Metal Improvement Company and Universidad Politecnica de Madrid. This way, the different spot size choice influences also the way the treatment is implemented, with or without coating.

2.3.2 Opaque Overlay

The opaque overlay is usually made of black painting or aluminium foils, 10 μm thick. This ablative layer acts mainly in two ways:

- at the laser impact, form plasma which then evaporates giving rise to a shock wave propagating inside the target
- act as protective layer so to not induce big surface roughness

MIC uses as ablative layer an aluminum foil, 10 μm thick, and this way is numerically implemented in the subsequently described FEM models developed via the Abaqus software.

Fairand and Clauer in one of their work demonstrated that different kind of material used to implement the opaque overlay didn't really influence the shock wave induced thus the residual stress field achieved.

The opaque overlay has two main properties:

- enhancing the creation of plasma by vaporization, thus resulting in a more consistent shock wave
- Protecting the component surface by micro-structural changes, since laser peening involves plasma at high temperatures, up to 10000°C.

Local melting induced by laser especially in case of absence of ablative layer, can be avoided controlling the laser power choice. Due to the high temperatures involved, some cooling requirements maybe imposed for high power lasers, such as that used for laser peening treatment.

Surface damages can be avoided using small laser spot size, increased overlap and high density of impacts.

The choice to perform the laser treatment with the ablative layer make it needed to take into account the cost due to the material itself and the manufacturing process since nowadays the ablative layer needs to be placed manually. Moreover its state has to be checked when moving to applications which involve multiple laser pattern, since it can be damaged. Also, to have reliable measurements of the compressive residual stress field achieved, the ablative layer has to be carefully removed. Attention must be paid when removing it, to an eventual release, causing changes in the stress field achieved. This can influence mainly the reliability of surface residual stress measurement techniques, such as XRD, while incremental hole drilling is less affected by this phenomenon since it allows to evaluate the residual stresses deeper through the coupon thickness.

2.3.3 Transparent overlay

As reported previously, the first experiments on LSP have been conducted without transparent layer, which was introduced by Anderholm in 1970. The introduction of a transparent overlay, confines the generated plasma which results in shock waves two orders of magnitude bigger then that produced in vacuum. According to Peyre et al., the adoption of a transparent overlay can lead to pressure peaks from five to ten times higher in magnitude and to two or three times longer in duration in respect to a non confined regime. During the years several materials were adopted as transparent overlays, quartz, glass, polymeric materials and distilled water. Water proved to be the best choice in term of compromise between properties, costs and ease of use. Water can be either running or stagnant. Attention must be paid for water to not contain impurities, which can cause laser reflection, thus energy loss. An other important parameter in terms of compressive residual stress field achieved is the water layer thickness. As reported in the literature, an important factor to be taken into account while performing the laser treatment is the dielectric breakdown, which is expected to influence the real amount of energy reaching the component surface. A thicker water layer can result in higher energy loss and random beam

deviation, but prevents from cavitation and surface roughness. Air breakdown does not affect the laser treatment at lower energies, so the previously mentioned choice of laser parameters may help in preventing from this phenomenon. A too thin water layer can result in energy loss as well, due to the water boiling. While developing the technology, different materials describing the transparent overlay have been adopted.

Fairand and Clauer developed the LILA Code and investigated the different combination of transparent and opaque layers to achieve the best condition in terms of pressure peak, thus the shock wave giving rise to the deeper compressive residual stress field. The main Laser suppliers use different transparent layers strategies; Toshiba immerse completely the component into the water, while Metal improvement Company focuses a high pressure water jet towards the component to be treated. It is immediately evident that the water jet solution is the more practical for industrial applications.

Test conducted on laser performances at Witwatersrand University showed an energy loss resulting from thicker water layer adoption. Thicker water layers resulted in energy losses because they provided a lower power density reaching the coupon surface, on the other hand, they proved to be effective in preventing from cavitation phenomena; thus a compromise solution has to be used.

The erroneous choice of water thickness as well as the distance from the target surface, can lead to random beam deviations, water ripples and damages of the treated area. moreover, erroneous choice of water layer thickness result in irregularities in the laser treatment.

Impurities present in the distilled water can result in surface damages.

Water filtering system is needed to avoid uncertainties in the delivered energy, due to contamination present within the water, since this can result in some aluminum surface particles to be eroded.

Depending on the water layer thickness, the hitting laser can result in the formation of two confined bubbles giving rise to a stronger shock wave even if lower power densities are used. This phenomenon is not yet quantified from an experimental point of view, and this can lead to difficulties in the process repeatability, as well as on its numerical representation.

Attention must be paid when performing the laser treatment to both buckling and bending phenomena; this way, attention must be paid also when measuring the residual stress field via hole drilling technique, on thin aluminum panels. When performing laser shock peening on thin components, reflection phenomena due to the interacting shock waves, can result in a lower compressive residual stress field induced, as well as on panels' distortion.

In order to achieve the desired stress field, laser parameters can be set based on predictive numerical models. Attention must be paid that laser power density causes an increase in the compressive residual stress achieved only up to a certain limit, since above a certain value, no further improvement is achieved, thus high-lightening that saturation has occurred.

An other important aspect to take into consideration is the dielectric breakdown of the transparent layer. Power density, wavelength, pulse profile and pulse duration have a direct effect on the dielectric breakdown threshold of the transparent layer; this way it is important to control the optimum laser power density, which can be described as:

$$\rho = \frac{E}{t \frac{\pi}{4}} \quad (2.1)$$

where:

- E is the energy
- t is the pulse duration

So, the wavelength in combination with the laser power density acts on the dielectric breakdown, which can be regarded as the plasma absorption of the incoming laser pulse which results in a limitation to the generated shock wave. This way it is evident how the dielectric breakdown effect influences the real amount of energy reaching the component surface.

Also the laser spot dimension influence the residual stress field achieved. A larger spot size results in a bigger compressive residual stress imposed, since the shock wave decreases with $\frac{1}{r^2}$, since the shock wave propagates with a sphere geometry for a small diameter, while it propagates with a planar front, for bigger spot size, thus resulting in a reduction factor which goes only as $\frac{1}{r}$. Overlap parameter is defined in different ways by the different laser suppliers. In Universidad Politecnica de Madrid the percentage of overlap is defined as:

$$\%overlap = 100 * (1 - \frac{l}{d}) \quad (2.2)$$

where:

- d is the spot diameter
- l is the distance between two subsequent spots

The number of spots is equal to:

$$Numberofspots = \frac{L}{\rho} \frac{W}{l} \quad (2.3)$$

where:

- L is the coupon length
- W is the coupon width

The spot density can be defined as:

$$\rho = \frac{Numberofspots}{LW} \quad (2.4)$$

An other important aspect connected to laser shock peening is the clamping configuration and the choice of peening just one or two coupon sides. When peening a thin coupon on both sides, attention must be paid to the clamping solution as well as to the laser parameters adopted on each shot side, to avoid specimen deflection.

Toshiba laser technique is characterized by the use of round spots at low laser energy, with high overlap, in order to reduce the effect of surface wave focusing. Toshiba implements laser shock peening with small spots since it implements the technology without coating.

An other important factor in terms of effectiveness of the laser treatment for industrial applications is the equipment relative positioning, target, laser and lens systems. This way, a high challenge is represented by the need to develop portable laser system which can be effective during maintenance and manufacturing.

Optics relative positioning is important in determining the spot size in correspondence to the target surface, since this influences the power density achieved, which is regarded as a focus parameter in determining the predicted residual stress field, thus allowing the effectiveness of the treatment on fatigue.

Several factors contribute to the energy level effectively reaching the coupon surface, such as beam divergence, variance in the beam profile, thermal lensing effect and water splashing, but the most important seems to be the air breakdown.

Tests conducted at Witwatersrand University highlighted that the main energy losses are attributed to air breakdown phenomenon and losses in the optical mirror system. This way, it is important to cover each lens after treatment to prevent them from dust and vapour which can result in subsequent energy losses, thus resulting in uncertainties in the laser treatment repeatability.

To be sure to fully characterize the residual stress field achieved even if beam deviation are present, measurements have to be carried out at different locations and not just immediately aside the laser pattern. This would also make it possible to correctly evaluate the numerical predictions, which give continuous informations about the residual stress field achieved, and not just at some points, as provided for example by the incremental hole drilling technique.

When performing the laser peening process, temperature on the coupon treated surface can exceed the critical one, this can lead to a change in the mechanical properties of the material which needs to be evaluated.

Great difference in the residual stress field achieved is highlighted when changing the scanning and stepping laser direction. At this purpose let's think to a L-T coupon which is peened as in the following ??:

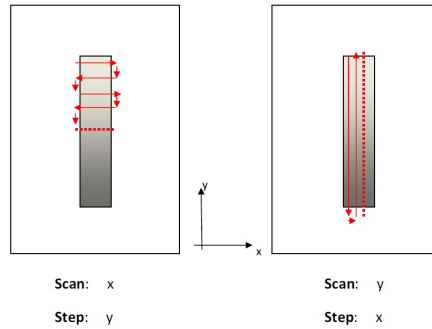


Figure 2.5: Laser scanning and stepping directions

The first configurations allows to achieve, by use of the same laser parameters, a higher compressive residual stress field. This, in accordance with the grains distribution due to the machining directions, constitutes a major obstacle to the propagating crack, which is supposed to grow in x direction.

An other important aspect to be taken into account when implementing fatigue test is the coupon clad surface, since this can act as a crack growth promoter.

2.3. LASER SHOCK PEENING CHAPTER 2. LASER SHOCK PEENING

In studying of fatigue, a parameter which is of primary importance is the surface finishing, which is mainly characterized by the following parameters:

- lay
- surface roughness
- waviness

Surface roughness can be measured in two way, by contact or without contact. Roughness can be evaluate dby two main parameters, which are:

- arithmetic mean roughness, which is a statistical descriptor that gives the average distance between the surface and the mean line, considering all the points along the profile
- peak roughness , which can be defined as the sum of the largest peak and the largest valley of the profile within the sampling length

Surface integrity descriptor are fundamental to make it possible to evaluate the displacement parameter, which is regarded as the calibrating one for the all explicit Johnson - Cook model developed to make predictions about the residual stress field achieved by laser peening treatment.

Tests conducted at Witwatersrand university, about hardness measurements on the treated samples varying the laser power density from 3 to 6 and then 9 $\frac{GW}{cm^2}$, and the water layer thickness from 1.5 to 8 mm, showed that on the contrary of what expected, the highest hardness wasn't achieved for the 8 mm water layer thickness, resulting in the confined bubble to cause a secondary wave through the material. The highest hardness has been achieved by coupons treated with the thinner water layer. Two possible explanations to this behavior are:

- The thicker the water layer, the bigger the energy loss through the water , and the less effective the energy reaching the sample
- the thicker the water layer, the more the electric breakdown of the water due to the plasma being generated before the coupon surface

The higher energy losses have been registered at Witwatersrand university at 9 $\frac{GW}{cm^2}$ maybe due to the dielectric breakdown, as well as to absorption, negating the effect of a secondary shock wave. Alternatively, the higher power density didn't result in the higher compressive residual stress due to the occurred material saturation. The energy losses registered for the thicker water layer associated to the higher power density can be the reason of the lower micro-hardness.

An other important aspect connected to the laser peening process implementation, as highlighted by Witwatersrand University, is that the lower power density with the bigger laser spot size resulted in the higher compressive residual stress field achieved. this can be due to the fact that bigger spot size produce shock wave that penetrate deeper into the material due to the planar wave attenuation.

2.4 Motivation

Recent incrementing interest on composite, due to the development of A 350 and Boeing 787, focused the research interest mainly on composite structures. Anyway, a lot of aircraft are still made of metallic components, thus research in this sense is useful. Even if Laser Shock Peening has been introduced in 1970, a lack of information in the numerical prediction of the compressive residual stress field induced by the treatment and associated with the best laser set up parameters choice is highlighted.

Due to the high velocity of the process, the high laser pulse involved is of the order of GW/cm^2 and duration time of 10 -100 nsec, the LSP is regarded as adiabatic. Cause of this, the LSP numerical simulations are referred only to the mechanical macroscopic effect, even if the process, involving plasma at high temperatures, can microscopically alter the component surface, thus not contributing to a change in the compressive residual stress field achieved, which mainly characterize the components depth, but can influence the fatigue behavior of the interested structure, since defects are recognized to start mainly from the surface layer.

Aircraft industries increasing interest is focusing on the development of portable laser systems able to allow treatment to repair and maintenance during the normal aircraft operations, using hangar and airline maintenance facilities. An attractive property of laser shock peening is its ability to already access areas non reachable with traditional treatments, such as shot peening. To be applicable directly in hangar or airlines facilities, laser shock peening process needs more automation; application of an ablative layer as well as other operations for preparing the surface to the treatment, in fact, are still manual. In order to increase fatigue life performances of aeronautical components, thin panels representative of fuselage skin have been laser peened and fatigue tests carried out to investigate the parameters, laser set up and geometry, which contribute to a slower fatigue crack propagation.

Bibliography

- [1] Domenico Furfari. *Laser Peening in commercial aeronautical applications*, IV International Conference on fatigue and related phenomena, Madrid, 5-10 May 2013.
- [2] Hemanet Amarchinta. *Uncertainty quantification of residual stresses induced by laser shock peening simulation*, doctoral Thesis, Wright State University, 2010.
- [3] Fainard, Wilcox, Gallagher, Williams. *Laser Shock Induced microstructural and mechanical property changes in 7075 aluminium*, journal of applied physics, vol43, No.9, 1972, pp.3893-3895.
- [4] Fabbro, Fournier, Ballard, Devaux, Virmont. *Physical study of laser produced plasma in confined geometry*, journal of applied physics, vol68, No.2, 1990, pp.775-784.
- [5] Fairand, Clauer, Jung, Wilcox. *Quantitative assessment of laser induced stress waves generated at confined surfaces*, Applied Physics Letters, Vol.25, No.8, 1974, pp. 431-433.
- [6] Peyre, Berthe, Fabbro, Sollier. *Experimental determination by PVDF and EMV techniques of shock amplitudes induced by 0.6-3 ns laser pulses in a confined regime with water*, journal of physics D: Applied Physics, vol.33, No 5, 2000, pp498-503.
- [7] Fairand and Clauer. *Laser generated stress waves: their characteristics and their effects to materials*, 1978.
- [8] Berthe, Fabbro, Peyre, Tollier, Bartnicki. *Shock Wave from a water confined laser generated plasma*, journal of applied physics, vol 82.
- [9] Marti Lopeza, Ocana, Pineiro, Asensio. *Laser Peening induced shock waves and cavitation bubbles in water studied by optical schlieren visualization*, physics procedia, vol 12.
- [10] Vilata-Clemente, Gloystein, Frangis. *Principles of atomic force microscopy*, www.gbhenterprises.com, 2008.

- [11] Ding, Ye. *Laser shock peening: performance and process simulation*, Woodhead publishing ltd, Cambridge, England, 2006.
- [12] Clauer. *How did we get here? a historical perspective of laser peening*, first international conference on Laser Shock Peening, Houston, TX, Dec 15-17 2008.
- [13] Hemanet Amarchinta. *Uncertainty quantification of residual stresses induced by laser shock peening simulation*, doctoral Thesis, Wright State University, 2010.
- [14] Fainard, Wilcox, Gallagher, Williams. *Laser Shock Induced microstructural and mechanical property changes in 7075 aluminium*, journal of applied physics, vol43, No.9, 1972, pp.3893-3895.
- [15] Fabbro, Fournier, Ballard, Devaux, Virmont. *Physical study of laser produced plasma in confined geometry*, journal of applied physics, vol68, No.2, 1990, pp.775-784.
- [16] Fairand, Clauer, Jung, Wilcox. *Quantitative assessment of laser induced stress waves generated at confined surfaces*, Applied Physics Letters, Vol.25, No.8, 1974, pp. 431-433.
- [17] Peyre, Berthe, Fabbro, Sollier. *Experimental determination by PVDF and EMV techniques of shock amplitudes induced by 0.6-3 ns laser pulses in a confined regime with water*, journal of physics D: Applied Physics, vol.33, No 5, 2000, pp498-503.
- [18] Fairand and Clauer. *laser generated shock waves: their characteristics and their effects to materials*, 1978.
- [19] Berthe, Fabbro, Peyre, Tollier, Bartnicki. *Shock Wave from a water confined laser generated plasma*, journal of applied physics, vol 82.
- [20] Marti Lopeza, Ocana, Pineiro, Asensio. *Laser Peening induced shock waves and cavitation bubbles in water studied by optical schlieren visualization*, physics procedia, vol 12.
- [21] Vilata-Clemente, Gloystein, Frangis. *Principles of atomic force microscopy*, www.gbhenterprises.com, 2008.
- [22] Ding, Ye. *Laser shock peening: performance and process simulation*, Woodhead publishing ltd, Cambridge, England, 2006.

CHAPTER 3

LSP Numerical Simulations

3.1 Laser Peening Treatment

Laser Peening process is based on the adoption of a laser with power density of several GW/cm^2 for short duration time, 1-50 ns. The process can be implemented either with or without an ablative layer coating. Usually the component surface is covered by black paint and subsequently by a water layer which acts as transparent overlay. The opaque coating is regarded as a sacrificial material to prevent the coupon surface from thermal effect arising from the plasma acting during the peening treatment. The opaque coating partially vaporizes into plasma when hit by laser, this is why it's commonly called ablative layer. The transparent overlay instead acts in confining the expanding vapor and plasma against the target surface. This way, a higher pressure is generated, which exceeds the the yield strength of the material. As previously mentioned LSP treatment can also be performed without ablative layer and water coating; these two different strategies result mainly in different dimension of the spot size.

3.2 Comparison with Shot Peening

Shot Peening treatment can be regarded as a cold working process. Shot peening consists of small spherical media, usually made of steel, glass or ceramics, impacting (shot) on the surface of the component of interest. Each impacting ball leaves small dimples on the treated surface. The surface fibers of the material are loaded in tension whereas that below, which try to restore the surface to its original shape, are loaded in compression. Shot peening advantages can be summarized in:

- handy equipment need for process implementation
- applicable to large or small (even if not too much) areas

3.3. LSP NUMERICAL MODELING 3. LSP NUMERICAL SIMULATIONS

- cheap

The main disadvantages are connected to:

- random nature of impacts make the process not repeatable
- non uniform residual stress distribution
- impossibility to access some areas prone to fatigue
- small balls after shot contaminate the surrounding environment
- insertion of compressive residual stresses only at lower depth under the component treated surface
- more roughened surface in respect to laser shock peening treatment

Roughness induced by traditional shot peening can be of such an entity to highlight the need for the manufacturer to remove it, since surface discontinuities are well know to act as crack initiation points. Nevertheless, surface removal can result in compressive residual stress removal as well, thus, since shot peening introduces this favorable stress state only at small depth under the surface of the treated component, surface removal can result in a complete loss of benefit. Laser Shock peening cannot be regarded as an alternative to traditional shot peening, but to the chance it gives to adjust and optimize in real time the spot geometry and main parameters acting on the reachable compressive residual stress, it can at least be used together with SP to treat both large areas at low cost and otherwise inaccessible structural parts prone to fatigue phenomena.

3.3 LSP Numerical Modeling

Peyre et al. in 2003 explained the first attempt to use the Johnson - Cook model to make predictions about the residual stress field achieved by means of laser peening treatment within the Abaqus software. In the corresponding paper it is reported the plot linking the laser power density used to implement the laser process, with the pressure value adopted for the numerical simulation, which is already used.

Ding and Ye in 2003, developed a three dimensional elastic perfectly plastic model to describe the LSP process. In order to simulate a laser treatment involving such high strain rates, they introduced damping effects and material viscosity, to limit the numerical oscillations.

Ocana et al in 2004 developed a model called Shocklas able to study the laser plasma interaction, and make predictions of the thermo-mechanical input to subsequently use to determine the residual stress field induced by the laser.

Wu and Shin in 2005 and 2007 mainly tried to convert the laser pulse to the pressure pulse; no measurement of the shock wave pressure has been made in this case. They divided the plasma contribution into two parts, the breakdown and the confined plasma; according to them only the confined plasma contributes to the generation of the shock wave.

Warren, Gou and Chen in 2008 developed an Abaqus subroutine in order to simulate the laser shock peening process taking into account the temporal, spatial and intensity effects on the compressive residual stress field achieved.

3.3. LSP NUMERICAL MODELING 3. LSP NUMERICAL SIMULATIONS

Achinth and Nowell in 2011, adopted the Eigenstrain approach to predict the residual stresses left by laser peening treatment. They started from the estimation of the plastic strain distribution achieved by the simulation of the LSP process in an explicit software, and since it's:

$$\epsilon = \alpha \Delta T \quad (3.1)$$

assuming ΔT equal to 1, then the strain can be regarded as the α parameters to be input in a subsequent static analysis, as predefined field, in the initial step. The same procedure has been adopted within this work of thesis to make an estimation of both the residual stress field and displacements occurring after the laser treatment.

Ding and Ye in 2006 explained the importance of the proper simulation time choice, which has to be twice the pressure pulse duration, in order to achieve saturation of plastic deformations. This work shows the importance to define the proper time simulation in order to not have too expensive computational analyses as well as reliable numerical results, without use of damping effects and viscosity parameters, which help in controlling high frequency oscillations through the all dynamic analysis.

A full explicit approach results in a computationally expensive way of proceeding, especially due to the predictions of the residual stress state, since it is very slow in reaching the static equilibrium. In the work by Ding and Ye it is reported that an all implicit way of proceeding is expensive as well in determining the dynamic stresses. Explicit plus implicit analysis will provide the faster numerical results.

The correct duration of the explicit analysis can be checked evaluating the kinetic and internal energies trend. On the other hand, no literature has been found to evaluate the correct duration of the implicit analysis, but it can be easily determined looking at the changes in the stress state of the material.

Amarchintha et al in 2009, published a paper in which they assess that in case of thick target, it can be simulated by infinite elements whereas, for thin coupon this is no longer possible, since this way the shock wave interaction arising between the incoming one and that reflecting from the back side of the component cannot be simulated.

The computational efficiency of the model representative of the laser peening treatment is difficult because of the complex nature of the phenomenon, since it involves both elastic and plastic effects, and because of the small time increments required. In fact, the LSP involves a high pressure pulse with a small time duration, but it requires a much longer time for the material to reach a subsequent equilibrium state. typical pressure time scale are in the order of nanoseconds, whereas the spring-back time is in the order of milliseconds.

Experimental implementation of the laser peening treatment is expensive as well as expensive are the measurement techniques adopted to characterize the induced residual stress field, which can be summarized in X-Ray diffraction, Neutron Diffraction, Synchrotron Diffraction, Stress contour Method and incremental hole drilling, which are usually compared or implemented together to be able to fully characterize the RS field achieved both on the surface and depth of the component making use of the main benefits of each technique. Anyway, the laser transient nature make real time in situ measurement very challenging. All these aspect highlight the need to develop a robust, reliable, cost and time

3.4. EXISTING MODELS FOR LSP NUMERICAL SIMULATIONS

effective numerical model to predict the residual stress field associated to a defined material, geometry and laser parameters.

Main parameters which is possible to optimize are:

- irradiance
- pulse duration
- number of layers
- coverage
- laser power density
- geometry of the target (thickness, shape, areas prone to fatigue, edges)
- laser peening sequence
- single or double side peening
- environmental conditions, such as ablative layer and tamping coat

3.4 Existing Models for LSP Numerical Simulation

Difficulties in the laser peening simulations are mainly due to the inherent physical complexity of the phenomenon itself, which includes the coexistence of different material phases, such as plasma, interacting each other.

3.4.1 Explicit/Implicit LSP Analysis

Braisted and Brockman were the first to develop a 3D model of LSP on the Abaqus software, ??:

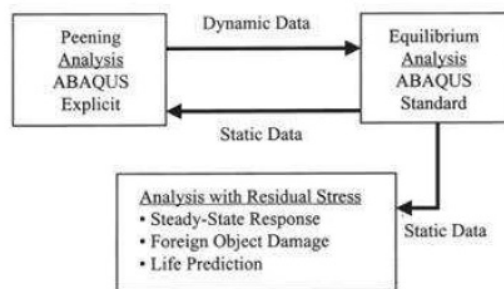


Figure 3.1: Braisted and Brockman LSP numerical procedure

Braisted and Brockman idea consisted in performing an Explicit Abaqus analysis until all the plastic deformation has occurred, which usually happens in a running time which is two orders of magnitude longer than the duration of the laser pulse. After that, the simulation is stopped and an Abaqus standard procedure is started, having as input the stresses, strains and displacement data coming from the previous analysis; this last step provides the residual stress field

3.4. EXISTING MODELS FOR LASER-INDUCED PLASMA CALCULATIONS

under static equilibrium conditions. This procedure is based on the benefit of the adoption of both an Explicit and Standard procedure. In fact, Abaqus Explicit is a non linear explicit time integration finite element code specifically designed for short duration transient analyses, whereas Abaqus Standard is a non linear implicit time integration finite element code used primarily for static or natural frequency calculations. Explicit methods are the most suitable for high speed non linear problems but have a lot of convergence issues, while the implicit ones are more robust and reliable but they imply prohibitive computational expenses in solving dynamic problems.

3.4.2 ShockLas Prediction Tool

The lots of the models present in the literature does not account for the plasma dynamics. In 2004 Ocana et al. presented Shocklas method to predict the residual stress field arising from the LSP treatment. Shocklas method consists of different phases, such as:

- Plasma dynamic analysis and investigation of breakdown in the dielectric media
- hydrodynamic aspects connected to the plasma expanding between the confinement layer and the base material
- shock wave evolution in bulk material

Each of the reported phases is developed in Shocklas in specific modules, respectively:

- HELIOS, an 1-D code used to simulate the dynamic evolution of the laser induced plasma
- LSPSIM, an 1-D code used to estimate the pressure wave effect on the target treated via LSP
- HARDSHOCK, a code which enables to solve the shock propagation problem characterizing the treated material on the basis of the time-dependent pressure profile calculated by HELIOS and LSPSIM

Doing so, Shocklas is able to represent the thermal and mechanical response of the material to the propagating shock wave and plasma induced by the laser treatment.

Shocklas calculation scheme is reported in ??:

A 3-D version of Shocklas has been implemented on the commercial software Abaqus, using an explicit differentiating strategy for the representation of the first fast shock propagation and a standard implicit differentiating procedure to analyze the final residual stress equilibrium state. Shocklas, being based on an integrated laser-plasma routine, based on a realistic material EOS, allows to study the LSP process starting from laser-plasma interaction. On the other hand, a so accurate representation of the LSP process results in high computational costs, which can be acceptable only from a research point of view, whereas from the industrial side it makes non-sense going so deep in detail to the laser physics requiring so high computational time, but providing a residual stress field

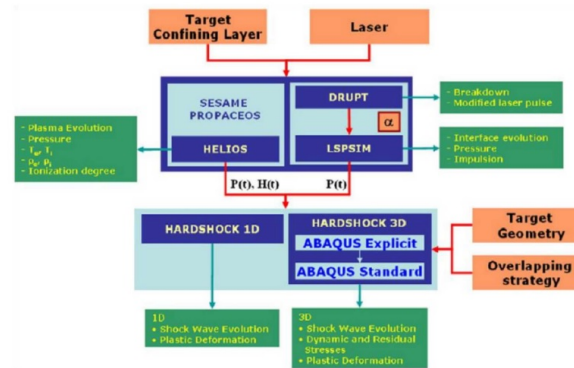


Figure 3.2: Shocklas Scheme

associated to a laser set up parameters specific for the material and geometry under investigation; this way a fast analysis on fatigue can be implemented to check potential benefits of LSP both on maintenance and production.

3.5 Johnson-Cook Modeling Technique

The background of the present thesis is a set of numerical analyses, developed in the past years, in order to investigate the laser parameters influence on the residual stress distribution on simple geometrical configurations. A numerical model calibration has been achieved by means of a Johnson-Cook material model. A deep analysis of the effects of the involved parameters in the residual stress field and displacement estimation has been performed. Further analyses have been developed to make predictions on different geometries of interest for the aeronautical industries. The performed analysis proved the Johnson -Cook model to be:

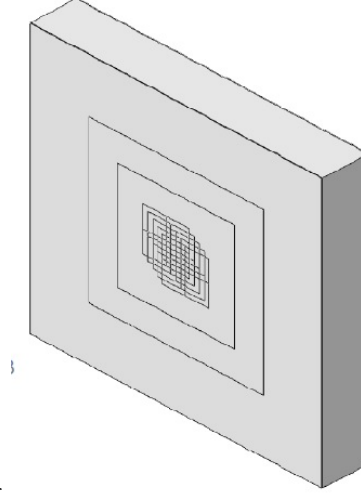
- **User friendly**, since based on the commercial software Abaqus, that is widespread in most of the industrial companies; it can be implemented on python scripts which are easy to handle and based on gui interfaces
- **Reliable**, the model has been calibrated on residual stresses and displacement parameter based on an intensive test campaign involving different peening settings and coupon geometries
- **Time and Cost Saving Based on the Abaqus Explicit Code** which guarantees the convergence even for the first fast impact phase.

In the development of a numerical model to represent the laser peening treatment, some main parameters have to be taken into account, such as:

- laser beam parameters
- overlay conditions
- material properties

3.5. JOHNSON-COOK MODELING TECHNIQUE IN NUMERICAL SIMULATIONS

Abaqus software is based on a CAE tool which enables to create a 3-D model. The geometry of the target has to be defined starting from a 2-D sketch; the 3-D model results from one of the typical manufacturing process which is possible to implement, such as extrusion and cutting. While defining the geometry, partitions have to be made in order to be then assigned by surfaces to represent each laser spot.



partition.jpg

Figure 3.3: Partition and Overlap adopted for a tested laser peening configuration

Each edge created by the created partition needs to be assigned by seeds to guarantee a good mesh quality, thus resulting in a shorter CPU's time.

The Abaqus explicit procedure adopted, based on Johnson- Cook material model, does not take into account the physics of the phenomenon, thus the plasma dynamics.

In the laser peening treatment, the residual stress field is introduced by shock wave originating after the laser impact on the coupon surface and the plasma formation, ablation and confinement. The hydrodynamic discontinuity of the shock front can be described by the following equations ??, ??, ??:

Mass conservation

$$\rho_0 U_S = \rho(U_S - U_P) \quad (3.2)$$

Momentum conservation

$$(P - P_0) = \rho_0 U_S U_P \quad (3.3)$$

where the subscripts refer to:

- 's ', shock wave quantities
- 'p ', particle quantities

3.5. JOHNSON-COOK MODEL IN NUMERICAL SIMULATIONS

Energy conservation

$$(E - E_0) = \frac{1}{2}(P + P_0)(V + V_0) = \Delta E \quad (3.4)$$

- ‘0’, undisturbed conditions

Equations ??, ??, ??, give rise to a undetermined system of five variables (ρ , P , U_P , U_S , E). To solve the problem, there is the need to introduce the equation of state, (EOS) which describes the behavior of the process and material. The choice of the EOS which better suites for describing the LSP process is not easy, since LSP is characterized by strain rates up to 10^6 sec^{-1} . At so high strain rates, the material exhibits changes in both the elastic modulus and the Yield strength. Johnson-Cook model describes the residual stress acting on the material as a product of three terms, describing respectively:

- strain hardening
- strain rate
- thermal effect

The Johnson - Cook model equation is ??:

$$\sigma = [A + B\epsilon^n][1 + C \ln \frac{\dot{\epsilon}}{\dot{\epsilon}_0}][1 - T'^m] \quad (3.5)$$

where:

$$T'^m = \frac{T - T_r}{T - T_m} \quad (3.6)$$

being T_r the room temperature, T_m the melting temperature, and, A , B , n , C , $\dot{\epsilon}_0$ parameters determined experimentally by Split Hopkinson bar test, valid for strain rates up to 10^4 sec^{-1} . This represents a limit in the adoption of the JC material model, since parameters involved are determined experimentally at strain rates which are two orders of magnitude less then that involved in the laser process; also, the Abaqus software gives reliable results for strain rates up to 10^4 sec^{-1} .

Looking more in detail to the involved parameters:

- A is the initial yield strength at room temperature
- n is the strain hardening
- m represents the thermal softening
- C is the strain rate sensitivity

An other important phase in the numerical model implementation is the load description. As already said, the Johnson- Cook model and the Abaqus explicit procedure adopted doesn't describe or account in detail the laser physics, such as the plasma dynamics. The laser effect is introduced just as a pressure load, which is described by its realistic temporal profile ??:

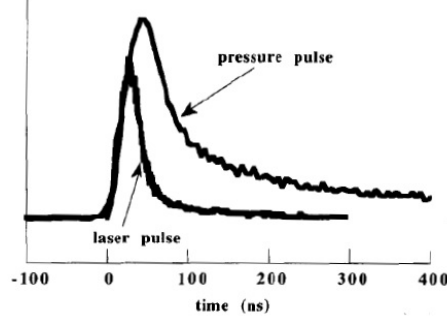


Figure 3.4: Laser Pulse temporal profile

Due to the plasma confining effect, the laser decay is slower than the initial rising to the pressure peak. In previous works, different geometries representative of the laser pressure profile have been examined, including the triangular symmetric, trapezoidal and triangular asymmetric; at the end, comparison between the different configurations and the achieved residual stress field with the experimental ones, lead to the conclusion that the shape which is more representative of the real pressure trend is ??:

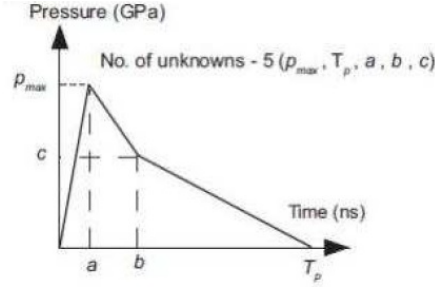


Figure 3.5: Laser pressure profile, numerical shape adopted

A correlation between the laser settings and the pressure configuration to be used in the Abaqus modeling representation, is expressed by the following relationships ?? which are valid when considering the plasma as a perfect gas:

$$P(GPa) = 0.01 \sqrt{\frac{\alpha}{2\alpha + 3}} \sqrt{Z(gcms^{-1})} \sqrt{I_0(GWcm^{-2})} \quad (3.7)$$

where:

- I_0 is the laser power density
- P is the pressure
- Z is the reduced shock impedance between the target and the confining medium
- α is the efficiency of the interaction

3.5. JOHNSON-COOK MODELING TECHNIQUE IN NUMERICAL SIMULATIONS

In a water confinement mode equation ??, becomes ??:

$$P(GPa) = 1.02\sqrt{I_0(GWcm^{-2})} \quad (3.8)$$

The load induced by the laser action can be implemented using an Abaqus explicit load module called ‘pressure’. Each pressure pulse has to be assigned to each created partition. Even if a uniform spatial pressure profile is easier and faster to implement, previous works showed that a non uniform spatial profile gives better results, thus characterized by less discontinuities between the peened and unpeened areas. The loading profile is described within steps which include the definition of:

- step duration
- numerical damping
- integration method
- output request

The analysis step are defined as dynamic explicit. The stability limit definition is based on the element length L_e , and the wave speed of the material C_d , where:

$$c_d = \sqrt{\frac{E}{\rho}} \quad (3.9)$$

In the step module it is possible to set other numerical devices such as artificial damping and mass scaling.

The parameters adopted for the first implementation of Johnson - Cook model to describe the material behavior when subjected to LSP treatment are reported in the following table ??:

Pressure Temporal Profile	Triangular	Simplest temporal profile
Full Width Half Maximum	60 ns	Pressure Profile peak at this point of the temporal profile
Artificial Damping	Default	-

Table 3.1: Numerical Parameters adopted in the first modeling attempt

The Johnson -Cook parameters describing Al 7050-T7451 are reported in the following table ??:

A [MPa]	B [MPa]	n	C	ϵ_0	m
490	207	0.344	0.005	1	1.8

Table 3.2: JC parameters, Al 7050-T7451

Starting from previous studies it has been highlighted that also the element mesh size has a great influence on the residual stress results. A rough or discontinuous mesh causes longer simulation time and inaccuracy of the results, whereas the use of mesh elements characterized by too small dimensions lead

3.5. JOHNSON-COOK MODELING TECHNIQUE IN NUMERICAL SIMULATIONS

to residual stress values exceeding the experimental ones. The use of a mesh which is too refined does not necessary lead to a more accurate prediction, but can result in numerical instability especially when associated to highly dynamic analyses. This is why, previous studies have been addressed to mesh refinement. The coupon geometry with a single central shot used for the mesh sensitivity study is reported in ??:

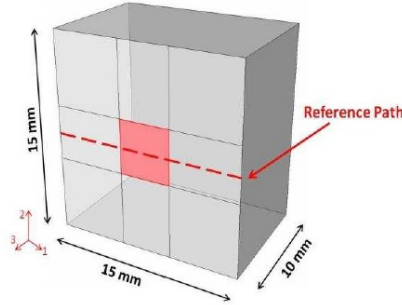


Figure 3.6: Single Peen geometry used for mesh sensitivity studies

Cubic mesh element type C3D8R of different dimension have been used and the achieved results compared with experimental data. C3D8R element is a (R) reduced integrated element, solid integrated brick with 8 nodes presenting 3 degrees of freedom, thus the three translations, for each node. Previous studies highlighted that the difference in the residual stress field achieved can go up to 120 MPa, depending only on the different choice of element size. From a deeper analysis of the achieved results it has been noticed that a strong deformation took place in the loading direction whereas just small deformations occurred in the other two directions. To avoid this kind of unwanted deformations, the element size has been refined, having a smaller dimension in the loading direction but enlarging the other two so to not give rise to too expensive analyses. A finer mesh has been created only in correspondence to the laser shot and its surroundings to not increase the computational time requested for simulation. By use of biased seed technique the mesh has been refined only in correspondence to the shot in coupon depth direction, and then increased gradually, to not result in instability problems, to a coarser one.

In previous works, by use of this approach, and comparison with the experimental results, the better mesh refinement has been set. The subsequent step regarded an investigation on the material defining parameters.

Since the LSP process involves high velocity phenomena and shock wave material interaction, the damping effect connected to the use of the bulk viscosity parameter can result in significant influence on the achieved results.

Abaqus Explicit allows to damp volumetric straining by means of two parameters:

- Linear Bulk Viscosity
- Quadratic Bulk Viscosity

Material bulk viscosity limits the numerical oscillations of high speed and high strain rate processes like laser shock peening. Regarding the damping

3.5. JOHNSON-COOK MODELING TECHNIQUE IN NUMERICAL SIMULATIONS

effects, in the Abaqus software they are indicated as linear and quadratic bulk viscosity; the former damps the noise associated to the high frequencies, whereas the latter redistributes the shock to various elements along the shock front thus preserving the elements from collapsing under high velocity gradients.

Previous studies highlighted a great influence of the bulk viscosity parameter in reaching the equilibrium state. Using a linear bulk viscosity value equal to 6, thus an order of magnitude greater than the default one, leads to an equilibrium solution, whereas the use of a LBV parameter equal to 0.06, thus an order of magnitude less than the default one, results in higher residual stresses and displacement achieved, when compared to the experimental ones. Moreover, the quadratic bulk viscosity has been increased as well, leading to the best set up values of 6 for LBV and 1200 for QBV.

JC material parameters reported in ?? and adopted in previous studies, have been found in the literature. Studies conducted on those parameters show a discontinuity in the stress - strain curve after the yield strength is reached ??:

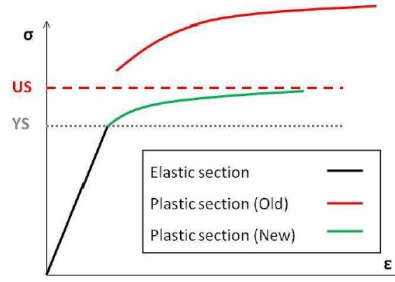


Figure 3.7: Stress-Strain Curve for JC parameters found in the literature vs new for curve continuity

The new JC parameters, defined on the basis of that found in the literature, but giving rise to a continuous stress-strain curve, are reported in ??:

A [MPa]	B [MPa]	n	C	ϵ_0	m
435	110	0.03	0.001	1e06	1.8

Table 3.3: JC parameters, Al 7050-T7451, continuous stress-strain curve

Despite the use of the new JC material parameters and increased bulk viscosity values, a big gap has been highlighted when comparing the numerical results achieved for the displacement parameter with the experimental ones. An investigation on the main parameters involved in the material description, showed that the only one influencing the resulting displacement values is the Yield strength. A matching with the experimental results has been found setting the yield at 80 MPa. It is evident that 80 MPa is not representative of the yield point of aluminum 7050-T7451; this leads to the conclusion that eventually the model doesn't take into account some aspects related to the surface phenomena induced by the laser treatment, such as temperature effect due to the plasma material interaction, or the presence of the ablative layer.

Crucial point of the analyses is the numerical simulation of the ablative layer. The numerical results achieved have been compared with the experimental

3.5. JOHNSON-COOK MODEL IN THE NUMERICAL SIMULATIONS

data coming from Al 7050-T7451 coupon shot peened by Metal Improvement Company (MIC) at Earby, England. MIC laser system is characterized by a Nd:glass laser delivering beams typically at 25 Joules at 18 ns. Before performing the laser treatment, MIC places by hand a thin aluminum foil, 100 μm thick, on the coupon surface. That foil is fixed on the coupon surface by means of a thin glue layer. Aluminum foil plus thin glue layer, result in what called the ablative layer. The ablative layer is so called since it partially vaporizes during the treatment. The above mentioned layer is covered by a water layer 1-3 mm thick. The remaining layer has to be removed after the treatment.

The ablative layer has been introduced in the numerical model as a perfectly plastic material showing a yield point of 10 MPa. The glue has not been represented since its effect on yield is regarded as negligible. The ablative layer has been geometrically defined by means of a partition on the coupon surface. No discontinuity condition has been set at the interface between main target body and ablative layer.

The dynamic of the shock wave can be better understand looking at the picture ??:

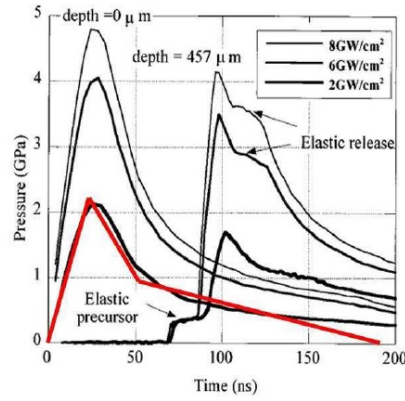


Figure 3.8: Shock Wave Profile found in the literature

Picture ?? shows the shock wave profile as numerically simulated at 0 and 457 μm depth., as a function of time, 25 ns as Full Width Half Maximum (FWHM), at different laser power densities, such as 2, 6 and 8 GW/cm^2 . From the pressure profile at 0 μm depth, thus on the coupon surface, in a water confined regime, it is highlighted that the shock wave is two time longer than the pulse duration, 50 ns vs 25 ns, due to the plasma cooling phase. Due to this velocity difference between the elastic wave reflecting from the coupon back and the plastic wave hitting the coupon front surface, the incoming shock wave amplitude is reduced. Accounting for this shock wave behavior, the pressure temporal profile has been set as in ??:

The first loading step is characterized by the application of the boundary conditions, set in the initial step, and the application of the laser pressure describe by the reported ?? temporal profile.

The pressure magnitude associated with the laser power has been defined by means of ??:

3.5. JOHNSON-COOK MODELING TECHNIQUE NUMERICAL SIMULATIONS

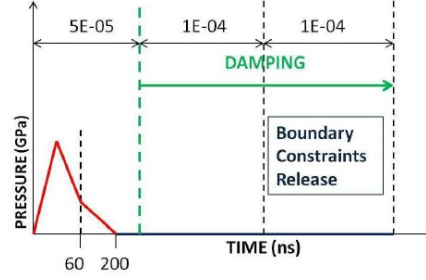


Figure 3.9: Pressure temporal profile

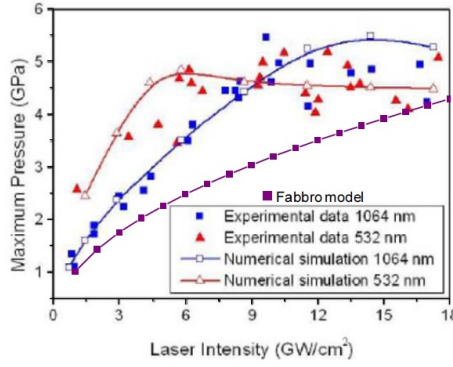


Figure 3.10: Relation between laser power and pressure loading

At this first loading step no artificial damping is applied in order to not invalidate the plastic deformations induced. The artificial damping effect is input only in the unloading and relaxation step, where oscillations connected to the shock wave dynamic arise, as previously described.

After running some simulations with a uniform spatial profile, discontinuity problems at the interface between the peened and unpeened area have been highlighted, due to the pressure variation from zero to thousand of MPa at the boundaries. This lead to the implementation of a distributed spatial pressure profile, characterized by a trapezoidal shape.

The boundary conditions have to be set firstly in the initial step. In this step they are implemented as Encastre on the back, not shot side, of the coupon. The loading step is characterized by the loading definition, both by a spatial and temporal profile as previously explained. BCs are propagated from the initial step. The BCs are changed only in case of two side peening configuration or in the relaxation step, where are set as reported in ??:

Investigations have been done on different geometries and loading magnitudes in the attempt to understand the ablative layer role.

Predictions on this loading fraction transferred parameter, as well as the evolution of the plastic dissipation energy and element plastic dissipation, is evaluated in order to check if the ablative layer acts as energy absorber, reducing the loading fraction (loading magnitude) transferred under the layer. This aspect has been investigated in order to check if the absence of matching between the numerical and experimental result, seen in certain analyses, can be due to this

3.5. JOHNSON-COOK MODELING TECHNIQUE IN NUMERICAL SIMULATIONS

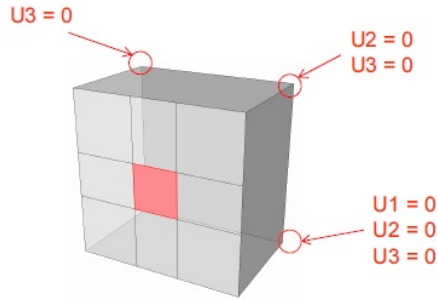


Figure 3.11: BCs in relaxation step

phenomenon of energy absorption. The analyses have been based on an all explicit approach involving only a single central shot. JC model used to evaluate not only the so called main specimen (coupon after the layer removal), but also the ablative layer, in order to check the temperature effect also on this numerical device.

Some of the main analyses parameters have been set as in the following:

- Laser Setting 3.2-18-1
- $P = 2500 \text{ Mpa}$
- Ablative Layer Yield=10 MPa
- Specimen Geometry:
 - $15 * 15 * 10 \text{ mm}$
 - Shot Spot $4*4 \text{ mm}$

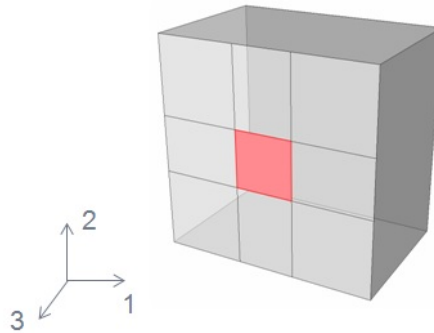


Figure 3.12: Specimen Geometry, Single Central Shot

- Specimen Components:
 - Main Specimen Body
 - Ablative Layer on Shot Surface, Thickness = 0.1 mm

3.5. JOHNSON-COOK MODEL IN THE FINITE ELEMENT SIMULATIONS

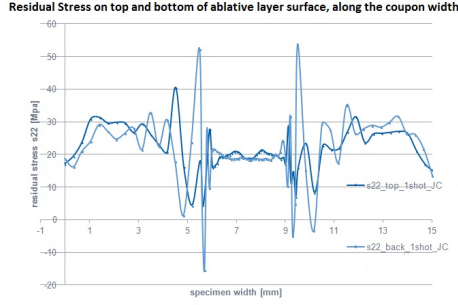


Figure 3.13: Residual stress at top and bottom ablative layer surfaces

Following, several plot referring to the main parameters involved in laser shock peening are reported in order to explain the ablative layer function.

As reported in ?? except for the shot borders (transition region), where the difference between the numerical results achieved in terms of residual stress on top and bottom ablative layer surfaces is bigger, the residual stress between these two parts is almost the same. The difference highlighted at the shot borders can be due to the possible distortion of the elements going from the loaded to unloaded, and from the finer to the coarser mesh. Nevertheless a small major value can be seen in correspondence to the upper part, as expected, acting the ablative layer as energy absorber.

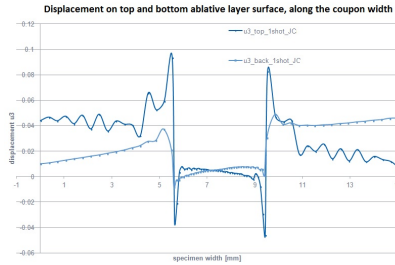


Figure 3.14: displacement parameter evaluated at top and bottom ablative layer surface

Symmetric conditions, in terms of displacement parameter, as in ??, can be seen, in correspondence to the end of the analysis, moving from the upper to the lower ablative layer surface.

Relating to the shot area, plastic deformation, as in ?? is bigger on the ablative layer lower surface, instead that on the upper one. Reminding that exactly that surface is connected to the so called main specimen (specimen after ablative layer removal), the question is how this connection between surfaces characterized by different yield values interacts with the results achieved, considering that the main specimen is characterized by a higher yield value; and how to correctly evaluate this aspect.

As reported in ??, element plastic dissipation is bigger on the back side of the ablative layer instead that on the upper one.

3.5. JOHNSON-COOK MODEL IN ABAQUS FINITE ELEMENT NUMERICAL SIMULATIONS

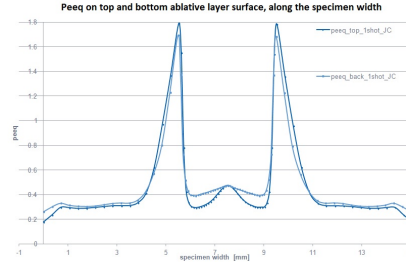


Figure 3.15: Peeq at top and bottom ablative layer surfaces

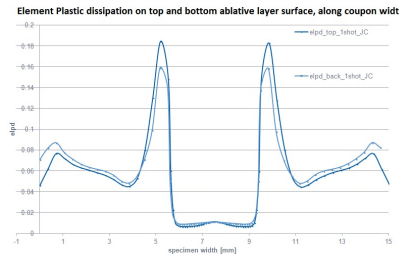


Figure 3.16: Elpd evaluated on top and bottom ablative layer surfaces

It is interesting to go more in detail with this temperature parameter, to check if it interferes someway with the numerical results achieved.

The temperature effect on the specimen subjected to LSP treatment can be checked by means of the Johnson- Cook model ??.

Being the temperature effect included in the JC model, it can influence the residual stress profile achieved after the LSP treatment, as well as the strain values and thus the induced displacement parameters. The analysis of this aspect can give an explanation of the ablative layer role. Abaqus software gives as field output request a parameter, called TEMP, which is the difference induced in terms of temperature, during and after the LSP treatment (to be check in different step time frames in order to check its evolution in time), in respect to the reference temperature imposed for the analysis; in the case under investigation, the room reference temperature has been set at the value of $20^{\circ}\text{C} = 293\text{ K}$.

Scheme ?? reports the adopted procedure to analyze the ablative layer effect in terms of temperature effect, to be defined in the loading step request selection.

The temperature effect has been checked for:

- Ablative layer top surface
- Ablative layer back surface
- Main Specimen body (specimen after ablative layer removal) Top (shot) Surface

The reported results are referred to the difference in temperature reached during the LSP treatment, in respect to the imposed room reference temperature, in this case of interest equal to $20^{\circ}\text{C} = 293\text{ K}$.

3.5. JOHNSON-COOK MODEL IN ABAQUS FINITE ELEMENT SIMULATIONS

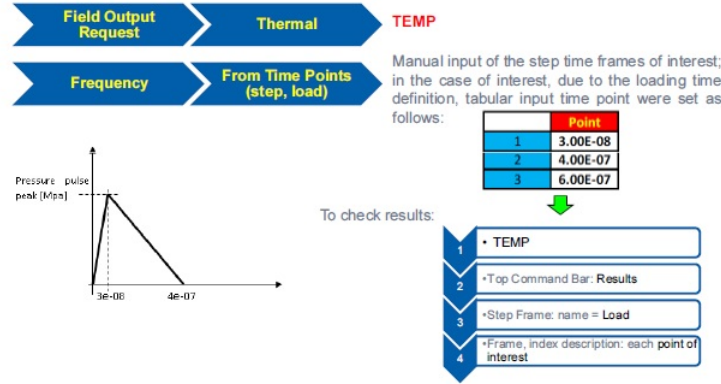


Figure 3.17: Procedure to evaluate the temperature effect

Based on the numerical results achieved in this way, an analytical check on the temperature influence has been implemented; starting on considerations on the Johnson-Cook model adopted to describe the LSP process, since ??:

$$\sigma = \underbrace{(A + B \epsilon^n)}_{\text{strain}} \left[1 + C \ln \left(\frac{\dot{\epsilon}}{\dot{\epsilon}_0} \right) \right] \underbrace{\left[1 - \left(\frac{T - T_0}{T_m - T_0} \right)^m \right]}_{\text{Temperature effect}}$$

Figure 3.18: Johnson - Cook influencing parameters

To evaluate the temperature effect, only the last term in the equation above has to be taken into account. The numerator term is that given by the Abaqus Field Output. So, being $T_m=908$ K and $T_0=293$ K, $m=1.8$, if:

$$\left[1 - \left(\frac{T - T_0}{T_m - T_0} \right)^m \right] \cong 1 \quad (3.10)$$

there is no consistent temperature influence on the achieved results. Considering the implemented pressure pulse profile ??:

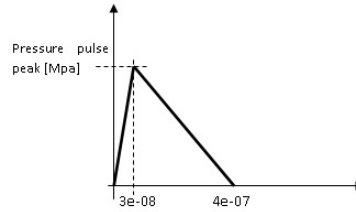


Figure 3.19: Numerically implemented pressure pulse profile

the temperature effect has been evaluated at 3e-08, 4e-07, 6e-07, 2.5e-04 and at the end of the relax time loading step:

- **Temperature at 3e-08 ??:** Temperature along the specimen width in correspondence to the pressure pulse peak; as expected the temperature on the top ablative layer surface is bigger than the one on the bottom part.

3.5. JOHNSON-COOK MODELING TECHNIQUE IN NUMERICAL SIMULATIONS

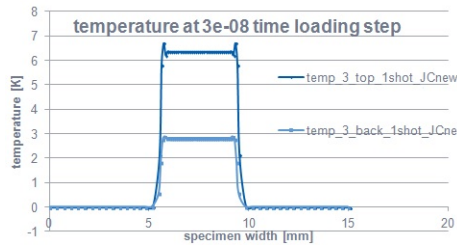


Figure 3.20: Temperature on front and back ablative layer surface

- **Temperature at 4e-07 ??:** Temperature along the specimen width at the end of the pressure pulse peak is about the same on both the top and bottom ablative layer surfaces

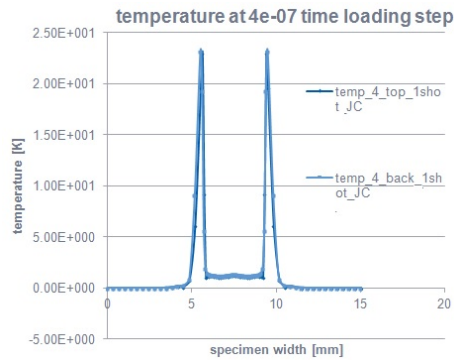


Figure 3.21: Temperature on top and back ablative layer surface

- **Temperature at 6e-07 ??:** In this time frame, at the end of the loading step, temperature is still the same between upper and lower ablative layer surface.

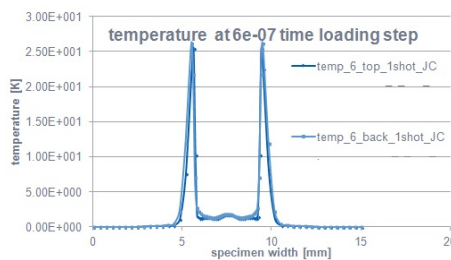


Figure 3.22: Temperature on top and back ablative layer surface at 6e-07

- **Temperature at 2.5e-04 ??:** also in this step time frame there is no big difference in terms of temperature between the upper and lower ablative layer surface.
- **Temperature at the end of the analysis, relax step ??:** Similar results between top and bottom ablative layer surface, with, as

3.5. JOHNSON-COOK MODEL IN FINITE ELEMENT SIMULATIONS

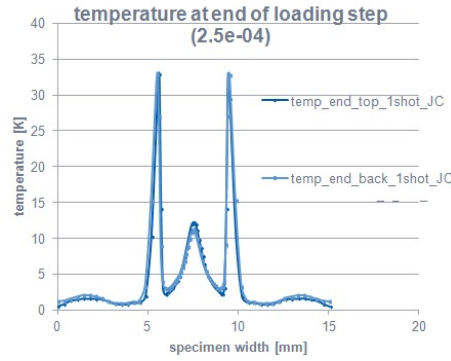


Figure 3.23: Temperature on top and back ablative layer surface at 2.5e-04

expected, a bigger temperature magnitude on the top layer surface, in correspondence to the shot area.

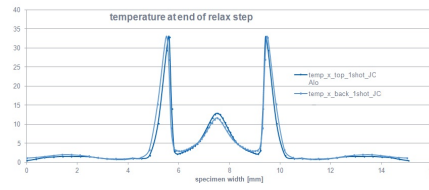


Figure 3.24: temperature on top and back of the ablative layer surface at the end of the analysis, relax step

Picture ??:

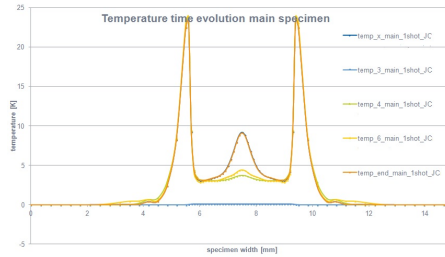


Figure 3.25: Temperature evolution on the so called 'main' coupon part

reports the temperature evolution during the laser treatment on the so called 'main' specimen part. On the main specimen part, the temperature, again in terms of difference in respect to the room reference one of $20^{\circ}\text{C} = 293\text{ K}$, increases following the arrow direction and stabilizing at the value reached at the end of the loading step, which is the same as that observed at the end of the complete analysis (end of final relaxation step).

Following, ??

shows the displacement parameter evolution on the ablative layer top surface. In respect to the shot area, the displacement value, as expected, increases on

3.5. JOHNSON-COOK MODELING TECHNIQUE IN NUMERICAL SIMULATIONS

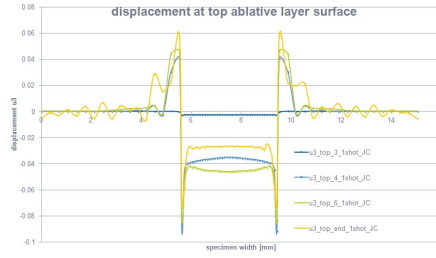


Figure 3.26: Displacement evolution on the ablative layer top surface

the top ablative layer surface, following the loading trend, increasing in absolute value, going from $3e-08$ to $4e-07$ to $6e-07$ and finally it reduces, in agreement with the loading distribution, going to the final equilibrium value at the end of the loading step.

Picture ??:

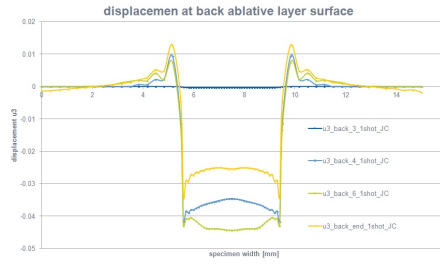


Figure 3.27: Displacement at back ablative layer surface

shows the displacement parameter trend at the back ablative layer surface. Same trend as for the top ablative layer surface, following the loading history, as expected; even if with different values in terms of displacement magnitude.

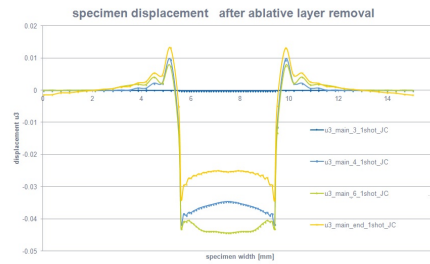


Figure 3.28: Specimen displacement evolution on main coupon part

Picture ?? shows the displacement parameter evolution on the main coupon part. According to the previously analyzed data, this parameter follows the loading trend, as well as the top and bottom ablative layer surface displacement do. The displacement value reached by the main specimen body, are, as expected, closer to that related to the back ablative layer surface, in agreement with the fact that the ablative layer acts as energy absorber.

3.5. JOHNSON-COOK MODELING TECHNIQUE IN NUMERICAL SIMULATIONS

Picture ??:

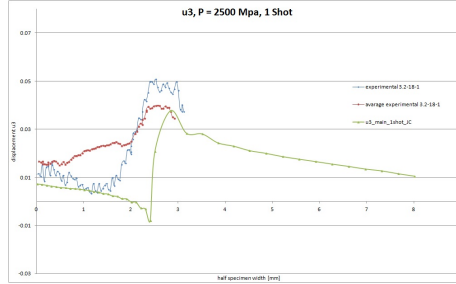


Figure 3.29: Comparison between the displacement parameter on main coupon part with experimental results

shows the difference in the displacement parameter between the main specimen body, thus after ablative layer removal, and the experimental results.

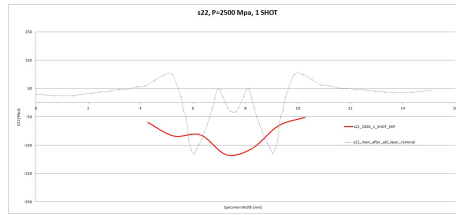


Figure 3.30: Residual stress achieved on main coupon part compared to the experimental results

Picture ?? shows the displacement evolution until the end relax step which is compared with the experimental results.

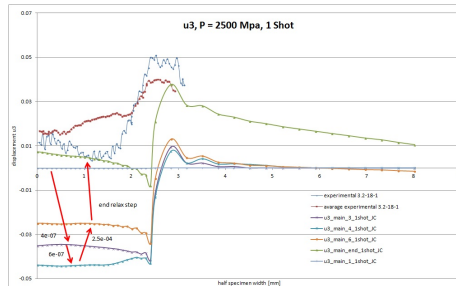


Figure 3.31: Displacement evolution on main specimen part

Picture ?? shows the comparison between the residual stress achieved on the main coupon part and the experimental results. While a smooth profile characterizes the experimental results, the numerical ones shows the typical central shot tensile residual stress. This behavior can be seen in all numerical simulations representative of a single central shot.

This parameter is referred to the internal energy of the process, which is an estimation of the free energy of a thermodynamic system, in the case of laser

3.5. JOHNSON-COOK MODEL IN BECHTOLD NUMERICAL SIMULATIONS

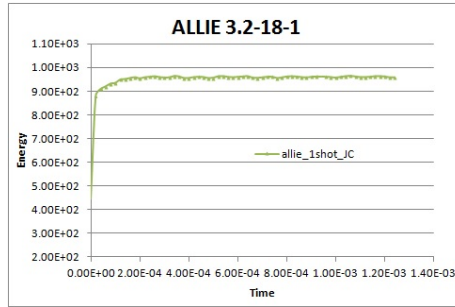


Figure 3.32: ALLIE energy

settings parameters 3.2-18-1, $p=2500$ Mpa. The parameter trend shows that the process, in the end, arrived at equilibrium, as expected.

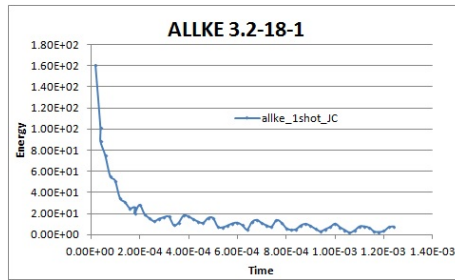


Figure 3.33: ALLKE energy

Picture ?? shows the kinetic energy evolution of the process. Being the kinetic energy the energy associated to a body because of its movement, this parameter gives indications about the achievement of an equilibrium condition in the end of the process.

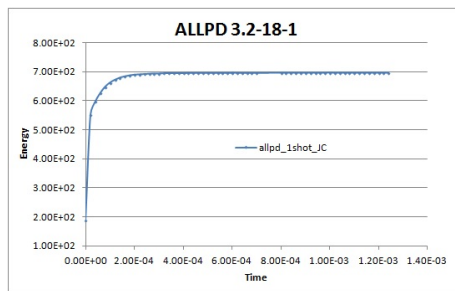


Figure 3.34: ALLPD

Picture ?? shows the plastic deformation energy trend. This parameter represents the energy dissipated by rate-independent and rate-dependent plastic deformation.

The pressure pulse definition serves to define the energies input from the laser to the target; the inserted energy is splitted into different parts, such as:

3.5. JOHNSON-COOK MODEL IN THE FINITE ELEMENT SIMULATIONS

- plastic deformation
- kinetic energy
- internal energy
- heating

The evaluation of the internal and kinetic energies make it possible to check if the dynamic stress state has become stable. Looking at the reported graphs of the internal and kinetic energies, tending respectively to a constant value and to zero, this means the shock waves interaction has become negligible, thus the dynamic stress state has become stable.

During the LSP process, external work goes in kinetic energy, internal energy, viscously dissipated energy, while the internal energy includes both the effects of elastically stored and plastically dissipated energies.

Of great importance is the time step increment choice. In the Abaqus implementation analyses the time step increment has to be choose in accordance to a stable time defined as:

$$\delta T_{stable} = \frac{L_e}{C_d} \quad (3.11)$$

where:

- L_e is the smallest element length
- C_d is the wave speed to the material

It has to be highlighted that, since laser shock peening process involves both an elastic and a plastic wave, but the elastic one is the faster, the latter has accounted for the time calculation. In order to avoid instabilities, the time increment must not exceed the sable time defined above; on the other hand, to have acceptable analyses times, the stable and interval times must be close to each other. The C_d parameter can be calculated as follows:

$$C_d^e = \sqrt{\frac{\lambda + 2\mu}{\rho}} \quad (3.12)$$

where:

$$\mu = G = \frac{E}{2(1 + \nu)} \quad (3.13)$$

and

$$\lambda = \frac{E\nu}{(1 + \nu)(1 - 2\nu)} \quad (3.14)$$

In order to have smaller computational times but reliable results, usually, a full symmetric model can be divided in more parts adding proper boundary conditions.

Nevertheless, some kind of analyses, like that used to predict the residual stress field to be then input as predefined field in the initial step of a subsequent analysis, involving xfem approach to describe for example the crack growth

3.5. JOHNSON-COOK MODEL IN THE FINITE ELEMENT SIMULATIONS

behavior, it is preferable to implement the full model, since this will result in a more accurate insertion of the crack, which, due to the needs of the xfem requirements, has not to coincide with a mesh element line. The choice of a proper element size has to be accurate, so to not incur in to excessively expensive analyses, in terms of computational costs, but to achieve reliable predictions.

Since laser shock peening involves high magnitude loading conditions, which can easily result in element distortion, first order elements have been adopted, since the second order ones are more suitable for standard analyses.

In the implemented models, the hourglass control formulation has been adopted because it provides a better accuracy of the coarser mesh associated with only a little amount of extra computational cost, but guarantees a better material non linear response at high strain levels, when compared with the default total stiffness formulation.

Johnson - Cook model, all explicit approach, has been used to implement some configuration and make prediction on the residual stress field achieved on different coupon thicknesses.

Specimen Dimension investigated are:

- 50*50*6 [mm]
- 50*50*8 [mm]
- 50*50*12.5 [mm]

Ablative layer thickness has been set at 0.1 mm. The shot dimension is 4*4 mm. Material properties are set as:

- Al 7050-T7451
 - Conductivity = 167
 - Density = 2.75e-09
 - Elastic = 70000, 0.33
 - Plastic Hardening, JC:

A [MPa]	B [MPa]	n	m	T_m	T_0
435	110	0.3	1.8	908	293

Table 3.4: JC parameters, Al 7050-T7451

- rate dependent, type=JC, 0.001, 1e06
- Specific Heat 8.5e+08
- Ablative, same parameters as that adopted for Al7050-T7451, except for:
 - Elastic 19000, 0.33
 - 1
 - Rate dependent 0.08, 1e06

Loading condition has been set as:

3.5. JOHNSON-COOK MODELING TECHNIQUE IN NUMERICAL SIMULATIONS

A [MPa]	B [MPa]	n	m	T_m	T_0
10	50	0.94	1.8	908	293

Table 3.5: JC parameters, Ablative

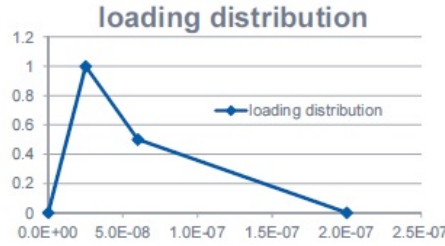


Figure 3.35: Loading Distribution

- Gaussian Pressure Curve Shape
- Triangular asymmetric configuration

Steps have been defined as follows:

- Initial, Back Specimen Side Encastre
- Load, Dynamic Explicit, direct user control: 4e-09, 5e-05; bulk viscosity: 0.06, 1.2 (default parameters)
- Unload, Dynamic Explicit: -, 0.0001; bulk viscosity: 0.06, 1.2 (default parameters)
- BCs, Free Shot surface, Encastre back surface; Dynamic Explicit: -, 0.0001
- Relax, Dynamic Explicit, Bulk Viscosity: 0.06, 1.2 (default parameters)

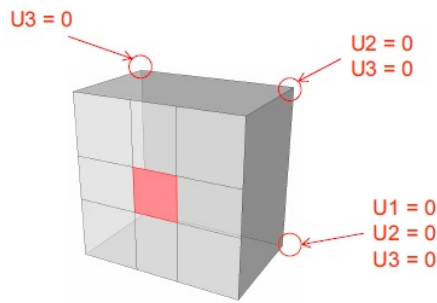


Figure 3.36: BCs Relax Step

Different laser power densities have been investigated, and their effect on the predicted residual stresses achieved has been compared.

Mesh has been set as:

3.5. JOHNSON-COOK MODELING TECHNIQUE IN NUMERICAL SIMULATIONS

- C3D8R element type
- finer mesh implemented in correspondence to the shot area to achieve more reliable results
- Coarser mesh far from the shot area to reduce the computational costs

The first investigated configuration is characterized by a double side peening, 3 layer as coverage, and the laser settings as reported in the following ??:

Power Density [GW/cm ²]	Pulse Duration [ns]	Number of Layers
2	18	3
3	18	3
4	18	3
5	18	3

Table 3.6: Investigated Configurations

The shooting configuration is ??:

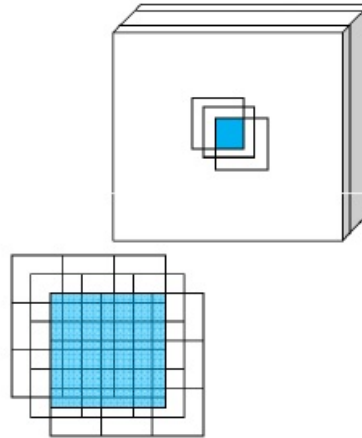


Figure 3.37: Shooting Configuration, 3 layers, geometry

The implemented shooting sequence is reported in the following picture ??:

The second investigated configuration is equal to the previous one, in terms of analyzed thicknesses and geometry parameters ??, but is characterized by 4 layers as coverage, and the shooting configuration is reported in the following ??:

The shooting sequence is reported in the following ??:

The last investigated configuration involves 5 layers as coverage. The laser setting are reported in ??:

The investigated geometry is shown in ??:

The shooting sequence is reported in ??:

The residual stress field achieved has been evaluated in all the directions shown in ??:

3.5. JOHNSON-COOK MODELING TECHNIQUE FOR NUMERICAL SIMULATIONS

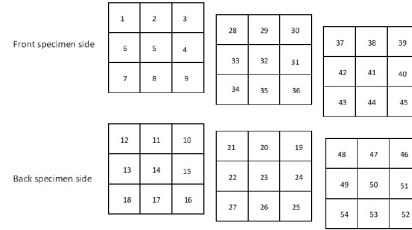


Figure 3.38: Shooting sequence, 3 layers as coverage

Power Density [GW/cm ²]	Pulse Duration [ns]	Number of Layers
2	18	4
3	18	4
4	18	4
5	18	4

Table 3.7: Investigated Configurations

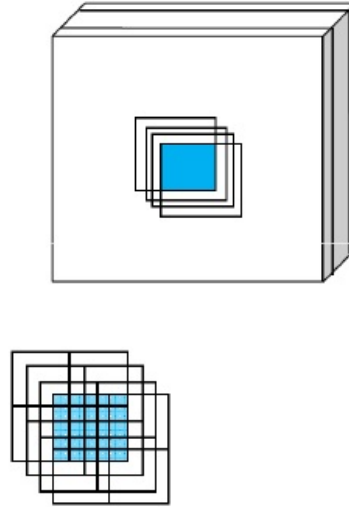


Figure 3.39: Shooting geometry, 4 layers coverage

Power Density [GW/cm ²]	Pulse Duration [ns]	Number of Layers
2	18	5
3	18	5
4	18	5
5	18	5

Table 3.8: Investigated Configurations

3.5. JOHNSON-COOK MODELING TECHNIQUE

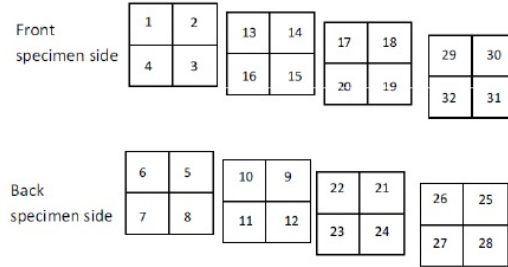


Figure 3.40: Shooting sequence, 4 layer coverage

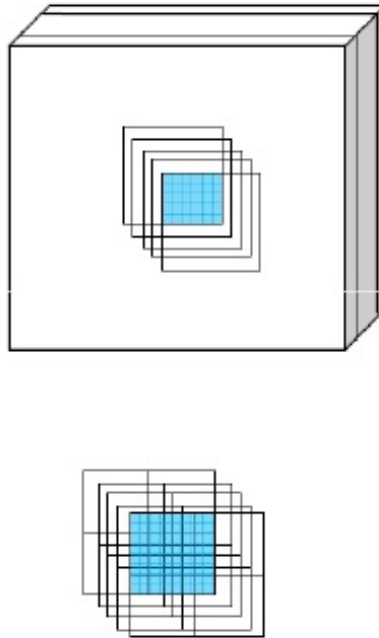


Figure 3.41: Shooting geometry, 5 layers as coverage

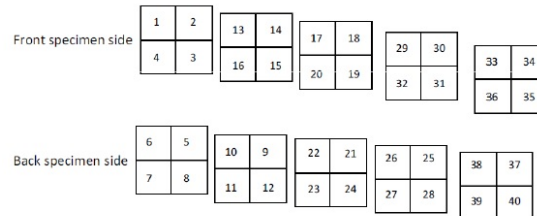


Figure 3.42: Shooting sequence, 5 layers coverage

3.5. JOHNSON-COOK MODELING TECHNIQUE IN NUMERICAL SIMULATIONS

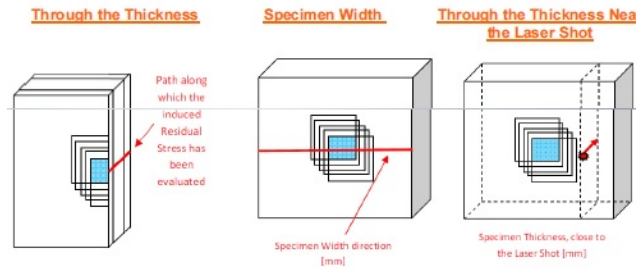


Figure 3.43: Residual stress measurement paths

Picture ?? shows the different residual stress values achieved for each of the investigated configurations characterized by 6 mm thickness:

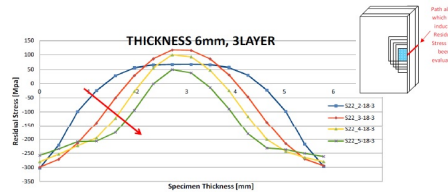


Figure 3.44: residual stress field achieved for different laser setting parameters on 6 mm coupon thickness

The arrow shows the direction in respect to which, the laser settings parameters give the deeper compressive residual stress field. As expected, increasing the laser power density, leaving the same number of layers, the compressive residual stress field achieved is deeper. Configuration 5 18 3 shows the higher compressive residual stresses, equal to -260 MPa, through the thickness up to a depth of 2.5 mm.

Picture ??:

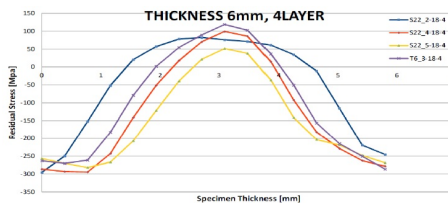


Figure 3.45: Residual Stress on 6 mm thick coupon, 4 layers coverage

The arrow shows the direction in respect of which, the laser settings parameters give the deeper compressive residual stress field. As expected, increasing the laser power density, leaving the same number of layers, the compressive residual stress field achieved is deeper. Configuration 5 18 4 shows the higher compressive residual stresses, equal to - 280 MPa, through the thickness up to a depth of 2.5 mm.

Picture ??:

3.5. JOHNSON-COOK MODELING TECHNIQUE

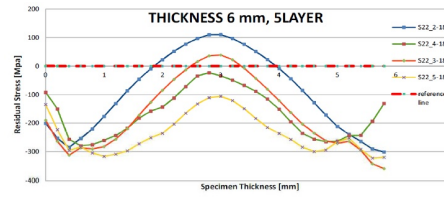


Figure 3.46: Residual Stress on 6 mm thick coupon, 5 layers coverage

The arrow shows the direction in respect of which, the laser settings parameters give the deeper compressive residual stress field. As expected, increasing the laser power density, leaving the same number of layers, the compressive residual stress field achieved is deeper. Configuration 4 18 5 shows a compressive residual stress through the all coupon thickness with a maximum value of - 280 MPa. Also configuration 5 18 5 shows a compressive residual stress through the all coupon thickness, but with a maximum value of - 320 MPa.

Picture ??:

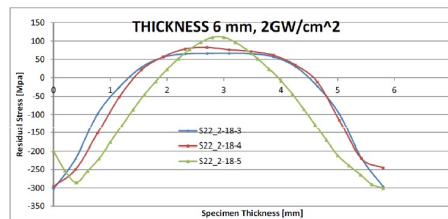


Figure 3.47: Residual stress on 6 mm thick coupon, 2 GW/cm²

As expected, increasing the number of layers, leaving the same laser power density, the compressive residual stress field achieved is deeper, on both specimen shoot sides. Same trend can be seen for all the tested laser power densities reported in ??, ?? and ??.

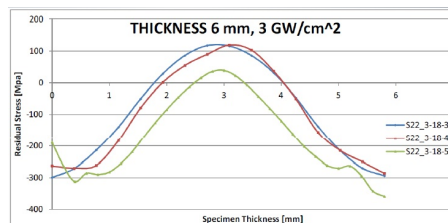


Figure 3.48: Residual stress on 6 mm thick coupon, 3GW/cm²

Picture ??:

Shows the through the thickness Tensile residual Stress Field, to balance the through the thickness compressive residual stress achieved in correspondence to the shot center area.

Picture ??:

Picture ??:

3.5. JOHNSON-COOK MODEL FOR BEAM-TO-BEAM LASER SIMULATIONS

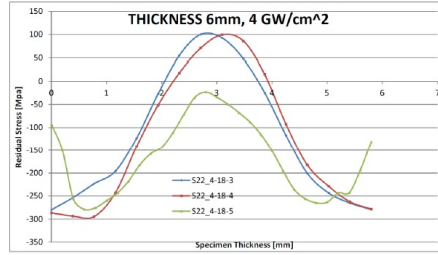


Figure 3.49: Residual stress on 6 mm thick coupon, 4GW/cm²

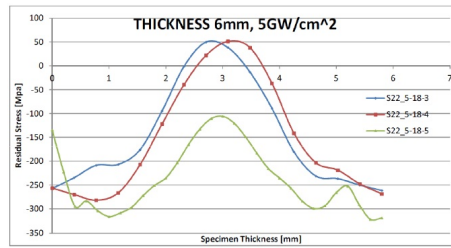


Figure 3.50: Residual stress on 6 mm thick coupon, 5GW/cm²

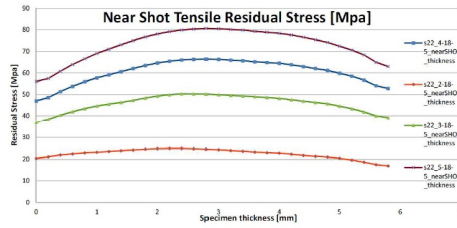


Figure 3.51: Residual stress field on 6 mm thick coupon aside the laser shot

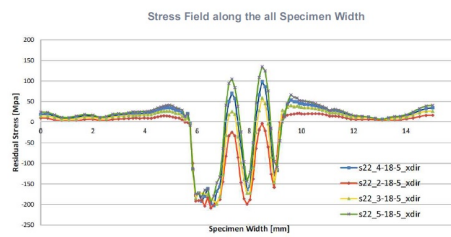


Figure 3.52: residual stress on 6 mm thick coupon, along specimen width

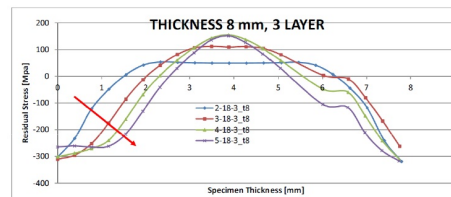


Figure 3.53: Residual stress on 8 mm thick coupon, 3 layers

3.5. JOHNSON-COOK MODELING TECHNIQUE

The arrow shows the direction in respect of which, the laser settings parameters give the bigger and deeper compressive residual stress field. The same in the following pictures, ??, ??. As expected, increasing the laser power density, leaving the same number of layers, the compressive residual stress field achieved is bigger and deeper. Configuration 5 18 5 shows a compressive residual stress through the thickness at 2.5 mm depth, with a maximum value of - 270 MPa.

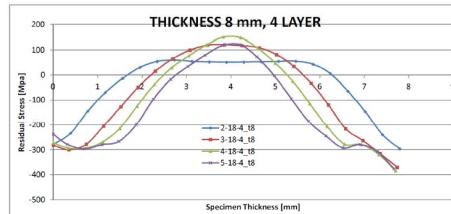


Figure 3.54: Residual stress on 8 mm thick coupon, 4 layers coverage

As expected, increasing the laser power density, leaving the same number of layers, the compressive residual stress field achieved is bigger and deeper, on both specimen shoot sides. Configuration 5 18 5 shows a compressive residual stress through the thickness at 2.8 mm depth, with a maximum value of - 300 MPa.

Picture ??:

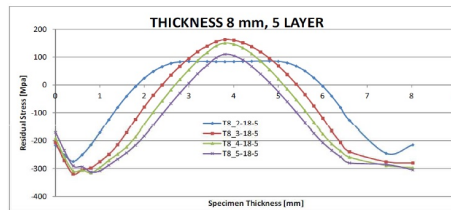


Figure 3.55: Residual stress on 8 mm thick coupon, 5 layers coverage

As expected, increasing the laser power density, leaving the same number of layers, the compressive residual stress field achieved is bigger and deeper, on both specimen shoot sides. Configuration 5 18 5 shows a compressive residual stress through the thickness at 3.0 mm depth, with a maximum value of - 310 MPa.

Picture ??:

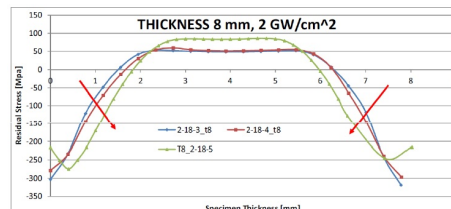


Figure 3.56: residual stress on 8 mm thick coupon, 2 GW/cm²

3.5. JOHNSON-COOK MODEL FOR BEAM-TO-BEAM LASER SIMULATIONS

As expected, increasing the number of layers, leaving the same laser power density, the compressive residual stress field achieved is bigger and deeper, on both specimen shoot sides. Same trend can be seen in the following pictures, each referring to a different laser power density but same coupon thickness, ??, ??, ??:

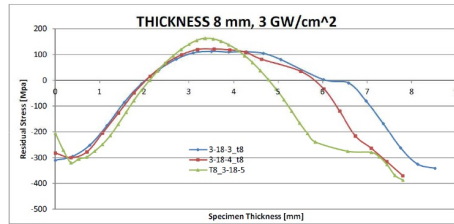


Figure 3.57: Residual stress on 8 mm thick coupon, 3 GW/cm^2

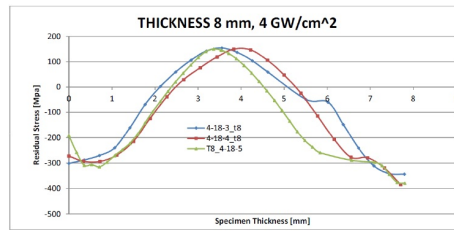


Figure 3.58: residual stress on 8 mm thick coupon, 4 GW/cm^2

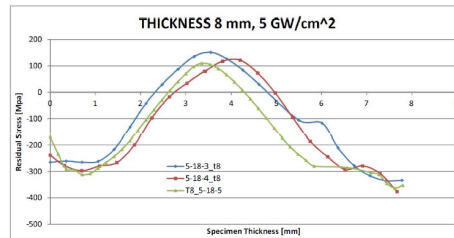


Figure 3.59: residual stress on 8 mm thick coupon, 5 GW/cm^2

The following results show the residual stress field achieved for coupon thicknesses of 12.5 mm.

Picture ??:

Shows that, as expected, increasing the laser power density, leaving the same number of layers, the compressive residual stress field achieved is bigger and deeper, on both specimen shoot sides. Configuration 5 18 5 shows a compressive residual stress through the thickness at 1.8 mm depth, with a maximum value of - 300 MPa.

Picture ??:

Shows that, as expected, increasing the laser power density, leaving the same number of layers, the compressive residual stress field achieved is bigger and deeper, on both specimen shoot sides. Configuration 5 18 5 shows a compressive

3.5. JOHNSON-COOK MODELING TECHNIQUE IN FINITE ELEMENT SIMULATIONS

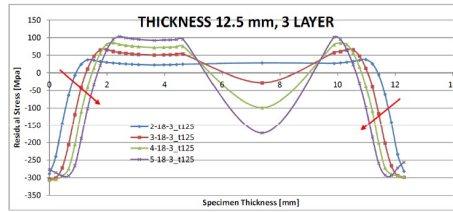


Figure 3.60: Residual stress on 12.5 mm thick coupon, 3 layers coverage

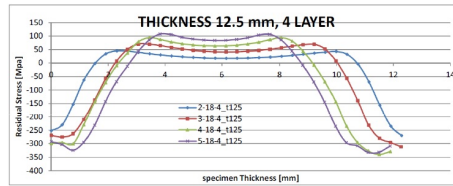


Figure 3.61: Residual stress on 12.5 mm thick coupon, 4 layers coverage

residual stress through the thickness at 2.5 mm depth, with a maximum value of - 320 MPa.

Picture ??:

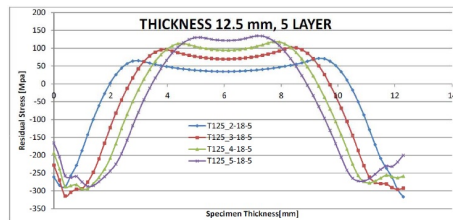


Figure 3.62: Residual stress on 12.5 mm thick coupon, 5 layers coverage

Shows that, as expected, increasing the laser power density, leaving the same number of layers, the compressive residual stress field achieved is bigger and deeper, on both specimen shoot sides. Configuration 5 18 5 shows a compressive residual stress through the thickness at 3.5 mm depth, with a maximum value of - 280 MPa.

Picture ??:

Shows that, as expected, increasing the number of layers, leaving the same laser power density, the compressive residual stress field achieved is bigger and deeper, on both specimen shoot sides. Same trend can be seen in the following ??, ??, ??:

A summary of the achieved results is reported in the following tables, each referring to a different coupon thickness, ??, ??, ??:

A summary of the configurations giving the best results in terms of higher compressive residual stress achieved at deeper depth is reported in the following table ??:

As can be seen from the results reported in the table ??, a compressive residual stress through the all specimen thickness can be reached only in the

3.5. JOHNSON-COOK MODELING TECHNIQUE FOR NUMERICAL SIMULATIONS

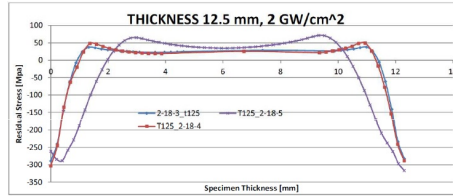


Figure 3.63: residual stress on 12.5 mm thick coupon, $2 \text{ GW}/\text{cm}^2$

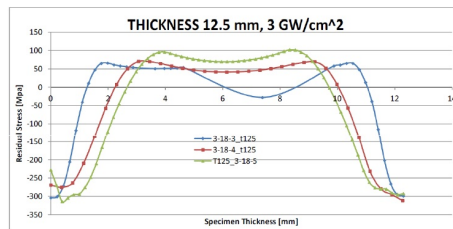


Figure 3.64: residual stress on 12.5 mm thick coupon, $3 \text{ GW}/\text{cm}^2$

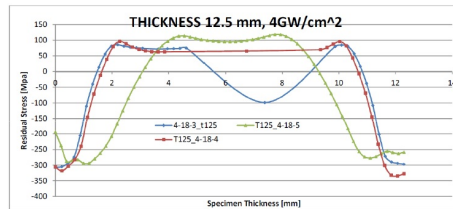


Figure 3.65: residual stress on 12.5 mm thick coupon, $4 \text{ GW}/\text{cm}^2$

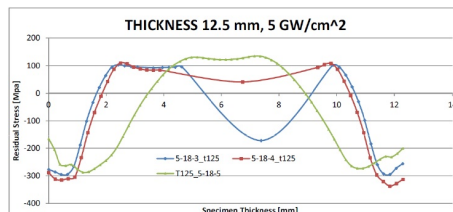


Figure 3.66: residual stress on 12.5 mm thick coupon, $5 \text{ GW}/\text{cm}^2$

3.5. JOHNSON-COOK MODELING TECHNIQUE FOR NUMERICAL SIMULATIONS

Thickness [mm]	Number of Layers, Coverage	Laser Power Density [GW/cm ²]	Compressive Residual Stress [MPa]	Depth [mm]
6	3	2	-300	1.6
6	3	3	-300	1.2
6	3	4	-280	2
6	3	5	-260	2.3
6	4	2	-300	1.2
6	4	3	-290	2
6	4	4	-270	2.1
6	4	5	-260	2.5
6	5	2	-290	1.8
6	5	3	-320	2.5
6	5	4	-290	all
6	5	5	-320	all

Table 3.9: Residual Stress field achieved on 6 mm thick coupon

Thickness [mm]	Number of Layers, Coverage	Laser Power Density [GW/cm ²]	Compressive Residual Stress [MPa]	Depth [mm]
8	3	2	-300	1.5
8	3	3	-310	2
8	3	4	-300	2.2
8	3	5	-270	2.5
8	4	2	-280	1.6
8	4	3	-300	2.1
8	4	4	-300	2.4
8	4	5	-300	2.8
8	5	2	-270	1.9
8	5	3	-320	2.2
8	5	4	-320	2.6
8	5	5	-320	3

Table 3.10: Residual Stress field achieved on 8 mm thick coupon

3.5. JOHNSON-COOK MODELING TECHNIQUE IN NUMERICAL SIMULATIONS

Thickness [mm]	Number of Layers, Coverage	Laser Power Density [GW/cm ²]	Compressive Residual Stress [MPa]	Depth [mm]
12.5	3	2	-280	1
12.5	3	3	-300	1.2
12.5	3	4	-300	1.5
12.5	3	5	-300	1.8
12.5	4	2	-250	1.8
12.5	4	3	-270	2.2
12.5	4	4	-300	2.2
12.5	4	5	-320	2.5
12.5	5	2	-280	2
12.5	5	3	-300	2.5
12.5	5	4	-320	3
12.5	5	5	-280	3.5

Table 3.11: Residual Stress field achieved on 12.5 mm thick coupon

Thickness [mm]	Number of Layers, Coverage	Laser Power Density [GW/cm ²]	Compressive Residual Stress [MPa]	Depth [mm]
6	5	4	-290	all
6	5	5	-320	all
8	5	5	-320	3
12.5	5	4	-320	3
12.5	5	5	-280	3.5

Table 3.12: Summary of the more compressive and deeper residual stresses achieved

analyses involving a 6 mm thick specimen, with laser set up parameters equal to 4-18-5 and 5185.

3.6 Eigenstrain Method

The term EIGENSTRAIN was first suggested by Mr. T. Mura in 1982 to indicate all the plastic (or permanent) strains that are automatically generated by materials when they are subjected to a mechanical treatment. The Eigenstrain method can be summarized in the following ??:

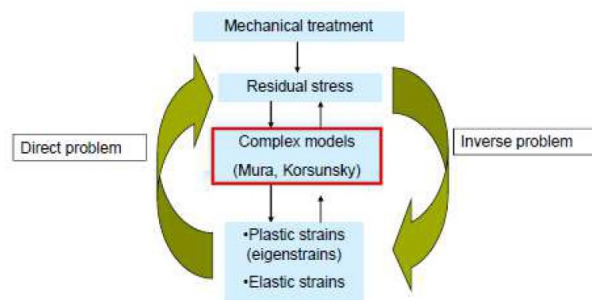


Figure 3.67: Eigenstrain Method

Eigenstrain account for all the permanent strains that arise in a material exhibiting inelastic behavior. The general procedure adopted in the implementation of the Eigenstrain method is ??:

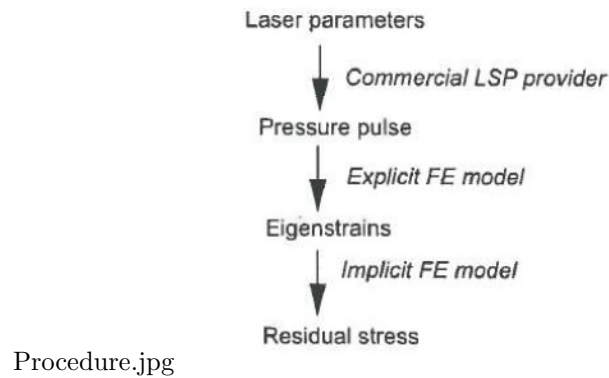


Figure 3.68: Eigenstrain procedure

Eigenstrain are so important because they depend only on:

- Material
- Laser Peening Parameters
- Peened Area

For thick wide Specimens Eigenstrain dont depend on:

- Coupon Geometry
- Coupon Thickness

Even if LSP involves both the shock induced thermal effects and the laser ablation induced heating, it is regarded to be an adiabatic process, because of its high velocity (ns); this way, it is possible to assume that the Eigenstrain are only due to plastic deformation.

the shock wave induces plastic strains that make the material stay in a geometric compatibility with the ligament; this gives rise to a residual stress field which satisfies both the deformation compatibility and the stress equilibrium. Therefore, independently on the complex dynamic responses of the material, the eigenstrains embedded in the model catch the residual stress field and deformations for different LSP processes just solving an elastic problem. Not catching the all dynamic of the process, the model is not suitable to predict the effects connected to the presence of edges or reflections of the shock waves from the boundaries. Cause of this disadvantage, the Eigenstrain method has several issues in predicting the residual stress field in thin parts, such as that representative of fuselage skin, that could feel the influence of edges and geometrical boundaries.

Because of its formulation, the method gives the possibility to develop a data collection for simple geometries to apply for more complex ones without doing any other expensive calculations (beyond the scope of this preliminary study on the numerical process implementation and validity).

The development of the Eigenstrain Model developed via an Abaqus subsequent application of a two Step Explicit Analysis involving the two faster step of the LSP process (initial + loading), followed by a two Step Standard Analysis, where the specimen material is described via the strain field obtained by the previous explicit analysis, fall into a wider numerical investigation whose goal is the implementation of a numerical LSP process prediction based on a first two step explicit and a second part Standard Analysis made of two steps having as inputs the results obtained from the explicit analysis as (Predefined Field, Initial Condition).

This way a two step explicit analysis was developed to obtain the strain components to insert as input in the subsequent standard analysis involving the Eigenstrain method. This approach will enable to obtain the same residual stress field and displacement status as that achieved with the validated all Explicit approach, but reduces the computational time costings

A major int to the Eigenstrain technique is provided in the following citation by Professor Hill and Dr. A.T. De Wald linear Eigenstrain Theory ??:

Considering the residual stresses introduced by an external process technology (such lamination, shot peening and so on), the material must necessary restore its internal balance when the application of the external treatment is finished.

Then the material itself will generate internal tensions to balance those forcefully introduced compressive stresses from an external source. So Hill indicates that the final residual stresses (or σ_{TOT}) can be seen as a superimposition of 2 stresses:

- One derived from an external source, σ_{LSP}

- One generated from the material in the attempt to balance this external one, $\sigma_{EQUILIBRIUM}$

$$\sigma_{TOT} = \sigma_{EQ} + \sigma_{LSP} \quad (3.15)$$

Derived from a small strain theory which states that:

$$\epsilon_{el} = \epsilon_{TOT} - \epsilon^* \quad (3.16)$$

The Eigenstrain Model has been implemented within this work of thesis by means of the Abaqus software by subsequent application of:

- Two Step Explicit Analysis for the description of the first fast part of the LSP process (Initial BCs + Loading) from which achieving the strain components. Analysis parameters maintained the same of the previous Analysis described:
 - Geometry
 - Material (Johnson-Cook Model)
 - Step Time Period
 - Loading Entity and Amplitude
 - Mesh
- Two Step Standard Analysis for the description of the second slower LSP process (Unloading and Relax):
 - Geometry
 - Relax Conditions and unit increment temperature as predefined field
 - Step Time Period
 - Mesh

The adopted geometry is the same of that used for the previous explicit analysis; this case a further partition has been created to fulfill the Eigenstrain procedure, leading to ??:

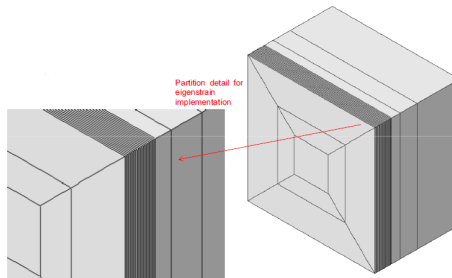


Figure 3.69: Partition adopted for Eigenstrain Method application

The parameters' set for the analysis are:

- Ablative Layer (simulated with Johnson-Cook Material Model):

- Aluminum Zero
- Conductivity = 167
- Density = 2.75e-09
- Elastic, Type isotropic, Young Modulus = 19000, Poisson Ratio = 0.33
- Plastic, hardening = isotropic, Yield Stress = 10, Plastic Strain = 0
- Rate Dependent, Johnson - Cook
- $C=1e-06$, $\epsilon_0=1000000$
- Main Specimen Body:
 - Al 7050-T7451
 - Density 2.75 e-09
 - Elastic, type = Isotropic, Youngs Modulus = 70000, Poissons Ratio = 0.33
- Step Definition:
 - Initial: Encastre BCs on the back Side of the specimen
 - Load: Field Output Reques = Frequency, evenly spaced time intervals = 10, History output Request = Frequency, evenly spaced time intervals = 200
 - Load Definition
 - Pressure
 - Load, Dynamic Explicit, applied only in the central shot area
 - Distribution uniform
 - Magnitude 1800 [MPa]
 - Amplitude, ??:

Time Frequency	Amplitude
0	0
3e-08	1
4e-07	0

Table 3.13: Amplitude Definition

- End of the Explicit Analysis

Applying the above mentioned procedure, it was possible to obtain the strain components to be used as input data in the description of the Material in the development of the Eigenstrain two Steps Standard Analysis, ??:

The parameters used for the Standard Analysis part of the Eigenstrain Approach are reported below:

- Main Specimen Body:

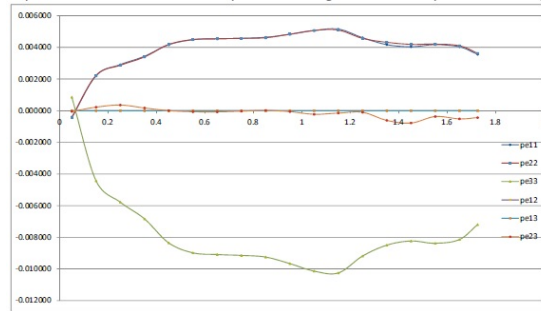


Figure 3.70: Strain Components achieved via Explicit Analysis to be used as input in subsequent Standard Analysis

- Al 7050-T7451
- Elastic, type = Isotropic, Youngs Modulus = 70000, Poissons Ratio = 0.33
- Ablative Layer
 - Introduced using the Eigenstrain partition, in the definition of the material first layer (the one closer to the surface), in the two steps Standard Analysis
- Eigenstrain partition (in each partition layer defined as in the picture reported before ??, the material for the Standard Analysis is described as):
 - Elastic, type = Isotropic, Youngs Modulus = 70000, Poissons Ratio = 0.33
 - Mechanical, Expansion, Type = Anisotropic, six thermal expansion coefficient:

alpha11	alpha22	alpha33	alpha12	alpha13	alpha23

using the strain data reported in the previous slide with the correspondent eigenstrain partition layer

This can be done because, if a unit temperature increment is considered, the strain relation can be written as:

$$\epsilon = \alpha \Delta T \quad (3.17)$$

As long as $\Delta T=1$:

$$\epsilon = \alpha \quad (3.18)$$

An example of the listed values to be used as input in the Eigenstrain Analysis is reported in ??:

- Material:
 - Conductivity = 167

Values to introduce in eigen standard						
thickness	pe11	pe22	pe33	pe12	pe13	pe23
0.049999	-0.000449	-0.000406	0.000855	-1.58E-008	7.38E-008	-4.79E-005
0.15	0.002198	0.002227	-0.004424	1.05E-007	-8.19E-007	0.000223
0.25	0.002811	0.002888	-0.005780	4.86E-007	9.02E-007	0.000356
0.349999	0.003437	0.003395	-0.006832	1.26E-008	1.20E-008	0.000172
0.45	0.004169	0.004183	-0.008352	-1.17E-007	2.60E-007	7.81E-006
0.549999	0.004485	0.004495	-0.008980	9.69E-008	3.95E-007	-6.70E-005
0.65	0.004544	0.004544	-0.009088	7.56E-008	-3.90E-008	-7.32E-005
0.75	0.004574	0.004570	-0.009144	-1.98E-008	1.15E-007	-2.53E-005
0.849999	0.004639	0.004609	-0.009249	-4.39E-008	-2.34E-007	1.99E-005
0.95	0.004623	0.004636	-0.009660	4.42E-008	1.37E-007	-5.68E-005
1.05	0.005084	0.005070	-0.010134	1.32E-008	-4.94E-008	-0.000225
1.15	0.005156	0.005093	-0.010249	-1.07E-007	-3.45E-007	-0.000150
1.25	0.004614	0.004569	-0.009183	-6.13E-007	1.88E-007	-0.000100
1.35	0.004174	0.004321	-0.008466	-4.56E-008	5.83E-007	-0.000609
1.45	0.004041	0.004192	-0.008233	-9.45E-008	2.26E-007	-0.000775
1.55	0.004172	0.004206	-0.008377	7.56E-008	9.50E-008	-0.000368
1.65	0.004038	0.004101	-0.008140	1.34E-007	1.31E-007	-0.000514
1.725	0.003561	0.003632	-0.007193	-1.29E-007	7.79E-007	-0.000435

Figure 3.71: Example of strain values to be used as input in the Standard Analysis, each attributed to the proper partition level

- Specific heat = 850000000
- density = 2.75 e-09

The achieved residual stress is reported in ??:

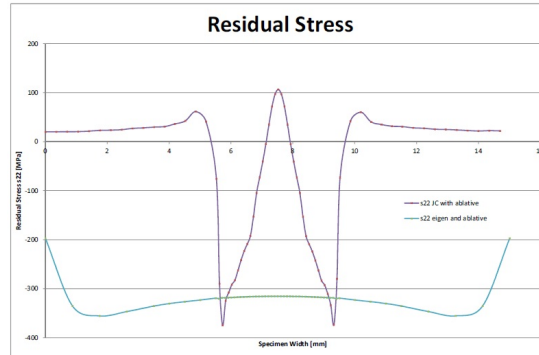


Figure 3.72: Residual Stress comparison between JC with Ablative Layer and Eigenstrain approach

From ??, the Eigenstrain trend does not present the central peak in the residual stress profile, which was always present in the residual stress field predicted via Johnson Cook Material Model.

The displacement achieved are reported in ??:

An analysis on the ablative layer role in term of temperature effect has been carried out also when applying the Eigenstrain Approach; in this case, as well as for JC, the main temperature difference between the configurations with and without the ablative layer, is highlighted at the coupon surface. Nevertheless the gap can be quantified in 1 kelvin, thus the Ablative Layer effect in terms of accuracy in the achieved data has to be related to some other effect, but not to the temperature one. The temperature gradient through the coupon thickness is reported in ??:



Figure 3.73: Displacement Eigenstrain vs Experimental

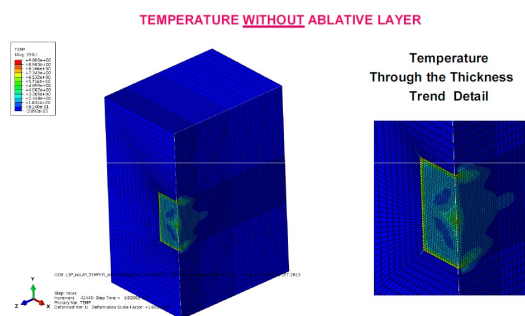


Figure 3.74: Temperature Profile Eigenstrain Analysis

3.7 Kinematic Hardening

The kinematic hardening models are used to simulate the inelastic behavior of materials that are subjected to cyclic loading; this models can be implemented in the Abaqus software with one or multiple back-stresses. The elastic part of response must be simulated by use of the linear elasticity material model.

Within the Kinematic hardening approach, the yielding of the metals is independent of the equivalent pressure stress. These models are suited for most metals subjected to cyclic loading conditions. The pressure-independent yield surface is described by the function ??:

$$F = f(\sigma - \alpha) - \sigma_0 = 0 \quad (3.19)$$

where:

- σ_0 is the yield stress
- $f(\sigma - \alpha)$ is the equivalent Mises stress with respect to the back-stresses

For example, the equivalent Mises stress is defined as:

$$(3.20)$$

where:

- S is the deviatoric stress tensor, defined as $S = \sigma + pI$
 - σ is the stress tensor
 - p is the equivalent pressure stress
 - I is the identity tensor
- α is the deviatoric part of the back-stress tensor

The kinematic hardening model is based on a plastic flow which can be represented as follows:

$$\dot{\epsilon}^{pl} = \bar{\epsilon}^{pl} \frac{\partial F}{\partial \sigma} \quad (3.21)$$

where:

- $\dot{\epsilon}^{pl}$ is the rate of plastic flow
- $\bar{\epsilon}^{pl}$ is the equivalent plastic strain rate

The evolution of the equivalent plastic strain is obtained from the equivalent plastic work expression, as:

$$\sigma^0 \bar{\epsilon}^{pl} = \sigma : \dot{\epsilon}^{pl} \quad (3.22)$$

which yields $\bar{\epsilon}^{pl} = \sqrt{\frac{2}{3} \dot{\epsilon}^{pl} : \dot{\epsilon}^{pl}}$ for isotropic Mises plasticity. The assumption of associated plastic flow is acceptable for metals subjected to cyclic loading as long as microscopic details such as localization of plastic flow occur, which lead the component to fatigue failure, are not of interest.

Two main kinematic hardening models can be defined as follows:

- linear kinematic hardening, characterized by a constant hardening modulus
- non linear kinematic and non linear isotropic hardening models

The linear kinematic hardening model describes the translation of the yield surface in stress space by means of the back-stress α_i . If temperature effects can be neglected, the hardening evolution can be described by the Ziegler law:

$$\dot{\alpha} = C \frac{1}{\sigma_0} (\sigma - \alpha) \bar{\epsilon}^{pl} \quad (3.23)$$

where:

- $\bar{\epsilon}^{pl}$ is the equivalent plastic strain rate
- C is the kinematic hardening modulus
- σ^0 is the equivalent stress defining the size of the yield surface, which in this model remains constant and equal to $\sigma|_0$
- $\sigma|_0$ is the size of the yield surface at zero plastic strain

The non linear kinematic hardening component describes the translation of the yield surface in stress space by means of the back-stress α . The isotropic hardening component describes the change of the equivalent stress defining the size of the yield surface σ^0 , as a function of plastic deformation. In many cases several kinematic hardening components, known as back-stresses can be superimposed; they can lead to a result improvement, as will be reported in the following prediction on laser peening treatment. When the temperature and field variable dependencies are omitted, the hardening law for back-stresses becomes:

$$\dot{\alpha}_k = C_k \frac{1}{\sigma_0} (\sigma - \alpha) \bar{\epsilon}^{pl} - \gamma_k \alpha_k \bar{\epsilon}^{pl} \quad (3.24)$$

where the overall back-stress can be defined as:

$$\alpha = \sum_{k=1}^N \alpha_k \quad (3.25)$$

where:

- N is the number of back-stresses
- C_k is a material parameter that must be calibrated from each cyclic test data, and represents the initial kinematic hardening moduli
- γ_k is a material parameter that must be calibrated from each cyclic test data, and determines the rate at which the kinematic hardening moduli decrease with increasing plastic deformation

When C_k and γ_k are zero, the model reduces to an isotropic hardening one. Picture ??:

shows an example of a non linear kinematic hardening model with three back-stresses, similar to the one used to implement the laser peening process and reported in the following results.

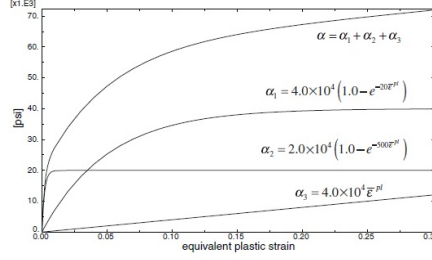


Figure 3.75: kinematic hardening model with three back-stresses

The isotropic hardening behavior of the model defines the evolution of the yield surface size σ^0 as a function of the plastic strain $\bar{\epsilon}^{pl}$. This can be introduced by specifying σ^0 and $\bar{\epsilon}^{pl}$ in a tabular form or by using the following exponential law:

$$\sigma^0 = \sigma|_0 + Q_\infty(1 - e^{-b\bar{\epsilon}^{pl}}) \quad (3.26)$$

where:

- $\sigma|_0$ is the yield stress at zero plastic strain
- Q_∞ is a material parameter which represents the maximum change in size of the yield surface
- b is a material parameter which defines the rate at which the size of the yield surface changes at the plastic strain development

In cyclic hardening of metals some effects have to be taken into account, such as:

- Bauschinger effect, which is characterized by a reduced yield stress after load reversal following the occurred plastic deformation due to the initial loading. Bauschinger effect decreases after continuous cycling. The linear kinematic hardening component takes into account this phenomenon whereas the nonlinear one improves the cycles' shape. The shape of the cycle can be improved applying a non-linear model and multiple back-stresses.
- Cycling hardening with plastic shakedown; this effect describes the hardening of soft metals toward the stable limit, whereas the initially hardened materials tend to soften, as in ??:

The kinematic hardening component alone, predicts the shakedown after one stress cycle whereas the combination of the isotropic component plus the non-linear kinematic one, predicts the shakedown after several cycles.

Even if the non-linear isotropic/kinematic hardening model provides more accurate results in cyclic loading conditions, it still has some limitations, such as the isotropic hardening is the same at all strain ranges. The amount of isotropic hardening depends on strain range. Furthermore, the model is a rough approximation of the cyclic behavior since if two different strain ranges are applied,

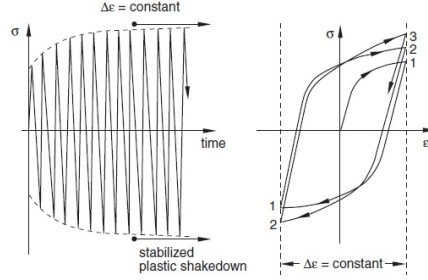


Figure 3.76: cyclic hardening with plastic shakedown

one following the other, the deformation in the first cycle affects the isotropic hardening of the second one.

When using a linear kinematic model approximates the hardening behavior with a constant hardening. A stabilized cycle is obtained after cycling over a fixed strain range until a steady state situation is reached; this way the stress-strain curve is the same at each cycle.

Providing the above-mentioned parameters, the linear kinematic hardening modulus can be express as:

$$C = \frac{\sigma - \sigma|_0}{\epsilon^{pl}} \quad (3.27)$$

The isotropic hardening component of the model can be expressed as the evolution of the equivalent stress as a function of the size of the yield surface, σ^0 and of the equivalent plastic strain $\bar{\epsilon}^{pl}$. The material parameters C_k and γ_k define the kinematic hardening component.

The kinematic hardening model for material definition can be implemented in the Abaqus software by using the following procedure:

- Mechanical
- Plasticity
- Plastic: Hardening: Combined
- Data type: Parameters
- Number of back-stresses: n

Numerical simulation of the LSP process has been implemented also via the kinematic hardening approach, both using one and three back-stresses. The achieved results have then be compared with that coming from the Johnson-Cook all explicit approach with ablative layer simulation. The same analysis approach has been used to implement numerical models referring to different shot configurations and coupon thicknesses. The reported results have been achieved for a coupon showing the following characteristics:

- 50*50*12.5 [mm]
- Al 7050-T7451

- Two side peening
- 4*4 [mm] as spot size
- laser configuration: 4-18-4

The kinematic hardening parameters used for the implementation of the numerical model involving respectively one and three back-stresses are reported in the following tables ??, ??, ??:

Plastic				Cyclic Hardening		
Yield Stress at zero plastic strain [MPa]	Kinematic Hardening Parameter C_1 [MPa]	γ_1		Equivalent Stress [MPa]	Q_∞ [MPa]	b
457	3211.7	25		457	-20	4

Table 3.14: KH parameters, Al 7050-T7451, 1 back-stress

Plastic						
Yield Stress at zero plastic strain [MPa]	Kinematic Hardening Parameter C_1 [MPa]	γ_1	Kinematic Hardening Parameter C_2 [MPa]	γ_2	Kinematic Hardening Parameter C_3 [MPa]	γ_3
390	38973.5695	275.524195	195909.859	3134.56109	3298.12915	23.4359252

Table 3.15: KH parameters, Al 7050-T7451, 3 back-stress, plastic

Cyclic Hardening			
Equivalent Stress [MPa]	Q_∞ [MPa]	b	
390	-145.703734	239.439252	

Table 3.16: KH parameters, Al 7050-T7451, 3 back-stress, cyclic hardening

Picture ??:

shows the difference in the numerical results achieved for the residual stress parameter along the coupon width. All the results are close to each other even if that linked to the KH 1 BS and JC are closer; slightly different from the previous two is the result achieved for the KH 3 BS model implemented. A comparison with experimental results is requested to check the reliability of the three procedure.

Picture ?? shows the through the thickness residual stresses achieved via the KH 1 and 3 back-stresses and JC with ablative layer implementation. Same conclusion as before can be made for the residual stress distribution through the coupon thickness, with the KH 3 BS approach being slightly different from the other two techniques.

Picture ?? shows the displacement parameter achieved for all the three different modeling techniques adopted. This case, KH 1 BS and 3 BS give the closer results while the Johnson-Cook model shows slightly different values, even if the trend is confirmed for the all three modeling techniques.

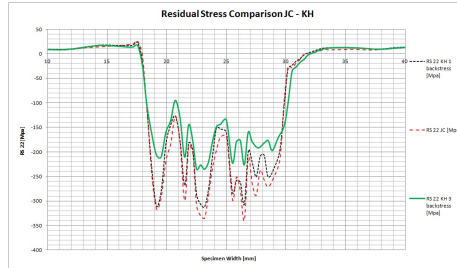


Figure 3.77: Residual Stress comparison between JC and KH approach

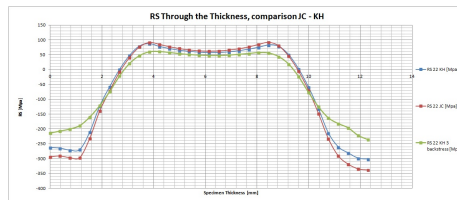


Figure 3.78: Through the thickness residual stress comparison between JC and KH approach

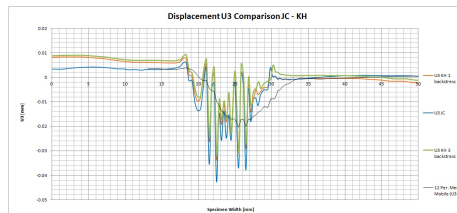


Figure 3.79: Displacement parameter, comparison between the KH and JC approach

3.8 Conclusions

The tensile peak which can be seen in the shot center when implementing the model referring to a single laser shot, can be due to the strength of the reflected wave, which can be higher in respect to the compressive incoming one, thereby resulting in a tensile peak.

A parametric study implemented on the Johnson -Cook parameters at Witwatersrand University shows the influence of the various involved parameters describing the material behavior on the achieved results in terms of residual stress field achieved:

- an increase in B and n parameters result in a shift upwards of the displacement curve
- an increase in A and a decrease in n, both result in a flattening of the displacement curve

The difference found in the residual stress profile with the same variations of A, B and n parameters is less pronounced than that found for the displacement parameter. An increase in the C value, results in a decrease in absolute value of the displacement parameter, and both in an inversion of the curve representative of that parameter. An increase in ϵ_0 results in a tensile peak at the center of the shot, while an increase in the C value, results in a flattening of the same residual stress profile curve.

Multiple shot configuration leads to a residual stress profile without the central tensile peak, and to a smoother displacement curve description. Nevertheless, too much overlap can result in a material saturation with no further improvement in the compressive residual stress profile achieved.

The major issue of Johnson-Cook modeling technique is the restore of equilibrium linked to the shock wave phenomena. In order to have a numerical model reliable and time effective, the laser shots must happen at frequencies definitely higher than the real ones. Since the time interval in Johnson-Cook model has been set at $2e^{-05}$, being:

$$F = \frac{1}{2e^{-05}} = 50000 \quad (3.28)$$

where F is the numerical shot frequency. The achieved numerical value is five order of magnitude higher than the real laser peening process frequency, which is usually 2 Hz. Setting so high numerical frequencies is necessary to have time effective numerical simulations.

To avoid phenomena arising from this high set value of frequency, one of the intermediate study step which led to the final numerical model has been characterized by the presence of a so called ablative layer to compensate to the effects induced by setting higher values of linear and quadratic bulk viscosity parameters.

An other aspect to be taken into account is that the pressure magnitude corresponding to the adopted laser power has been defined based on the ??, which represents the pressure profile as Gaussian. Experimental measurements conducted at Witwatersrand University proved that this is no longer true for any kind of laser, thus for i.e. the SA laser system provides a top-hat non linear shape.

From the residual stress profile achieved with the kinematic hardening approach through the coupon width, it is possible to see in the lot of the analyzed cases a peak arising at the end of the compressive part; this is representative of the encounter phenomenon between the new incoming wave with the release one. This behavior can be associated to the chosen numerical frequency providing time effective analyses.

A comparison between the Johnson-Cook model and the kinematic hardening approach has been performed. Johnson-Cook material parameters are provided by split Hopkinson bar test which goes up to strain rate to 10^4 sec^{-1} which corresponds to the same value Abaqus is able to provide reliable results; nevertheless the laser peening process goes up to 10^6 sec^{-1} strain rate. Even if nor Johnson-Cook model neither the kinematic hardening approach are representative of the physics of the laser process, the Kinematic Hardening representation seems to be the best compromise to make predictions on the residual stress field achieved by laser shock peening process.

Bibliography

- [1] Brasted, Brockman. *Finite element simulation of laser shock peening, international journal of fatigue*, vol.21, no.7, 1999, pp. 719-724.
- [2] Ding et Ye. *Three-dimensional dynamic finite element Analysis of multiple laser shock peening process*, Surface Engineering, Vol.19, No.5, 2003, pp.351-358.
- [3] Wu, Shin. *From incident laser pulse to residual stress: a complete and self-closed model for laser shock peening*, ASME Journal of manufacturing science and engineering, Vol.129, No.1, 2007, pp.117-125.
- [4] Peyre, Caieb, Braham. *FEM calculation of residual stresses induced by laser shock processing in stainless steel implemented simulation based on Abaqus Explicit to model the shock propagation and attenuation, and on Abaqus Standard to predict the thermo-mechanical residual stresses*
- [5] Warren, Guo, Chen. *Massive parallel laser shock peening: simulation, analysis, and validation*, International Journal of Fatigue, Vol.30, No. 1, 2008, pp.188-197.
- [6] D.Glaser, R.Bedekar, and C.Polese. *Generation of secondary shock by cavitation in the LSP process*, IV International Conference on Laser Shock peening and Related Phenomena, Madrid 5-10 May, 2013.
- [7] C.Crudo. *Investigation on Laser Peening Capability by FE simulation*, Msater Thesis, University of Bologna, 2013.
- [8] W. Braisted, R. Brockman. *Finite element simulation of laser shock peening*, International Journal of Fatigue 21 (1999) 719-724.
- [9] Dassault Sistmes. *Explicit Dynamic analysis*, Abaqus Theory Manual. (2011)
- [10] Dassault Sistmes. *Implicit Dynamic analysis*, Abaqus Theory Manual. (2011)
- [11] Coratella Stefano. *Linear Eigenstrain Theory: Calibration of both simple and complex geometry FE Models*.

- [12] J.L.Ocana, M.Morales, C.Molpeceres, J.Torres. *Numerical simulation of surface deformation and residual stresses fields in laser shock processing experiments*, Appl. Surf. Sci. 238(2004), 242-248.
- [13] G.Ivetic. *Finite Element Analysis of Laser Shock Peening of Aluminum Alloy 7050-T7451 Thick Plates*, (2009). Alma Mater Studiorum University of Bologna.
- [14] M.Sticchi. *Finite element modelling of Laser Shock peening-Geometrical Constraints Impact on Residual Stress Distribution After Laser Shock Peening* (2011). University of Naples "Federico II".
- [15] Dassault Sistmes. *Explicit Dynamic Analysis* (2011). Abaqus/CAE User's Manual. Vol. II 6.3.3
- [16] Liu Zhanqiang, Shi Zhenyu and Guo Yuebin. *Fem simulation of minimum uncut Chip Thickness in Mechanical Microcutting* (2011). (2006) ISNMN 2010 Guilin and Han et al.
- [17] L. Berthe, R. Fabbro, P. Peyre, L. Toller, and E. Bartnicki. *Shock waves from a water-confined laser-generated plasma* (1997). J. Appl. Phys. 82, 2826 (1997).
- [18] Dassault Sistmes. *Cyclic loading of metals* (2011). Abaqus/CAE User's Manual. Vol. III 22.2.2
- [19] Peyre, Sollier, Chaieb, Berthe, Braham, Fabbro. *FEM simulation of residual stress induced by laser shock peening* (2003).
- [20] Ding, Ye. *Three dimensional finite element analysis of multiple laser shock peening process*, Surface engineering, vol 19, no 5, pp 351-358, 2003.
- [21] Ocana, Molpeceres, Morales, Torres. *Numerical Simulation of surface deformation and residual stress fields in laser shock processing experiments*, journal of applied surface science, vol 238, pp 242-248, 2004.
- [22] Wu, Shin. *A self close thermal model for laser shock peening under the water confinement regime configuration and comparison to experiments*, journal of applied physics, vol 97, no 11, pp 113517, 2005.
- [23] Wu, Shin. *From incident laser pulse to residual stress: a complete and self close model for laser shock peening*, asme journal of manufacturing science and engineering, vol 129, pp 117-125, 2007.
- [24] Warren, Guo, Chen. *Massive parallel laser shock peening: simulation analysis and validation*, international journal of fatigue, vol 30, no 1, pag 188-197, 2008.
- [25] Achintha, Nowell. *Eigenstrain modeling of residual stresses generated by laser shock peening*, journal of material processing technology, vol 21, pp 1091-1101.

CHAPTER 4

Afgrow Fatigue Life prediction

4.1 Afgrow Software

The commercial software Afgrow can be used to implement fatigue life predictions in components representative of fuselages skin subjected to spectral loading condition. Afgrow is based on a standard user interface to create an intuitive environment for fracture mechanic analyses, on the principles of which are based the concepts for the stress intensity factor calculation.

4.2 Geometry of the analyzed configurations

Two coupons geometries have been investigated, ??:

Parameter	Specimen A	Specimen B
Coupon Width [mm]	160	400
Coupon Length [mm]	400	800
Coupon Thickness [mm]	2	2

Table 4.1: Geometry configurations investigated via Afgrow Software

Within Afgrow it is possible to calculate the SIF by means of two different approaches, that are:

- Standard Stress Intensity Solution
- Weight Function Stress intensity solutions

The investigated crack configuration is based on a classical model geometry as reported in ??:

The SIF calculation is based on the following formulation of β geometric factor:

4.3. IMPLEMENTED LOADING CONDITION FOR FATIGUE LIFE PREDICTION

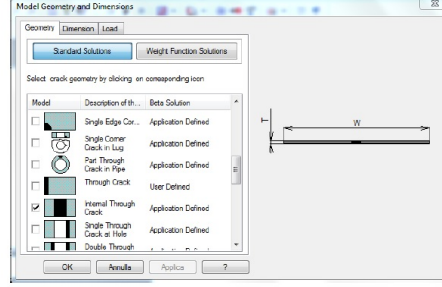


Figure 4.1: Afgrow Standard crack Solutions: Internal Through crack

$$K = \sigma \sqrt{\pi a} \left(1 - 0.025 \left(\frac{2a}{W} \right)^2 + 0.06 \left(\frac{2a}{W} \right)^4 \right) \sqrt{\sec\left(\frac{\pi a}{W}\right)} \quad (4.1)$$

the above mentioned solution for the β factor being valid for $0 < \frac{a}{W} \leq 0.5$.

4.3 Implemented loading condition

Afgrow allows the user to create a loading spectrum representative of the cyclic loading condition which is representative of that of a fuselage one. Spectra are cycle counted, thus each max- min pair describes a complete cycle. In the case of interest a constant amplitude loading characterized by a SMF of 70 MPa and a loading ratio R of 0.1 has been adopted.

4.4 Material description

The specimen material is Al 2024-T351. This material has been introduced in Afgrow by a tabular look up approach. When using a tabular look-up configuration, the user is allowed to input crack growth rate curves. The tabular look-up configuration is based on Walker equation on a point by point basis to extrapolate/interpolate data for two adjacent R values. The walker equation being expressed as:

$$\frac{da}{dN} = C[\Delta K(1 - R)^{m-1}]^n \quad (4.2)$$

Since a constant amplitude loading condition has been implemented, a single R value has been introduced. The tabular look-up table for the description of the adopted material needs to be filled in with other parameters, such as:

- ultimate strength
- Young Modulus
- Poisson Ratio

The filled tabular look-up table for the material of interest is reported in the following ??:

4.4. MATERIAL DESCRIPTION AFGROW FATIGUE LIFE PREDICTION

Input values of Delta_K for up to 30 da/dN values and up to 10 different R(stress ratio) values. Matrix must have at least two R values and two da/dN values.
Input: Delta_K for R >= 0; input Kmax for R < 0.0

Number of da/dN Sets: 30 Number of R Sets: 1

	R [1]
da/dN [1]	4.02e-006
da/dN [2]	4.88e-006
da/dN [3]	5.91e-006
da/dN [4]	7.17e-006
da/dN [5]	8.70e-006
da/dN [6]	1.07e-005
da/dN [7]	1.31e-005
da/dN [8]	1.61e-005
da/dN [9]	1.98e-005
da/dN [10]	2.47e-005
da/dN [11]	3.04e-005
da/dN [12]	3.75e-005
da/dN [13]	4.57e-005
da/dN [14]	5.56e-005
da/dN [15]	6.71e-005
da/dN [16]	8.04e-005
da/dN [17]	9.59e-005
da/dN [18]	0.000114
da/dN [19]	0.000138
da/dN [20]	0.000167
da/dN [21]	0.000201
da/dN [22]	0.000241
da/dN [23]	0.000288
da/dN [24]	0.000343
da/dN [25]	0.000408
da/dN [26]	0.000484
da/dN [27]	0.000574
da/dN [28]	0.000681
da/dN [29]	0.000808
da/dN [30]	0.000958

Material name: Aluminum Alloy

Ultimate Strength: 420 Young's Modulus: 10225.2

Coefficient of Thermal Expansion: 1.23e-005 Poisson's Ratio: 0.33

Upper limit on da/dN, DADNHI: 0.0019 Lower limit on da/dN, DADNLO: 3.93701

Plane Stress Fracture Toughness, KIC: 91.005 Yield Strength, YLD: 44.9617

Plane Strain Fracture Toughness, KIC: 33.672 Lower limit on R shift (Max: 0): -0.33

Delta K threshold value @R=0: 2.275 Upper limit on R shift (0, 1): 0.72

OK Cancel Save Read Apply

Figure 4.2: tabular look-up data for Al 2024-T351

The crack growth rate curves have been extrapolated from experimental results; this because to have a good agreement with the experimental results and that given by the Afgrow, it is necessary to introduce da/dN and ΔK values manually. Based on the experimental results, the following crack growth rate curve parameters describing the Al 2024-T351 behavior have been extrapolated, ??:

Since experimental results are available only for specimen dimension 160*400*2, the numerical results achieved for the baseline configuration have been validated only on this geometry. the achieved results are reported in ??:

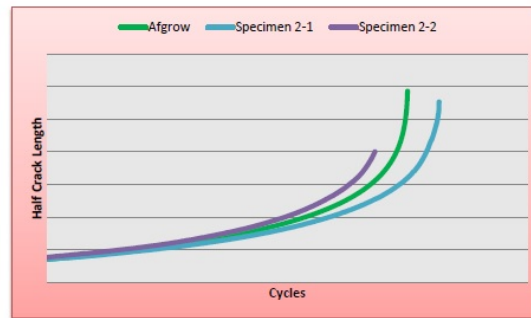


Figure 4.3: baseline validated result for Al 2024-T351

The numerical result achieved are close to the experimental ones, thus the adopted procedure which lead to the proper choice of parameters to define the Al 2024-T351 behavior, has been used for further analyses involving the laser treatment.

The laser effect has been introduced in the Afgrow by inserting additional residual stresses at user defined crack length increments, as in ??:

Afgrow gives the chance to introduce the normalized stress values in the

4.4. MATERIAL DESCRIPTION AFGROW FATIGUE LIFE PREDICTION

da/dN	ΔK
1.02e-04	10
1.24e-04	11
1.50e-04	12
1.82e-04	13
2.21e-04	14
2.67e-04	15
3.24e-04	16
3.92e-04	17
4.75e-04	18
5.76e-04	19
6.98e-04	20
8.46e-03	21
1.02e-03	22
1.24e-03	23
1.50e-03	24
1.82e-03	25
2.21e-03	26
2.68e-03	27
3.24e-03	28
3.93e-03	29
4.76e-03	30
5.77e-03	31
6.99e-03	32
8.47e-03	33
1.03e-02	34
1.24e-02	35
1.51e-02	36
1.83e-02	37
2.21e-02	38
2.68e-02	39

Table 4.2: Experimental values of da/dN and ΔK used for simulations

4.4. MATERIAL DESCRIPTION AFGROW FATIGUE LIFE PREDICTION

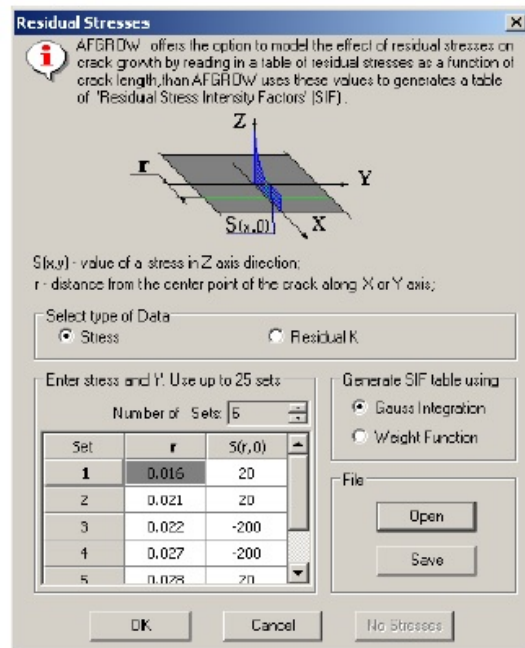


Figure 4.4: Residual stress definition within AFGrow

crack plane and to allow the software to calculate the corresponding SIF, or enter predetermined K values.

Residual stress intensities can be calculated by means of:

- Gaussian Integration Method
- Weight function Solution

The Gaussian Integration method is based on the stress intensity solution given by Tada, Paris and Irwin Stress intensity handbook to integrate a given 2-D unflawed stress field to estimate K at user defined crack length increments, ??.

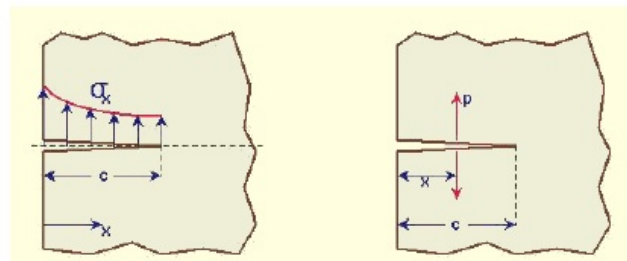


Figure 4.5: Model for SIF evaluation

4.4. MATERIAL DESCRIPTION AFGROW FATIGUE LIFE PREDICTION

$$K_I = \sum_{x=0}^C \sigma_x^* F(c, x) dx \quad (4.3)$$

$$F(c, x) = \frac{2}{\sqrt{\pi c}} \frac{1.3 - 0.05(\frac{x}{c}) - 0.2(\frac{x}{c})^2 - 0.3(\frac{x}{c})^3 + -0.25(\frac{x}{c})^4}{\sqrt{1 - (\frac{x}{c})^2}} \quad (4.4)$$

It is possible to implement the Weight function approach developed by Prof. Glinka only if a weight function solution is available for the analyzed geometry. The available weight function solution are reported in ??:

Model	Description of Configuration	Beta Solution
	Center Semi-Elliptical Surface Crack	Prof. Glinka
	Center Single Corner Crack at Hole	Prof. Glinka
	Internal Axial Crack in Thick Pipe	Prof. Glinka
	External Axial Crack in Thick Pipe	Prof. Glinka
	Center Through Crack	Prof. Glinka
	Single Edge Through Crack	Prof. Glinka
	Double Edge Through Crack	Prof. Glinka
	Radial Edge Crack in Disc	Prof. Glinka
	Axial Through Crack in Thick Pipe	Prof. Glinka

Figure 4.6: Available Weight Function

Results obtained for coupon dimension 400*160*2 mm are reported below. The crack growth behavior has been studied firstly for a configuration like that reported in ??

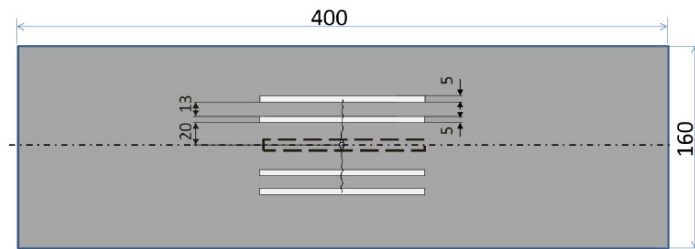


Figure 4.7: Specimen Configuration involving four 5 mm laser stripes

In this first approach a constant through the thickness compressive residual stress state has been considered, ??.

It has been noted that the best performance in terms of fatigue life is achieved when the two shot stripes are close to each other, as in ??:

4.4. MATERIAL DESCRIPTION AFGROW FATIGUE LIFE PREDICTION

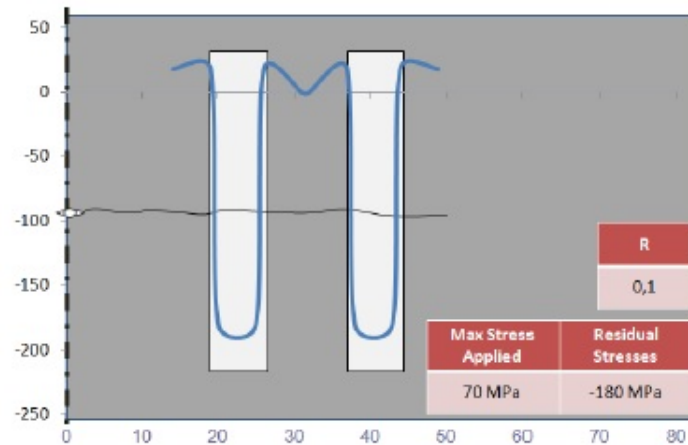


Figure 4.8: residual stress configuration for specimen characterized by 5 mm width laser stripes

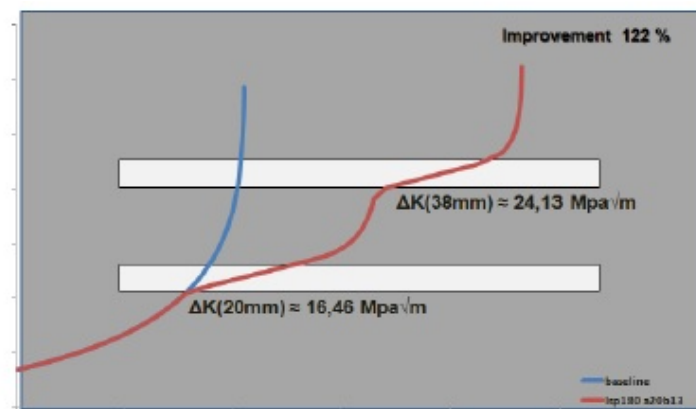


Figure 4.9: Improvement in fatigue life with 5 mm stripes on 400*160*2 mm coupon

4.4. MATERIAL DESCRIPTION AFGROW FATIGUE LIFE PREDICTION

An attempt to introduce a third stripe each side has been made, but since it lead only to an improvement in fatigue life estimated in the 10%, the improvement gained is not worth the cost of the laser stripes, so the best configuration in terms of fatigue life, at the lowest cost is that characterized by two stripes placed symmetrically within the component (total laser stripes within the target equal to four).

A further analysis has been developed involving two stripes each 10 mm wide, as in ??:

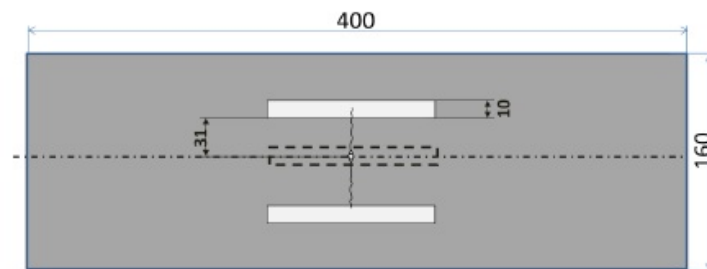


Figure 4.10: Specimen configuration characterized by 10 mm wide laser stripes

The simulated stress configuration adopted and the results achieved are reported in ?? and ??:

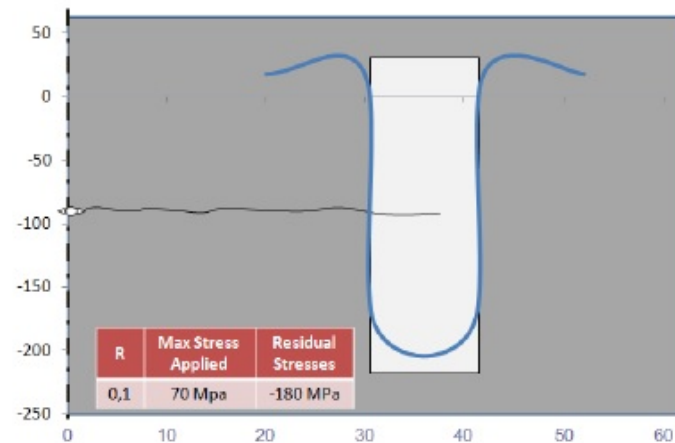


Figure 4.11: Stress configuration adopted for coupon characterized by 10 mm wide stripes

A further solution involving more 10 mm wide stripes couldn't be implemented since the net section yield reached when half the crack length is about 60 mm.

Second specimen configuration is referred to 400*800*2 mm. As done for the previous specimen dimensions a first configuration involving laser patterns 5 mm wide has been investigated. Again a constant through the thickness compressive residual stress field has been implemented, ??:

The inserted residual stress field is summarized in ??:

4.4. MATERIAL DESCRIPTION AFGROW FATIGUE LIFE PREDICTION

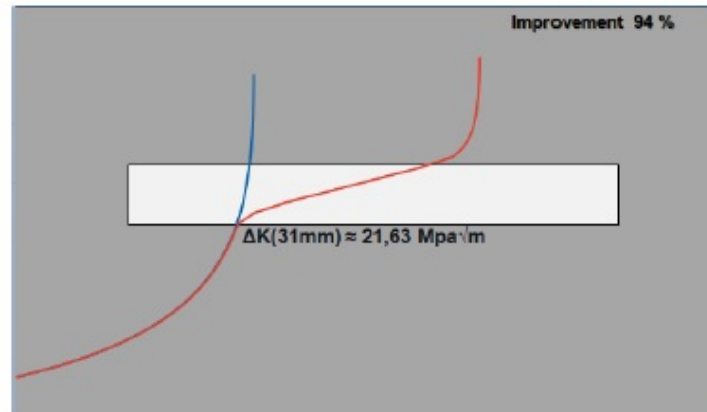


Figure 4.12: Crack Growth improvement for configuration based on 10 mm wide stripes

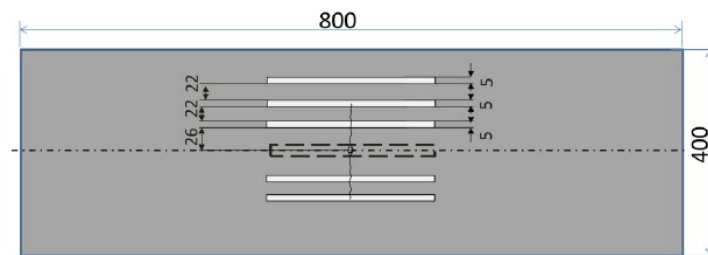


Figure 4.13: Specimen 400*800*2 mm, with 5 mm wide laser stripes

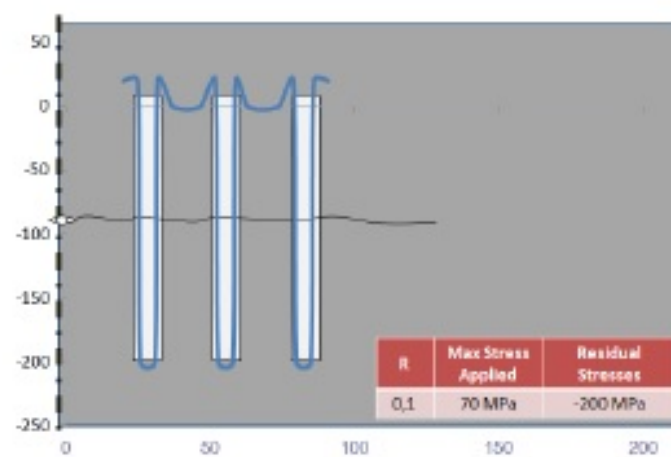


Figure 4.14: Residual stress in 400*800*2 mm coupon, laser stripes 5 mm wide

4.4. MATERIAL DESCRIPTION AFGROW FATIGUE LIFE PREDICTION

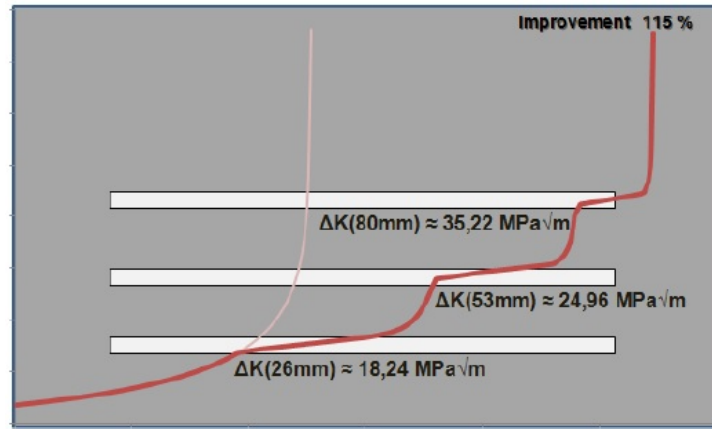


Figure 4.15: fatigue life improvement for coupon configuration 400*800*2 mm

The benefit in crack growth terms is reported in ??:

Again, the best crack growth behavior is reached when the three stripes are placed as close as possible to each other. Adding a further laser stripe in respect to the coupon center line, thus having 8 stripes in the coupon, leads to a benefit in fatigue life, which is quantified in a too small SIF increase; this is not sufficient to justify the costs connected to the experimental introduction of a further laser stripe.

A subsequent analysis involved laser stripes 10 mm wide, as in ??:

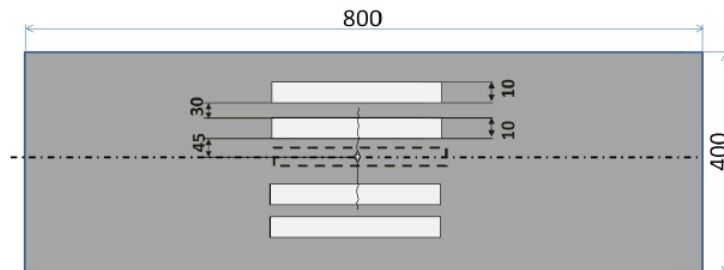


Figure 4.16: Specimen configuration 400*800*2 mm, laser patterns 10 mm wide

The simulated residual stress distribution from this configuration is reported in ??:

The results achieved in terms of crack growth slow down are reported in ??:

A further case characterized by laser pattern 20 mm wide has been implemented, resulting in the major benefit in terms of fatigue life behavior. The investigated configuration is reported in ??:

The inserted residual stress field can be represented as in ??:

Crack Growth benefit in terms of SIF is reported in ??:

What found from results achieved via AFGROW software prediction is that fatigue life increases with the laser pattern width and decreases with the laser stripes distance from each other.

4.4. MATERIAL DESCRIPTION AFGROW FATIGUE LIFE PREDICTION

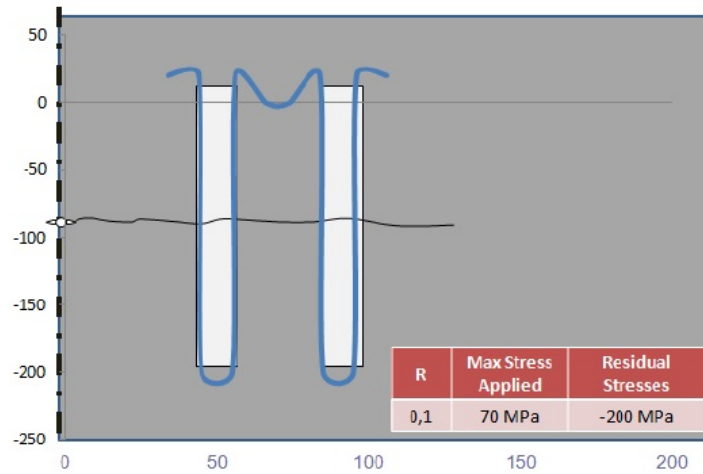


Figure 4.17: Residual stress inserted in coupon 400*800*2 mm, laser stripes 10 mm wide

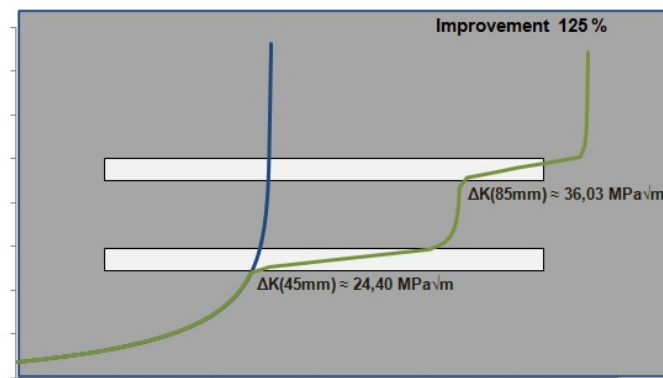


Figure 4.18: Crack growth improvement for coupon 400*800*2 mm, laser stripes 10 mm wide

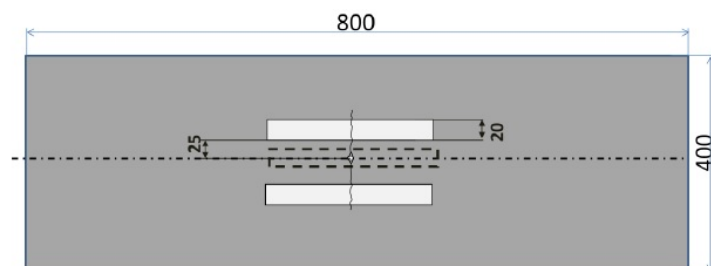


Figure 4.19: Specimen configuration 400*800*2 mm, laser stripes 20 mm wide

4.4. MATERIAL DESCRIPTION AFGROW FATIGUE LIFE PREDICTION

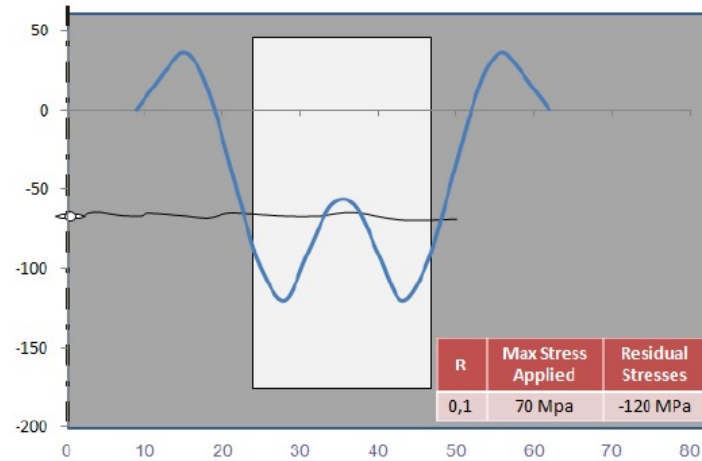


Figure 4.20: Residual stress field in 400*800*2 mm coupon geometry, laser stripes 20 mm wide

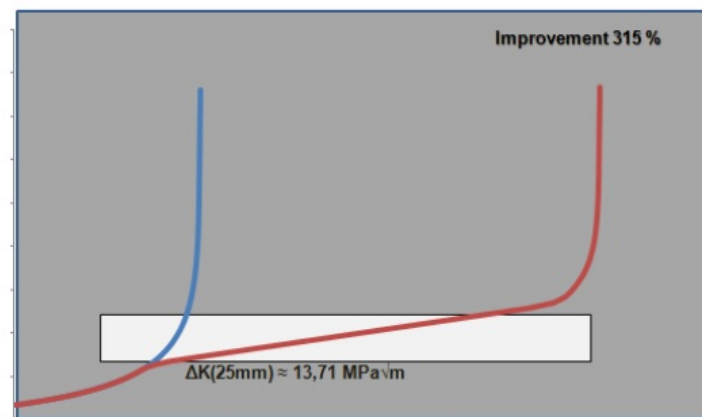


Figure 4.21: Crack growth benefit in 400*800*2 mm coupon, laser stripes 20 mm wide

4.4. MATERIAL DESCRIPTION AFGROW FATIGUE LIFE PREDICTION

Independently from the reliability of the achieved results, it is not completely understood the Afgrow procedure to estimate the crack growth behavior starting from a residual stress field manually introduced. It seems that Afgrow is based on algorithms which generate an error in the crack growth prediction when the two different methods, Gauss integral method and Weight Function method, are used.

For this reason, a new Matlab script, based on Terada's approach to estimate fatigue life of welded components, has been implemented. The analytical model has been validated with experimental results.

Bibliography

- [1] Jessica D'Ermilio. *Laser Shock Peening Treatment to Control and Moderate Fatigue Crack Growth in Aircraft Structure Based on Residual Stress Engineering Approach*, Scuola di ingegneria e architettura, universit di Bologna, 2013.

CHAPTER 5

Analytical Fatigue Life Prediction

5.1 Introduction

Flat thin aluminum panels with centered crack have been Laser Shock Peened along straight patterns perpendicular to the crack. Despite of the locally induced compressive residual stresses, the experimental tests, performed at Airbus Ottobrunn plant, showed the negative effect of the LSP on the fatigue crack propagation performances of panels. Starting from the numerical assessment of the self-balancing residual stress distribution along the entire panel width, the fatigue crack growth through the panels has been analytically evaluated and compared with experimental results, showing a good agreement. The comparison highlights the sensitivity of the fatigue crack propagation life to the selected LSP pattern configuration (i.e. the width of the LSP treated strip and the relative position to the crack centre) which have to be accurately setup in order to exploit the full potentiality of the LSP process in increasing the fatigue life and avoid undesired reduction of the component performances.

5.1.1 Geometry definition and experimental procedure

Three M(T) central cracked aluminum panels 2mm thick have been used in this investigation [7]. The panels, 160mm wide and 400mm long, have been LSP treated along two straight patterns, 10mm wide and 100mm long, located 50 mm from the specimen centerline, as shown in ???. The panels have been subjected to LSP treatment before the introduction of the central crack by the Universidad Politecnica de Madrid (UPM) with a Q switched Nd:YAG laser with 2.5 mm spot diameter, 178 pulse/cm² density and 0.75 mm shot overlapping were used to perform the LSP process. The central cracks has been machined as saw cuts perpendicularly to the LSP patterns into the panels which have been subjected to a pre-fatigue loading to achieve realistic sharp tip crack geometry before the fatigue crack propagation tests. The fatigue crack propagation tests have been performed by Airbus Group Innovations on the aforementioned three

panels identified as 2.1, 2.3 and 2.4. A constant amplitude fatigue load with $R = 0.1$ has been applied uniaxially perpendicular to the central crack.

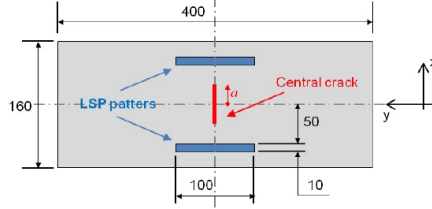


Figure 5.1: FCP specimen configuration

The experimental crack growth rate data as a function of the Stress Intensity Factor (SIF) are reported in ?? for the three investigated specimens. The LSP influence can be evaluated via comparison with a baseline, relative to the non-treated material. The baseline behavior has been extrapolated by means of the Paris C and n material coefficients calculated at the linear part of the ?? curves ($C = 2.10 \times 10^{-11}$; $n = 2.71$) and taking into account the effect of the finite-width of the panel expressed by the geometry factor below (a).

$$\beta(a) = \sqrt{\sec \frac{\pi a}{W}} \quad (5.1)$$

where a is the semi-crack length of the crack and W is the panel width.

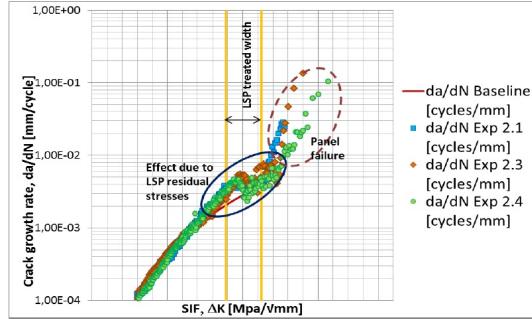


Figure 5.2: Fatigue Life, Paris Curve; experimental LSP coupon vs Baseline

A comparison of the experimental half-length crack vs fatigue cycles curves with baseline is shown in ??. A crack growth slowdown due to the laser peening has been highlighted in the crack propagation rate experimental data at the middle of the treated pattern. At the same time, a steep increase in the crack growth rate is evident before and after the shot pattern. This effect can be due to both the onset of plastic collapse and the self-equilibrating tensional residual stress accumulated in this area. The crack growth results show an overall negative effect of the laser shock peening process in comparison to the non-treated solution, because the crack growth rate is in every case higher than the baseline. The chosen geometric configuration, i.e. the relative position between the laser pattern and crack origin and the shot width, is unable to exploit the benefit of the compressive residual stress field induced by the LSP.

Furthermore, this configuration had a detrimental effect on the fatigue crack propagation performance of the cracked panel.

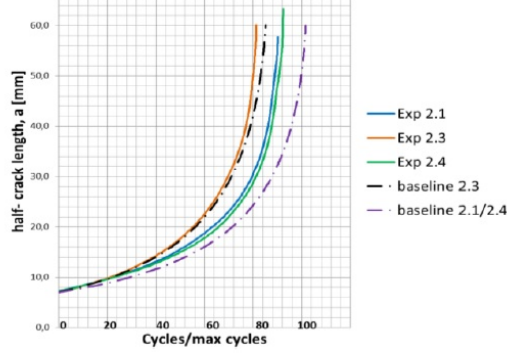


Figure 5.3: non dimensional a/N curves, compared with baseline.

The different behavior shown in ?? is due to the fact that, while in coupon 2.3 the crack propagates along the x horizontal axis, in the specimens 2.1 and 2.4 it develops with an angle of 45 degrees with respect to the previously mentioned axis. The 2.1-2.4 reference baselines have been evaluated taking into account the effect of the angled propagation expressed by a geometry factor in addition to the aforementioned finite-width geometry factor.

In order to predict how the laser pattern dimension and location affect the fatigue crack propagation performances of a thin-walled cracked panel, is fundamental to describe the self-balancing residual stress distribution along the entire panel width. An all explicit finite element model (Abaqus Software), which already proved to be effective in making such predictions, has been applied. The stress profile reported in ?? for half of the investigated panel has been obtained along the entire crack path. On the basis of the residual stress profile we have obtained using the finite element modeling is then possible to predict the fatigue crack propagation performances of the investigated panels by means of analytical models. The SIF $[K_{Res}(a)]$ of a crack propagating through a residual stress field can be calculated by the Eq.2:

$$K_{Res}(\pm a) = \frac{1}{\pi a} \int_{-a}^{+a} \sigma_{yRes}(\xi) \sqrt{\frac{a \pm \xi}{a \mp \xi}} d\xi \quad (5.2)$$

where the function $y_{Res}()$ describes the profile of the residual stress component orthogonal to the crack path. Tada proposed an analytical formulation of the residual stress profile established in a welded panel across the welding bead

$$\sigma_{yRes}(x) = \sigma_0 \frac{1 - \left(\frac{x-L}{c}\right)^2}{1 + \left(\frac{x-L}{c}\right)^4} \quad (5.3)$$

By means of an accurate selection of the shape parameters c , L and σ_0 of the Tada equation, the analytical formulation can describe accurately the residual stress profile calculated numerically for the LSP treated panel (??). L is the distance between the crack centre and the LSP pattern centreline, c is

representative of the point in which the residual stress field changes from tensile to compressive and σ_0 is the compressive peak stress value.

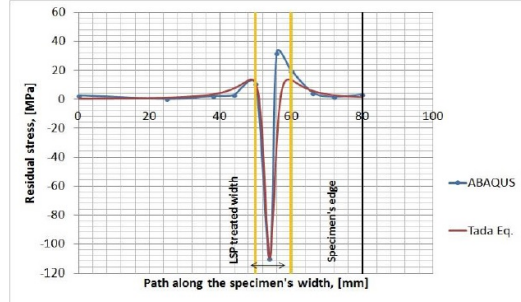


Figure 5.4: Numerical and analytical evaluation of Residual Stress Field

In ?? a mismatch of the numerical residual stress profile and its analytical representation is evident at the LSP pattern side close to the panel edge. This is due to the edge effect captured by the finite element model and not taken into account by the analytical formulation. Moreover, tensile residual stresses are established in both the sides of the LSP pattern in order to restore the global stress equilibrium of the panel. The tensile stresses predicted at the inlet to the shot pattern are lower than that at the exit, explaining the moderate acceleration in crack propagation shown by the tests results, in respect to the baseline, before reaching the pinned line, and subsequently slowing down in the central area, before the final sharp increase of the FCP. The prediction of fatigue crack propagation behavior of the investigated panels with the aforementioned SIF model for the residual stress field taking into account the finite-width of the panel, has been compared with the experimental measurements (??), showing good agreement.

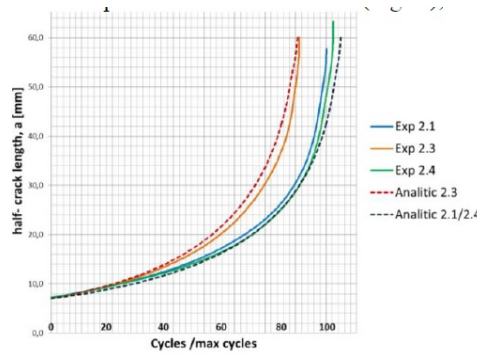


Figure 5.5: Effect due to LSP, comparison between the test results and the analytical evaluations

5.1.2 Parametric analysis on geometric parameters influence

A parametric analysis on the effect of the LSP pattern position and width on the FCP performances has been carried out. The proposed analytical crack propagation model implementing the Tadas residual stress distribution has been used, with the following parameters:

- laser pattern width of 10 mm; compressive residual stress of -100MPa and -150 MPa; distance between crack origin and peened area of 15 mm, 26.5 mm and 50 mm.
- laser pattern width of 33 mm; compressive residual stress of -100MPa and -150 MPa; distance between crack origin and peened area of 26.5 mm and 61.5 mm.

The results are shown in ?? and summarized in Table ?? and ?. An increase in FCP life is achieved only when the peening pattern is closer to the initial crack origin, at 15mm. Similarly, a larger laser shot width and higher compressive residual stresses were producing the best results in terms of FCP. The lack of benefit in the actual experimental configuration can be explained with the effect of the balancing tensile field before the shot pattern that, acting to a long crack, provides a significant contribution to the crack driving force. As a consequence, the tensile residual stress field before the shot path counteracts the subsequent compressive stresses in retarding the crack propagation.

Specimen	15 mm	26.5 mm	50 mm
RS=-100 MPa; Shot Path=10 mm	23.7	0.004	-1.77
RS=-150 MPa; Shot Path=10 mm	74.98	7.9	-2.43

Table 5.1: Percentage variation of the fatigue life referred to the baseline, laser pattern 10 mm

Specimen	26.5 mm	50 mm
RS=-100 MPa; Shot Path=33 mm	47.5	-11.9
RS=-150 MPa; Shot Path=33 mm	291.18	-15.52

Table 5.2: Percentage variation of the fatigue life referred to the baseline, laser pattern 33 mm

5.1.3 Conclusions

The objective of this work was to investigate the enhancement in fatigue crack propagation performances induced by LSP on structures which are representative

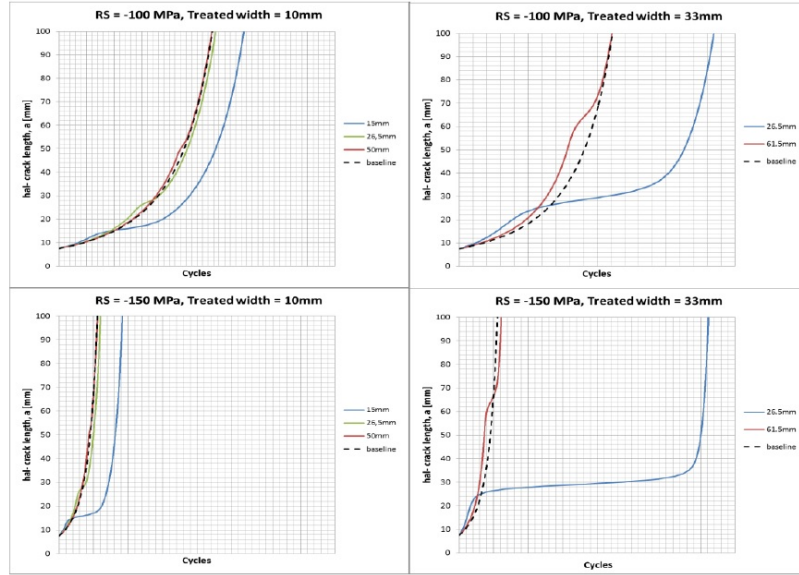


Figure 5.6: Fatigue Life Estimation with Terada and Tada modeling technique

of aircraft fuselage skin. The experimental data obtained on simple specimen show no improvement achieved with the selected configuration of the LSP treated pattern. Using a previously validated FEM approach to predict the residual stress profile along the entire width of the LSP treated specimen, together with an analytical crack propagation model, a comparison of the FCP predicted performances has been done with the experimental data available, showing a good agreement. The model was then used to make predictions about the best peening configuration to achieve benefit in terms of fatigue crack propagation life after LSP treatment. This lead to the conclusion that, to extend component fatigue crack propagation life, the laser shot has to be placed close to the crack origin and a larger shot pattern has to be used. In this case, LSP can be very effective in enhancing fatigue life performances.

Bibliography

- [1] U. Heckenberger, E. Hombergsmeier, V. Holzinger, W. von Bestenbostel. *Advances in Laser Shock Peening theory and practice around the world: present solutions and future challenges*, Proceedings of the 2nd International Conference on Laser Peening, Emerald Group Publishing Ltd., Bradford, 2011, p. 22-33.
- [2] G. Ivetic, I. Meneghin, E. Troiani et al. *Fatigue in laser shock peened open-hole thin aluminium specimens*, Materials Science and Engineering A 534 (2012) 573-579.
- [3] G. Ivetic, E. Troiani, I. Meneghin et al. *Characterization of fatigue and crack propagation in laser shock peened open hole 7075-t73 aluminium specimens*, in Proceedings of ICAF 2011 Symposium, Montreal, Canada, 2011.
- [4] G. Ivetic, E. Troiani, I. Meneghin et al. *Characterization of fatigue and crack propagation in laser shock peened open hole 7075-t73 aluminium specimens*, in Proceedings of ICAF 2011 Symposium, Montreal, Canada, 2011.
- [5] G. Ivetic, E. Troiani, I. Meneghin et al. *Characterization of fatigue and crack propagation in laser shock peened open hole 7075-t73 aluminium specimens*, in Proceedings of ICAF 2011 Symposium, Montreal, Canada, 2011.
- [6] C. Rubio-Gonzalez, J.L. Ocana, G. Gomez-Rosas, C. Molpeceres, M. Paredes, A. Banderas, J. Porro, M. Morales. *Effect of Laser shock processing on fatigue crack growth and fracture toughness of 6061-T6 aluminium alloy*, , Material and Science Engineering A 386 (2004) 291-295.
- [7] S. Huang, J.Z Zhou, J. Sheng, K.Y. Luo, J. Z. Lu, Z. C. Xu, X. K. Meng, L. Dai, L. D. Zuo, H. Y. Ruan, H. S. Chen. *Effects of Laser Peening with different coverage areas on fatigue crack growth properties of 6061-T6 aluminium alloy*, International Journal of Fatigue 47 (2013) 292-299.
- [8] S. Huang, J.Z Zhou, J. Sheng, J. Z. Lu, G. F. Sun, X. K. Meng, L. D. Zuo, H. Y. Ruan, H. S. Chen. *Effect of Laser Energy on fatigue crack growth properties of 6061-T6 aluminium alloy subjected to multiple laser peening*, Engineering Fracture Mechanics 99 (2013) 87-100.

-
- [9] D. Furfari, N. Ohrloff, E. Hombergsmeier, U. Heckenberger, V. Holzinger. *Enhanced Fatigue and Damage Tolerance of Aircraft Components by Introduction of Residual Stresses A Comparison of Different Processes*, in A. Brot (Ed.), Proceedings of ICAF 2013 Symposium, Jerusalem, Israel, 2013.
 - [10] P.C. Paris, H. Tada, G. Irwin. *The Stress Analysis of Cracks Handbook*, 3rd edition, p.127, ASME Press, New York, 2000.
 - [11] S. Taddia, E. Troiani, C. Crudo. *Numerical Investigations on Laser Peening Process*, in J.L. Ocana (Ed.), Proceedings of the 4th international conference on laser shock peening and related phenomena, Madrid, Spain, 2013.
 - [12] E. Troiani, C. Crudo, G. Molinari, S. Taddia. *Investigations on Laser Peening Capability by finite element simulations*, in A. Brot (Ed.), Proceedings of the ICAF 2013 Symposium, Jerusalem, Israel, 2013.
 - [13] G. Ivetic, I. Meneghin, E. Troiani. *Numerical analysis of Laser Shock Peening as a process for generation of compressive residual stresses in open hole specimens*, Materials Science Forum 681 (2011) 267-272.
 - [14] H. Terada. *Stress Intensity factor analysis and fatigue behaviour of a crack in the residual stress field of welding*, Fatigue of aircraft structures 1 (2011) 5-15.
 - [15] H. Tada, P.C. Paris. *The stress intensity factor for a crack perpendicular to the welding bead*, International Journal of Fracture 21 (1983) 279-284.

CHAPTER 6

RS measurement

Aim of this chapter is to provide informations about the residual stress measurement techniques, with particular emphasis on X-Ray diffraction method which has been adopted to characterize the residual stress left by Laser Shock Peening Treatment at Elettra facilities in Trieste. Beneficial residual stresses can be introduced deliberately, as in case of laser shock peening; for this reason it is important to have reliable methods for the measurement of these stresses and to understand the level of information they can provide.

6.1 Measurement Techniques

The knowledge of the effective residual stress field within a component is mandatory in the engineering process to understand how its magnitude and distribution affect the fatigue life of the structure. Nowadays, several residual stress measurement techniques are available depending on different materials and component configuration, so the choice of the one which suites better for the case under investigation is of primary importance. Cross check of different measurement techniques can helping understanding the effective residual stress field characterizing a component.

In this chapter an overview on the following measurement techniques is given:

- Hole Drilling Technique
- Contour Method
- Neutron Diffraction Method
- Synchrotron X-Ray Diffraction

6.1.1 Residual Stress

The residual stress, which is the stress remaining in a structure after loading removal, is auto-balanced, this way two possible state are recognized:

- If

$$\sum F = \int \sigma dA \quad (6.1)$$

the sample has always been in the elastic region

- If

$$0 = \int \sigma dA \quad (6.2)$$

somewhere in the sample the yield has been reached, thus leading to plasticity.

Residual stress cannot be measured directly, but are obtained from strains, which are linked to the distance between the crystal lattices as in ??:

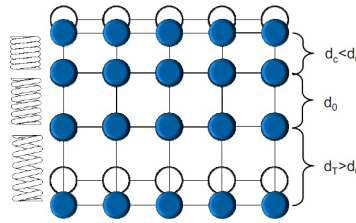


Figure 6.1: residual stress are linked to crystal lattices distances

From ?? it can be seen that a compressive residual stress state is linked to a shorter distance between atom whereas a longer distance between them corresponds to a tensile stress state.

There are two different approaches for residual stress measurement ??:

Destructive	Non Destructive
Consist in: cutting the sample having a residual stress release as a consequence recording the strain modification	Record strains without modifying the residual stress field
The main are: Hole Drilling Technique Contour Method Slitting Method	The main are: X-Ray Diffraction Neutron Diffraction Ultrasonic Method

Table 6.1: Residual Stress Technique

6.1.2 Contour Method

The Contour Method can be summarized in the following two pictures ??, ??:

The contour method consists in cutting the sample without introducing plasticity, otherwise a different space between atoms is introduced that leads to an erroneous prediction of the residual stress field. The cut is done by means of electrical discharge machining. This method is not suitable for surface residual

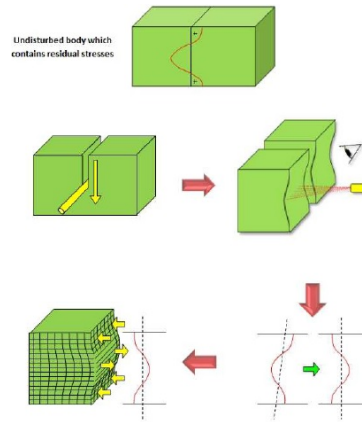


Figure 6.2: Contour Method Principle

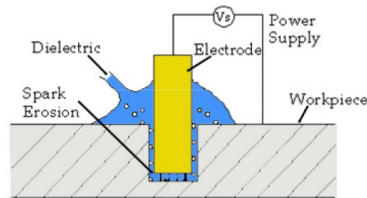


Figure 6.3: Electrical Discharge Machining

stress measurement of thin components. The contour method gives a 2D map of the residual stress field rather than a measurement in just one specific point as with hole drilling technique.

Pro	Cons
Allows to measure residual stress in big components spatial resolution is imposed by the user, usually it is one of the smallest among the residual stress measurement techniques	Only one stress component can be measured for each cut once the sample is cut, all the residual stress field is changed experience in cutting the sample

Table 6.2: Pro and Cons of Contour Method

6.1.3 Incremental Hole Drilling

This measurement technique is quite fast and cheap; it is a semi-destructive and based on measurement of the stress relaxation due to incremental hole drilling of a small hole. Incremental hole drilling, which has been adopted to characterize the residual stress field of the laser peened coupon in Universidad Politecnica de Madrid, requires three steps:

- Glue the strain gage on top of the sample surface

- Drill incremental holes
- Compute the recorded strains and calculate the stress

Incremental Hole drilling can be summarized in the following ??:

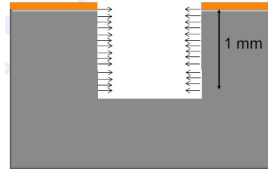


Figure 6.4: Incremental Hole Drilling

It is not possible to measure residual stresses at depth of more than 1 mm under the surface hosting the strain gage, since even if the technique implies going slowly deeper within the component thickness without heating it, the strain gage is still on the top surface, so measurement deeper than 1 mm are no longer reliable. Pro and cons of incremental hole drilling are reported in the following ??:

Pro	Cons
the residual stress field can be measured from 16 μm to 1.2 mm underneath the specimen surface	Only the in plane stress component can be measured specimen thickness of at least 6 mm horizontal spatial resolution must be at least 6 times the tip diameter, as imposed by ASTM

Table 6.3: Pro and Cons of Incremental Hole Drilling

When considering the use of the hole drilling technique, difficulties can occur due to an alteration of the stress field, while drilling the hole in the coupon, and also in the definition of well defined geometries of the holes. There are four most famous drilling techniques, which are:

- low speed drilling
- high speed drilling
- air abrasive jet machining
- electro chemical milling

Regarding the air abrasive jet machining, this is characterized by the following ??:

The four most commonly used methods to calculate the residual stresses given the strains are:

- incremental strain method

Pro	Cons
Quick	No control of the hole shape
Portable	Limited control of the incremental measurements

Table 6.4: Pro and Cons of air abrasive jet machining

- average stress method, by Nikola, uses the concept of a uniform stress which equals the spatial average of the equivalent uniform stress before the hole depth increment plus the stress within the increment; but this is invalid because the stress closer to the surface contribute more to the strain relaxations than the stresses farther from the surface.
- power series method, by Schajer, which implies the use of a technique which allows to achieve a better fit curve through the measured strain data, but is only applicable to smoothly varying stress fields
- integral method

Vibrations during measurements can influence the the achieved measured results.

Of great importance is the grinding and polishing of the coupon before proceeding with any kind of measurement technique; when doing so, it is important to not introduce farther deformations in order to not change the achieved residual stress field.

In order to have reliable measurements, the gauge rosette to perform hole drilling has to be placed in areas which are not interested by scribe marks.

6.1.4 Neutron Diffraction Method

This measurement technique is non destructive and uses high energy neutrons to evaluate the lattice deformations. The impacting neutrons will be reflected by the specimen. The measurement of the reflection angles gives important informations about the internal state of stress, according with the Bragg's Law.

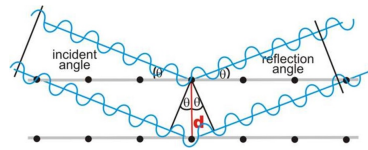


Figure 6.5: Bragg's Law Principle 1

Bragg's Law can be summarized in the following ??:

$$n\lambda = 2d\sin\theta \quad (6.3)$$

The residual stress calculation:

$$\epsilon = \frac{d_{c,t} - d_0}{d_0} \quad (6.4)$$

where:

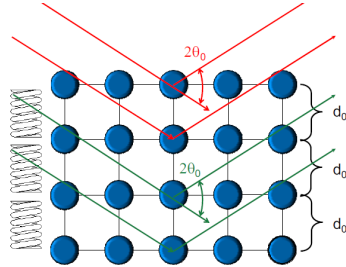


Figure 6.6: Bragg's Law Principle 2

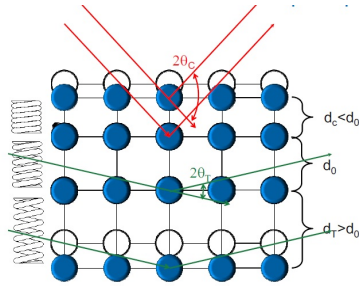


Figure 6.7: Bragg's Law 3

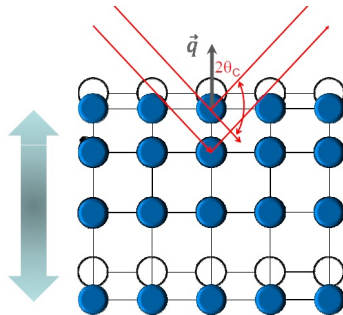


Figure 6.8: Bragg's Law Principle 4

6.1. MEASUREMENT TECHNIQUES CHAPTER 6. RS MEASUREMENT

- $d_{c,t}$ is the distance between lattice planes in case of compressive or tensile residual stress
- d_0 is the distance between lattice planes at equilibrium

$$\sigma_i = \frac{E}{1 - \nu^2}(\epsilon_i + \nu\epsilon_j) \quad (6.5)$$

There are two ways to produce neutrons:

- Nuclear Reactor
- Spallation Source

Pro and Cons of the both are summarized in the following ??

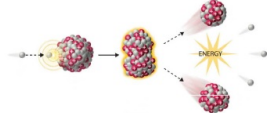
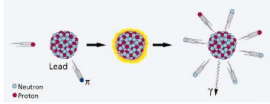
Nuclear Reactor	Spallation Source
	
Only one wavelength, so only one reflection plane according with the tested material	Several wavelength used, so more planes at same time thus increasing statistics
Higher energy involved	Less energy involved
Faster measurement, typically 5 min for Aluminum alloys	Slower measurements, typically 40 min for Aluminum alloys
More dangerous	Less dangerous

Table 6.5: Pro and Cons of Nuclear reactor source and Spallation Source

Depending on the Miller Indices, lattice planes with the same orientation, scatter the neutron in the same direction. In picture ??:

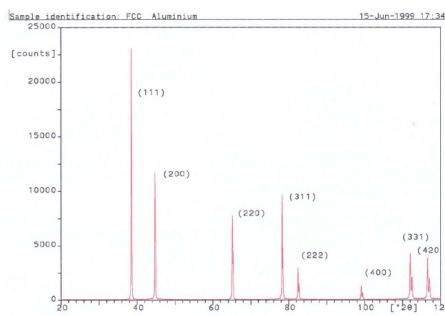


Figure 6.9: Counts

are reported the counts , thus each peak gives an idea of how many neutrons are reflected in the corresponding direction, identified by Miller Indices, as written on top of each peak. Peaks are different for different materials and different crystal lattices ??:

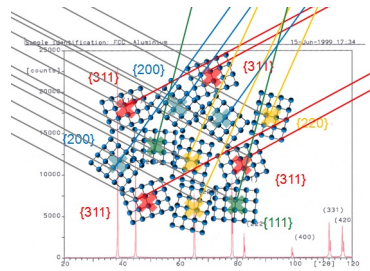


Figure 6.10: Lattice Planes reflecting neutrons

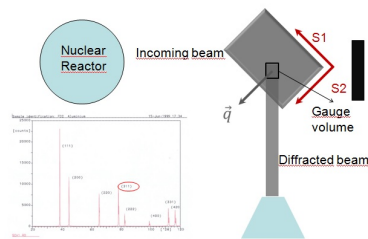


Figure 6.11: Nuclear Reactor Working Principle

Unfortunately, looking at ??, the metallic materials grains have many different orientations. The same orientation scatters the neutrons or photons with the same angle.

In ??, the gage volume is an area of material, squared, which reflects neutrons while measuring and (311) lattice plane scatters close to 90 degree.

As can be seen in ??, aluminum is not composed only of (311) lattice planes but the (311) is the one reflecting neutrons, and this is related to the material Young modulus. While setting parameters at Elettra facilities great attention must be paid to the Young modulus associated to the chosen reflecting plane ??

	<i>Al</i>
$(2(S_{11} - S_{12}))/S_{44}$	1.22
E_{200} (GPa)	63.7
E_{311} (GPa)	69.0
E_{420} (GPa)	69.1
E_{531} (GPa)	71.1
E_{220} (GPa)	72.6
E_{331} (GPa)	73.6
E_{111} (GPa)	76.1
	70 GPa

Figure 6.12: Young modulus associated with corresponding lattice plane in aluminum

6.1.5 X-Ray Diffraction Method

Every time we accelerate or decelerate a charged particle, a photon is produced. In case we use electrons, photons are produced in the X-Ray frequency.

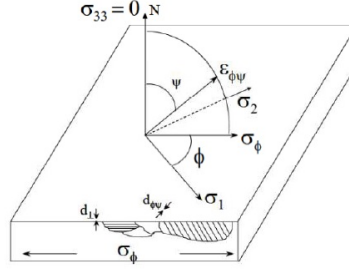


Figure 6.13: Surface X-Ray parameters

Looking at ??, residual stresses can be find as follows:

$$\epsilon_{\phi\psi} = \frac{d_{\phi\psi} - d_0}{d_0} = \frac{1 - \nu}{E} \phi \sin^2 \psi - \frac{\nu}{E} (\sigma_1 + \sigma_2) \quad (6.6)$$

$$d_{\phi\psi} = ((\frac{1 + \nu}{E}) d_0 \sigma_{\phi}) \sin^2 \psi - (\frac{\nu}{E}) (\sigma_1 + \sigma_2) d_0 + d_0 \quad (6.7)$$

which can be seen as a line equation ??:

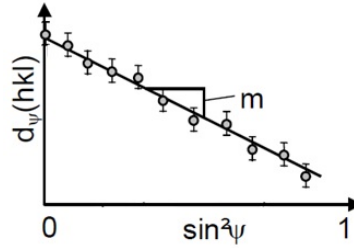


Figure 6.14: residual Stress X-Ray calculations

$$d_{\phi\psi} = y \quad (6.8)$$

$$((\frac{1 + \nu}{E}) d_0 \sigma_{\phi}) = m \quad (6.9)$$

$$\sin^2 \psi = x \quad (6.10)$$

$$(\frac{\nu}{E}) (\sigma_1 + \sigma_2) d_0 + d_0 = q \quad (6.11)$$

$$m = \frac{\partial d_{\phi\psi}}{\partial \sin^2 \psi} = (\frac{1 + \nu}{E}) d_0 \sigma_{\phi} \quad (6.12)$$

$$\sigma_{\phi} = \left(\frac{E}{1 + \nu} \right) \frac{1}{d_0} m \quad (6.13)$$

The principles at the basis of synchrotron XRD in measuring the residual stress field is that every particle whose trajectory is curved must have been accelerated by a centripetal acceleration ??;

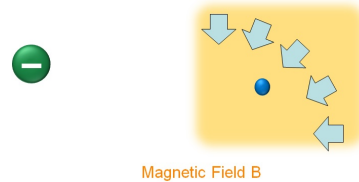


Figure 6.15: Synchrotron X-Ray radiation

The same result can be obtained by inserting electrons into a magnetic field. The Lorentz force acting on the particle will deviate its trajectory. Many different magnetic fields can be used to accelerate the electrons inside a closed loop: this is called synchrotron, ??:

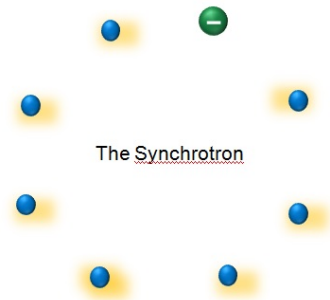


Figure 6.16: Electrons in a synchrotron

In the world there are few facilities in which this kind of measurements can be done, and are:

- Elettra (Trieste, IT) 260 m
- Soleil (Paris, FR) 354 m
- Diamond Light Source (Oxford, UK) 560 m
- APS (Chicago, USA) 1.100 m
- CERN (Geneva, CH) 27.000 m

Typically the synchrotron X-Ray gauge volume is 50 μm , while the length can reach 2 mm, as in ??

Main optical components required for residual stress measurement at devoted beam in a Synchrotron facility are ??:

The peak choice associated with the residual stress measurement is derived from ??:

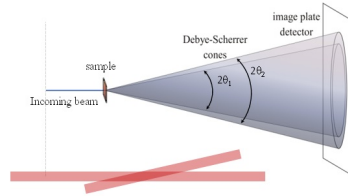


Figure 6.17: Synchrotron Gauge Volume

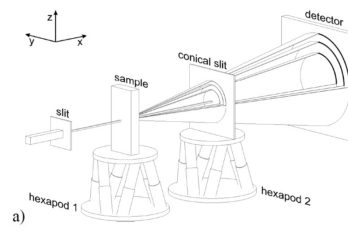


Figure 6.18: Residual Stress measurement optical system in devoted beam

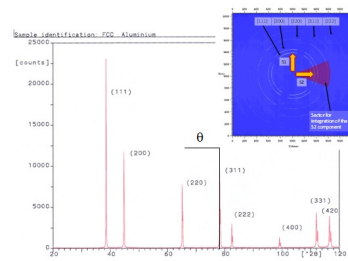


Figure 6.19: Peak Choice

Being:

$$\theta_{measured} \rightarrow d \rightarrow \epsilon \quad (6.14)$$

and

$$\theta_0 \rightarrow \epsilon = -\cot \theta_{measured}(\theta_{measured} - \theta_0) \quad (6.15)$$

X-Ray Diffraction method can be applied only to crystal structures. The X-Ray beam is characterized by only one wavelength of the same magnitude as the atomic spacing. The diffraction phenomenon can be summarized as follows. When the beam hits the material, X-Ray scatter in all directions, but some of that reflected by an atom cancel out with others; this way only the ones striking certain crystallographic planes at specific angles are reinforced. The beam is reinforced when Bragg's Law is satisfied:

$$\sin \theta = \frac{\lambda}{2d_{hkl}} \quad (6.16)$$

where:

- θ is half the angle between the diffracted and the original beam
- λ is the X-Ray wavelength
- d_{hkl} is the distance between planes causing the beam reinforcement

The above-mentioned parameters are reported in ??:

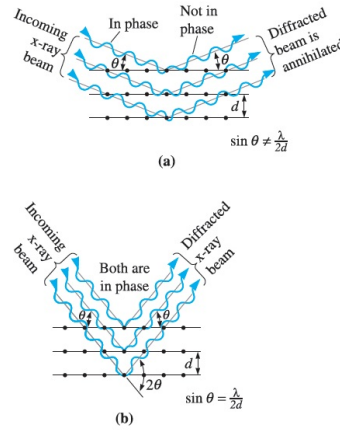


Figure 6.20: Bragg's Law Parameters

Picture ??, reports in (a) the case in which the diffracted beam is annihilated, whereas case (b) the one in which the diffracted beam is reinforced. As can be seen in ??:

a diffractometer records the 2θ angles of the diffracted beam giving the diffraction pattern which can be seen in ?? (a) and (b). This way the knowledge of the x-ray wavelength allows to calculate the inter-planar spacing and identify the planes that cause diffraction.

Diffraction Method Pro and Cons are summarized in the following ??:

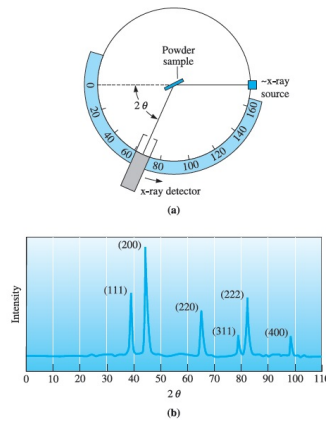


Figure 6.21: Diffractometer

Pro	Cons
Measurement can be carried out very close to the surface (17 μm from the top surface) as far as 30 cm within the sample	To access facilities, approval of a work proposal is needed
Spatial resolution from 50 μm to 1 mm and up	If facility is not working properly due to energy level provided for eg., the experiment is postponed
	High cost

Table 6.6: Pro and Cons X-Ray Diffraction Method

6.2 Material characterization

In order to understand the choice of the adopted beam parameters, a focus on the material properties, in terms of crystal lattice and mechanical characterization has to be provided.

Stress term refers to a force per unit area. Residual Stresses are those left by machining or treatment after load removal. Application of stresses causes strains. Elastic strains is that which go away after load removal; this case stress and strain are linearly related by the Young modulus. Plastic strain are those which remain after load removal; yield strength is the stress level at which plastic strain starts to develop. The arrangement of atoms in a material is known as structure. If atoms are arranged in a periodic fashion, the material is known as crystalline. The characteristic of crystalline and grains influences the fatigue behavior of the component.

A better understanding of the definition of the Young modulus is required in order to explain how the same parameter value has been chosen for the material under investigation at Elettra facilities. The elastic modulus is also related to the atomic spacing, which is defined by an equilibrium solution between attractive and repulsive forces. The Young modulus is the slope E in the stress strain curve, but is also related to the force-distance curve.

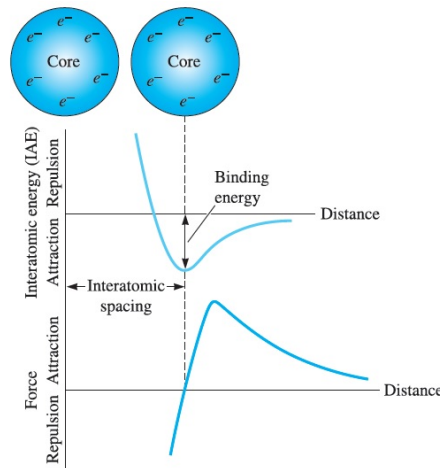


Figure 6.22: Young Modulus definition

The material has a high modulus of elasticity when the curve slope is steeper, since this means a greater force is required to stretch the bond.

The elastic modulus does not depend on the material micro structure, since two aluminum samples with the same chemical composition but different grain scale, have the same elastic modulus but different yield strength, since this latter is a micro structure sensitive properties. The grains are the smaller crystal which form a polycrystalline material. The border of these crystals are grain boundaries. Grain boundaries affect the fatigue performance of materials. A lattice is a purely mathematical collection of points which divide the space into smaller equally sized segments. A unit cell is a lattice subdivision which still contains the lattice properties. Cubic crystal system is divided in:

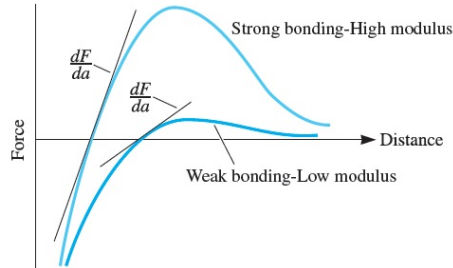


Figure 6.23: Force Distance curve for two materials, difference in the elastic modulus

- simple cubic (SC)
- face-centered cubic (FCC)
- body- centered cubic (BCC)

All the reported configurations are referred to the different position of lattice points in the unit cell.

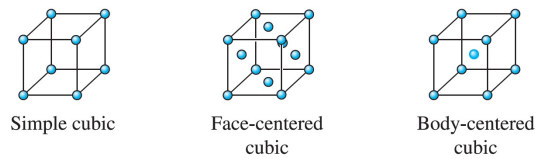


Figure 6.24: Cubic Crystal System

Miller Indices are used to describe directions in the unit cell. Miller Indices are then used to set parameters at Elettra facilities. The procedure for finding the Miller Indices for direction is ??:

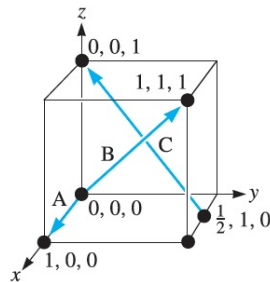


Figure 6.25: Miller Indices, eg.

- For point A:
- The two points are (1 0 0) and (0 0 0)
- Subtracting each other : $1\ 0\ 0 - 0\ 0\ 0 = 1\ 0\ 0$

- this case there are no fraction to reduce by integers
- Miller Index is $[1\ 0\ 0]$
- For point B:
- The two points are $(1\ 1\ 1)$ and $(0\ 0\ 0)$
- Subtracting each other : $1\ 1\ 1 - 0\ 0\ 0 = 1\ 1\ 1$
- this case there are no fraction to reduce by integers
- Miller Index is $[1\ 1\ 1]$
- For point C:
- The two points are $(0\ 0\ 1)$ and $(\frac{1}{2}\ 1\ 0)$
- Subtracting each other : $0\ 0\ 1 - \frac{1}{2}\ 1\ 0 = -\frac{1}{2}\ -1\ 1$
- $2(-\frac{1}{2}\ -1\ 1) = -1\ -2\ 2$
- Miller Index is $[\bar{1}\ \bar{2}\ 2]$

Material whose properties depend on the crystallographic direction are anisotropic, and this is the case of aluminum; Young Modulus of aluminum is 75.9 GPa in $(1\ 1\ 1)$ directions, but is only 63.4 GPa in $(1\ 0\ 0)$ directions. This is an important parameter to set when dealing with residual stress measurement depending on the crystal lattice of interest. Materials as aluminum which which is crystallographically anisotropic can behave as isotropic if in a polycrystalline form, because the random orientation of different crystals will cancel out with the effect of the anisotropy as a result of the crystal structure. The inter-planar spacing (d_{hkl}) is the distance between two adjacent parallel planes of atoms with the same Miller indices. The inter-planar spacing in cubic material is given by the general equation ??:

$$d_{hkl} = \frac{a_0}{\sqrt{h^2 + k^2 + l^2}} \quad (6.17)$$

where:

- a_0 is the lattice parameter
- h, k, l are the Miller indices of the adjacent planes being considered

Bibliography

- [1] Donald R. Askeland. *The Science and Engineering of materials* Third Edition, 1996.
- [2] Stefano Coratella. *Seminar in Residual Stresses Measurement Techniques*, University of Bologna, 26 November 2014.
- [3] Grant, Lord, Whitehead. *The measurement of residual stress by incremental hole drilling technique*, Measurement good practice guide, n.53, national physical laboratory, uk.
- [4] Cullity, Stock. *Elements of X-Ray Diffraction*, prentice hall, upper saddle river.
- [5] Mitchell, Perez-Rairez. *X-Ray diffraction*, lecture notes from institute of chemical and bioengineering, eth Zurich, Switzerland, cc.usst.edu.cn, 14 november 2012 (internet download).
- [6] Prevey. *Current application of X-Ray diffraction residual stress measurement, development in materials characterization technologies*, eds Van Der Voort, 1996.
- [7] Roy, Wells. *Comparison of residual stress measurements by different techniques*, internet, 14 november 2012.
- [8] *X-Ray diffraction technique*, www.readbag.com, 14 november 2012.

CHAPTER 7

Experimental RS measurements by XRD

Aim of this chapter is to provide informations about the residual stress measurement by X-Ray diffraction done at Elettra facility in Trieste; a comparison between the residual stresses achieved for different laser set up parameters will also be provided.

Before entering the Elettra facilities to perform X-ray diffraction measurement, a work proposal has to be written and accepted.

It has to be taken into account that, x-ray diffraction technique allows to characterize only the close to the surface residual stress field. Treatments such as laser shock peening introduce compressive residual stresses at deeper depth under the coupon surface, which can be measured only by means of techniques such as incremental hole-drilling.

Anyway, the coupon adopted within this work of thesis are so thin, 1.4 mm thick, that, referring to the residual stress evaluation achieved by means of the validated Kinematic Hardening numerical model for thin coupons, it can be well estimated a compressive residual stress characterizing the all target thickness. The small difference in the compressive residual stress field achieved between the two side shot surfaces of the coupon, is due to the fact that, in order to not result in a non acceptable distortion of the target, the laser set up parameters used when shooting the two surfaces are changed.

X-ray diffraction can be regarded as the more reliable measurement technique since hole drilling reliability depends on the operator ability to perform the measurement, as well as on the adopted testing machine and instruments.

7.1 X-Ray Diffraction Measurement Technique

X-ray diffraction technique is suitable only for crystalline materials with fine grains. X-Ray allows to measure the macro-stresses present in the structure, since the strain distortion of the crystal lattice shifts the angular position of the diffraction peak selected for residual stress measurement. Macro-stresses are those of interest in analyzing the fatigue life of components. Micro-stresses are

7.1. X-RAY DIFFRACTION EXPERIMENTAL TECHNIQUES BY XRD

imperfections in the crystal lattice which cause the broadening of the diffraction peak.

Measurement of at least two orientation defined by different ψ angles, allows to characterize the stress present on the sample surface.

Only elastic strains contribute to the formation of macro-stresses, since contributing to an alteration of the crystal lattice spacing. Plastic strains contribute to dislocation motion and break of the crystal lattice, thus creating micro-stresses. Even if residual stresses are originated also from plastic strains, the only macro-stresses remaining in a structure are those coming from elastic strains.

The residual stresses are measured by means of X-Ray diffraction in a restricted volume, depending on the beam hitting the coupon surface, and depth depending on the absorption coefficient of the material for the radiation used. Since the diffraction peak selected for residual stress measurement affects greatly the precision of the method, usually in the literature it is recommended to use 2θ angles not less than 120° . For aluminum alloys the values for elastic constants and peak choice are reported in the following table ??:

Alloy	Radiation	Lattice		Elastic constants(a) ($E/1 = \nu$)				Linear		
		plane,	angle	GPa (10^6 psi)		Bulk		Absorption		
		(hkl)	(2θ),	(hkl)	Bulk	Error	$K_{48}(\text{b})$	Coefficient (μ)	cm ⁻¹	in. ⁻¹
		degrees								
Aluminum-base alloys										
2014-T6	Cr K α	(311)	139.0	59.4 ± 0.76 (8.62 \pm 0.11)	54.5 (7.9)	-8.3	387	56.2	442	1124
2024-T351	Cr K α	(311)	139.3	53.8 ± 0.55 (7.81 \pm 0.08)	54.5 (7.9)	+1.1	348	50.5	435	1105
7075-T6	Cr K α	(311)	139.0	$60.9 \pm .048$ (8.83 \pm 0.07)	53.8 (7.8)	-11.4	397	57.6
7050-T6	Cr K α	(311)	139.0	57.1 ± 0.41 (8.28 \pm 0.06)	53.8 (7.8)	-5.8	372	54.0	443	1126

Figure 7.1: Parameters for X-Ray Diffraction of aluminum alloys

When dealing with X-Ray measurements, it is important to properly position the coupon in relation to the hitting laser beam; the sample must be positioned at the center of rotation and the ψ angle must be constant through the irradiated area. It has to be noticed that X-Ray gives reliable results on flat surfaces only. The beam size has to be chose in relation to the residual stress field nature. An increase in the irradiated area causes a decrease in the data collection time. A decrease in the irradiated area which causes a decrease in the diffracted intensity by an order of magnitude, causes an increase on the collection time proportional to that decrease.

The principal sources of error related to X-Ray diffraction technique are linked to the proper location of the diffracted peak. Other sources of systematic error are:

- excessive surface roughness
- excessive surface curvature
- interference between the sample geometry and the diffracted beam
- coarse grain size, which lessen the number of crystals contributing to the diffraction peak thus resulting asymmetric peaks which are not properly localized

7.1. X-RAY DIFFRACTION MEASUREMENTS BY XRD

- definition of the X-Ray elastic constants such as $(\frac{E}{1+\nu})_{(hkl)}$, which can differ from the bulk value of 40% due to elastic anisotropy
- excessive residual stress gradients in the coupon depth can result in residual stress field wrong measurement, since residual stresses are calculated as averages

Some aspects have to be investigated before proceeding with X-Ray measurements, such as:

- Energy magnitude available at facility or wavelength
- Co-ordinate of the measurement system to define the zero position
- range of 2θ angles to be scanned
- Chi angles
- Sample translation, if measurements are going to be taken at different sample locations
- Duration time of each count

All the above-mentioned parameters can be set and checked by means of the PINCER software available at Elettra facility Beam-line.

The energy level is selected by beam-line staff, depending on the selected crystal for the desired wavelength at which the measurement will be carried out. Since this procedure requires at least two hours, it is preferable to perform all the measurement requiring the same wavelength in a row. The main advantage of using a synchrotron is that it provides light sources which make it possible to achieve deeper measurement in respect to the traditional light sources. The energy level available at the residual stress beam line depends on the synchrotron energy level available on the measurement day.

Since the measurement time depends strongly on the range of 2θ angle scanned, it is preferable to concentrated only on the few θ degrees where the peak is expected to be located. The 2θ angle is determined by the crystal lattice chosen. Each crystal lattice has a different deformation mechanism, influencing both the elastic and inelastic response. As reported above ??, in the literature are usually reported some preferential planes in relation to the sample material under investigation. Moreover for aluminum alloys lattice planes which can be used as a reference are:

- {311}
- {222}
- {333}
- {511}
- {422}

7.1. X-RAY DIFFRACTION MEASUREMENTS BY XRD

The choice of the lattice plane depends on the material itself but also on the subsequent test that particular component will be further subjected to; this because X-Ray diffraction measurement technique is non destructive.

For example, being the components under investigation in this work of thesis devoted to subsequent fatigue life, plane $\{422\}$ could be a choice; anyway, after analyzing the peak, it has been preferred to use plane $\{311\}$, which is commonly taken as a reference for aluminum 2024-T351.

as above mentioned, the grain size affects the precision of the measurement, since the coarser the grains, the less grains contributing to the diffraction peak. The more grains present in the measurement volume, the better the acquired signal.

It is important to know the time duration of each measurement since the beam-line has to work 24 hours per day in the assigned test interval; so a measurement schedule concentrating the coupon to be measured at the same energy level has to be provided. The time duration of each measurement depends on:

- wavelength or energy level provided
- measurement apparatus precision, in terms of detector sensitivity
- characteristics of the material under investigation, such as grain size and choice of the crystallographic plane for identification of the peak

Varying the ϕ orientation allows to measure different stress components.

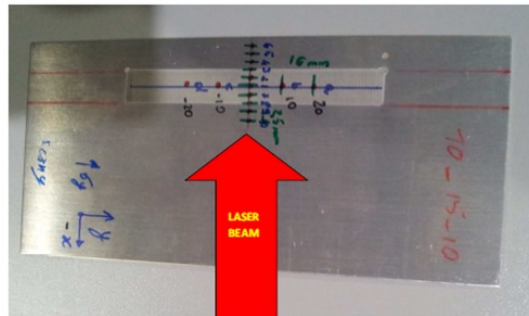


Figure 7.2: Residual Stresses measured are perpendicular to the hitting X-Ray beam

The residual stress measured are always perpendicular to the X-Ray beam direction as in ???. At least five tilt angles have to be selected to have reliable results in term of $\sin^2\psi$ values.

A particular procedure has to be applied when measuring at Elettra MCX Beamline, involving the following four phases:

- opening an closing in a safety way the experimental lab, where the measurement take place and the beam is acting
- properly fixing the sample without altering the residual stress field or having interactions of the grippers with the laser beam

7.1. X-RAY DIFFRACTION EXPERIMENTAL MEASUREMENTS BY XRD

- finding and setting the zero position
- starting the measurement

The specimen alignment has to be checked moving the coupon several times along the x and y axes several mm (i.e. 20 mm). Once the alignment is achieved, the phi angle must be zeroed. The specimen alignment is conducted from an outside area, close to the room where the laser beam hits the coupon, working on a PC on which the images of the specimen position in relation to the x and y axes, are provided from an inside camera. The alignment of the target is done by means of a provided software. After the axes alignment, the 2θ position has to be zeroed. The zero 2θ corresponds to that depicted in the following picture, ??:

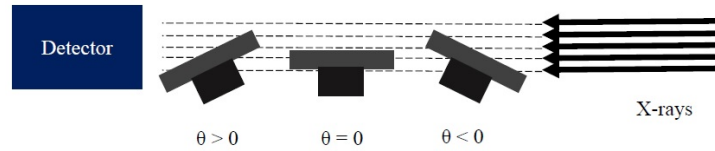


Figure 7.3: Finding the zero θ position

When looking for the zero θ position, the sample has to be also moved in the z direction in order to not obstruct the hitting X-Ray beam, and as a consequence the detector receives maximum intensity rays. During this phase of sample positioning and alignment, filters must be used, otherwise the detector which is exposed to the direct unattenuated X-Ray beam, risks to be damaged.

When inserting the sample in the sample holder, attention must be paid when closing the bolts to fix the sample; this operation has to be done without altering the residual stress field acting on the sample, and this is particularly difficult for coupons whose surface is a bit curved. Another aspect to take into account while positioning the sample is to ensure that the bolts do not interfere with the X-Ray beam at any of the ϕ angles measured. The 2θ angle is useful to determine the peak location. The XRD data provide the intensity counts per second, corresponding to the 2θ angle as in ??:

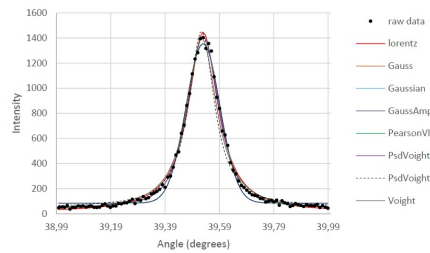


Figure 7.4: Peak Location

The peak can be determined by mathematical functions such as Gaussian, Lorentzian, Pearson VII, Voigt, and Pseudo-Voigt.

Sources of uncertainty in residual stress measurement by means of X-Ray are:

7.1. X-RAY DIFFRACTION MEASUREMENTS BY XRD

- specimen surface height offset; roughness peak on the surface can make it difficult to properly set the zero z position
- 2θ definition
- number of ψ tilts
- peak fitting method
- elastic constants chosen for the specimen material
- Coarse grain size

A problem connected with X-Ray measurements is that if the beam hits a coupon area which is too big, the residual stress measurements are no longer reliable, since while part of the hitting beam is still inside the target an other one is going out from it. Asking to Elettra staff, they ensured that this wasn't the case for tested coupon since it is possible to incur in such a risk only when dealing with more powerful synchrotron, but this is not the case for Elettra.

Different crystallographic planes give different elastic and inelastic responses. Measurements made on different crystallographic planes are not comparable. Also stress measurement made at different energy levels are not comparable since each energy level correspond to a different depth in the coupon thickness.

Before proceeding with any measurement it is recommended to clean or degrease the component surface without brushing it or treat it with abrasive chemical agents, since these can alter the residual stress field. If the sample is too big to access the facility and must be cut, this process has to be done without modifying the residual stress state, both cutting far from the area which is going to be measured and may be using electro discharge machining so to not introduce significant residual stresses. While cutting the sample attention must be paid to not heat the component.

If the specimen surface is curved, may be following a mechanical treatment, using a small X-Ray beam in relation to the target curvature, makes the X-Ray beam hitting a flat surface.

Rough surfaces can be measured as well even if attention must be paid to the z zeroing, since it can be affected from the higher peaks only acting as a reference thus not giving reliable estimation of the residual stress field characterizing the component.

The temperature must be kept constant during measurements since a change in this parameter can alter the residual stress field.

The first important step to perform when dealing with X-Ray diffraction measurement technique is to properly position the sample; only the residual stress component perpendicular to the laser beam can be measured .

An important step in the measurement procedure is the goniometer alignment. If during the measurement the sample needs to be translated to select different measurement points on its surface, or needs to be rotated by ϕ angle to select different stress components, it has to be checked that while doing so, the height of the sample in respect to the hitting X-ray beam is not changed; this is ensured by the correct alignment of the goniometer. χ tilt has to be verified as well to ensure that when changing the ψ angle there is no movement of the diffracted peak. Since height misalignment result in a shift of the diffracted peak, alignment has to be checked especially for curved surfaces, as one of that

7.1. X-RAY DIFFRACTION MEASUREMENTS BY XRD

reported below, regarding a laser peened coupon with laser pattern width of 20 mm. The alignment of this target has been checked moving several times and by several millimeters (20 mm) the coupon along both axes x and y, ensuring to precisely follow the axes references.

The coupon alignment is done by means of a provided software from a PC located outside the measurement room where the X-Ray beam acts ??:

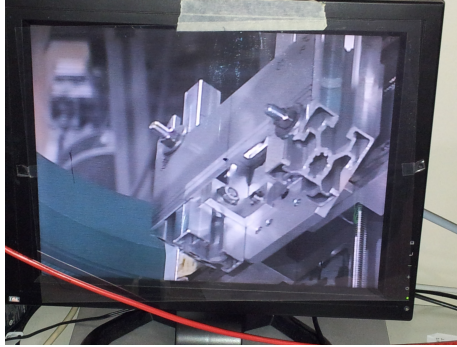


Figure 7.5: Coupon alignment

Pictures ?? and ?? show the coupon fixed in the measurement location:

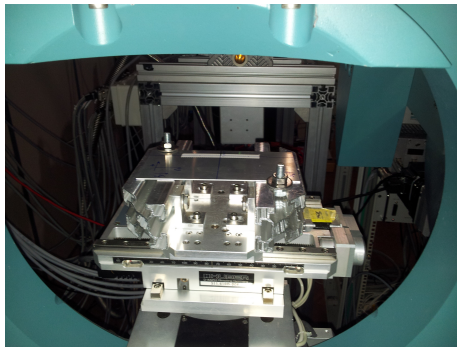


Figure 7.6: Coupon in measurement location, 1

Elettra facility is located in Basovizza, Trieste, accessible by walking through a park, as reported in ??:

Elettra synchrotron is shown in ??:

Picture ?? shows the the coupon alignment and close to it, the sharp diffracted peak obtained for further residual stress measurement; the small window in front shows an insight to the room where the coupon is placed and where the X-Ray beam is acting.

The target has to be properly fixed in the measurement location paying attention to not introduce further stress components while fixing it by bolts ??, ??:

7.1. X-RAY DIFFRACTION EXPERIMENTAL TECHNIQUES BY XRD

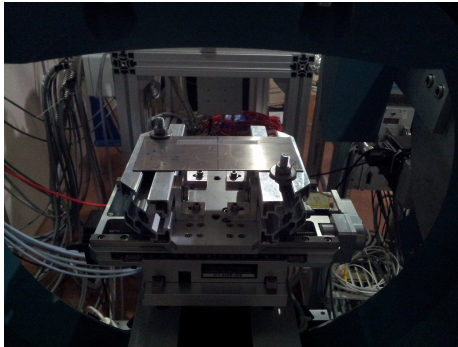


Figure 7.7: coupon in measurement location, 2



Figure 7.8: Elettra in Basovizza

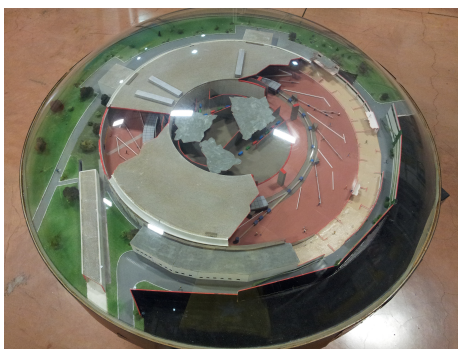


Figure 7.9: Elettra Synchrotron

7.1. X-RAY DIFFRACTION EXPERIMENTAL TECHNIQUES BY XRD

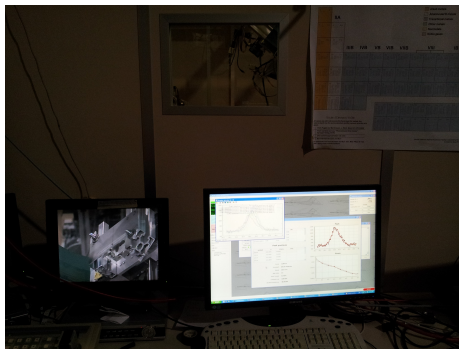


Figure 7.10: Elettra, residual stress measurement beam

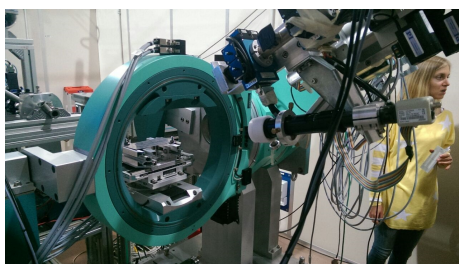


Figure 7.11: fixing the coupon



Figure 7.12: fixing the coupon, 2

7.2 Comparison between different laser set up parameters

The data coming from the Elettra experimental measurement test campaign are reported below in order to find the best laser set up parameters to be subsequently used for prediction of components fatigue life by a previously validated model. The week during which the test were carried out at Elettra facilities, the synchrotron energy level was 2 GeV, this meant the maximum energy available at residual stress measurement beam was 20 KeV. Nevertheless the Elettra technicians told reliable measurements could be taken at a maximum of 18 KeV. 18 KeV correspond to a depth in the coupon thickness of 0.012 mm.

Chi angles values to be measured are between 6 and 12 since the strain components to be used to evaluate the stress state are at least 6.

In each of the following measures the first point measured is that at the center of the shot pattern, and the others are at 2.5 mm from this first one moving towards the specimen center and after to the coupon edge, as depicted on the target in ??.

X-Ray measurement technique is based on Bragg's Law.

There is a relationship between the diffraction pattern diffracted from the crystal lattices after being hit from the X-ray beam and the distance between the lattices, which are representative of the residual stress field achieved. Altering the inter-planar distance between lattices causes a different diffraction pattern. Changes in the diffracted pattern are also affected by different X-ray beam wavelength.

A question mark linked to X-Ray measurement technique is related to the fact that since some materials strongly absorb X-Ray, only a small thickness under the coupon surface can be reached, thus making it not possible to precisely predict the thickness to which correspond the measured residual stress.

Referring to ??, the main angles involved in residual stress measurement by means of X-ray diffraction technique are:

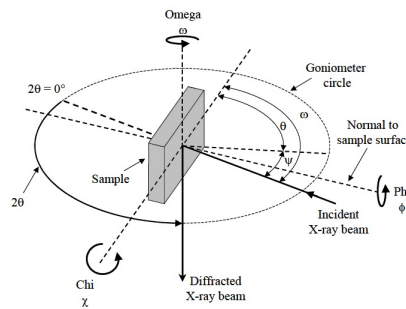


Figure 7.13: Angles involved in X-Ray measurements

- 2θ angle is the Bragg angle, the angle between the incident and diffracted X-Ray beam
- Omega ω is the angle between the incident X-ray beam and the sample surface. Omega and 2θ lie in the same plane

7.2. COMPARISON BETWEEN DIFFERENT LASER SET UP PARAMETERS

CHAPTER 7. EXPERIMENTAL RES MEASUREMENTS BY XRD

- ϕ is the angle of rotation of the sample about its surface normal
- χ is the angle of rotation in plane defined by ω and 2θ .
- ψ is the angle involved in the $\sin^2\psi$ method. Start at $\psi=0$ where ω is half of the 2θ and add successive ψ , i.e. 20, 30 and 40 °.

The working principle of an X-Ray tube can be summarized in a focused beam of electrons which is accelerated through a large potential difference (energy supplied by an external generator) and strikes a metal target with considerable energy, resulting in the generation of X-Rays. Anyway, most of the involved energy is dissipated into heat and only 2% is converted in X-Rays.

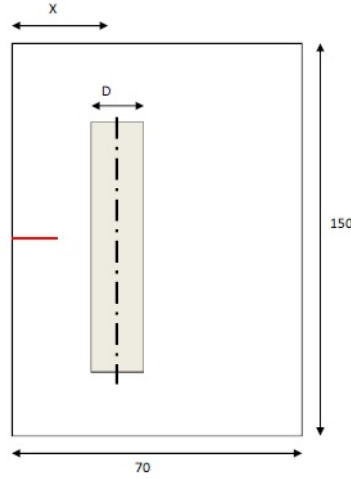


Figure 7.14: Specimen Configuration

Point Test#	Plasier Stress [Mpa]															
	1	21	10	9	8	7	1	2	3	4	5	6	15	17.5	a	b
20	-12.5	-10	-7.5	-5	-2.5	0	2.5	5	7.5	10	12.5	15	17.5	20	10	0
21	36.47	7.34	20.63	64.93	-138.9	-129.54	-122.03	-25.69	36.05	31.99	31.96				-131.48	-129.54
22						-79.8	-76.33	-20	23.66	22	22					
23						-49.82	-55.1	-30	-12.76	7	-1					
24						-127.8	-130.56	-50	34.98	30	30					
						-105.63	-101.08	-40	19.66	18	18					

Figure 7.15: Residual Stress Summary at 12 KeV

Picture ?? shows that 2.0 and 2.5 $\frac{GW}{cm^2}$ give the same compressive residual stress field, whereas decreasing the laser power with the same coverage result in a lower in magnitude compressive residual stress. An increase in laser power decreasing the coverage, result in a more lower compressive residual stress.

Picture ?? shows that the largest the laser pattern, and the closer to the edge, the lower the compressive residual stress field. Double side peening provides the higher compressive residual stress field. The same laser pattern width and laser parameters result in a higher compressive residual stress for laser pattern closer to the edge.

Picture ?? shows that specimens laser peened with the same coverage and laser parameters except from the laser power exhibit a higher compressive residual stress in case of higher laser power. At this depth (measurement depth defined

7.2. COMPARISON BETWEEN DIFFERENT LASER SET UP

PARAMETER 7. EXPERIMENTAL RS MEASUREMENTS BY XRD

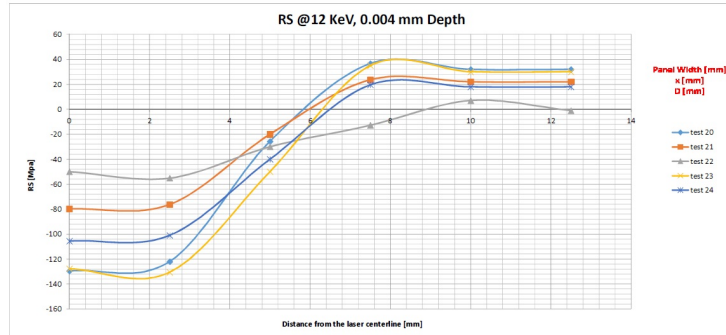


Figure 7.16: Residual Stress Plot at 12 KeV

Point	Plaser Stress [Mpa]																
	20	11	10	9	8	7	1	2	3	4	5	6	12.5	15	17.5	a	b
Test # / X co-ord	0	-12.5	-10	-7.5	-5	-2.5	0	2.5	5	7.5	10	12.5	15	17.5	20	10	0
1																	
2	-172	10.46	10.84	13.84	-129.4	-162.55	-159.5	-158	-14.48	30.59	25.28	44.53				-166.62	-163.83
3																	
4																	
5																	
6																	
7																	
8																	
9																	
10																	
11																	
12																	
13																	
14																	

Figure 7.17: Residual stress Summary at 15 KeV

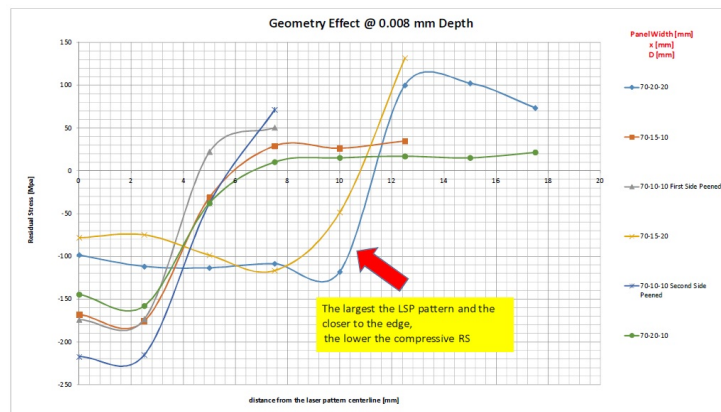


Figure 7.18: residual stress Plot at 15 KeV

Point	Plaser Stress [Mpa]																
	1	11	10	9	8	7	1	2	3	4	5	6	12.5	15	17.5	a	b
Test #	12.5	-10	-7.5	-5	-2.5	0	2.5	5	7.5	10	12.5	15	17.5	20	10	0	-10
15																	
16	16.9	19.04	12.23	-139.25	-160.5	-160.99	-148.62	7	41.06	33.04	31.85					-164.24	-156.92
17																	
18																	
19																	
20																	

Figure 7.19: Residual Stress Summary at 18 KeV

7.2. COMPARISON BETWEEN DIFFERENT LASER SET UP PARAMETERS

CHAPTER 7. EXPERIMENTAL RS MEASUREMENTS BY XRD

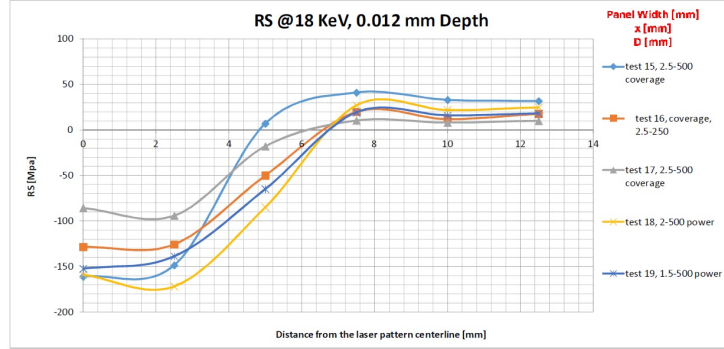


Figure 7.20: Residual Stress plot at 18 KeV

by this energy level, 18 KeV) under the coupon surface, a higher compressive residual stress can be seen for coupon with the same laser power but less coverage.

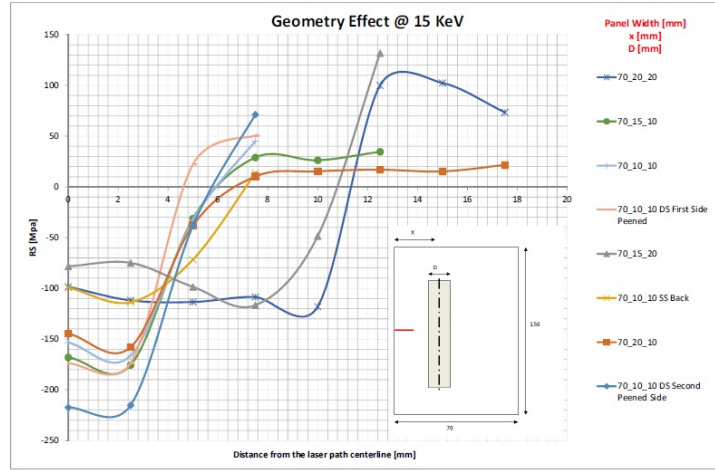


Figure 7.21: Laser Geometry Effect, 15 KeV

Picture ?? shows that double side peening configuration provides the higher compressive residual stress. Configurations shot with the same laser parameters and having the same laser pattern width, are very close to each other when varying only the laser pattern distance from the coupon edge. Measurement carried out on a coupon shot peened on only one side but measured on both surfaces, shot and not, showed the higher compressive residual stress on the shot side in respect to the non shot one. Enlarging the laser pattern width but maintaining the same laser parameters result in a lower compressive residual stress; anyway, in this case, the configuration exhibiting the laser pattern farther from the coupon edge is characterized by the higher compressive residual stress.

Picture ?? show that the results are very close to each other, but coupons with the same laser parameters and same laser pattern width exhibited the higher compressive residual stress for laser pattern farther from the target edge.

Picture ?? shows that samples characterized by the same laser parameters

7.2. COMPARISON BETWEEN DIFFERENT LASER SET UP PARAMETERS

CHAPTER 7. EXPERIMENTAL RS MEASUREMENTS BY XRD

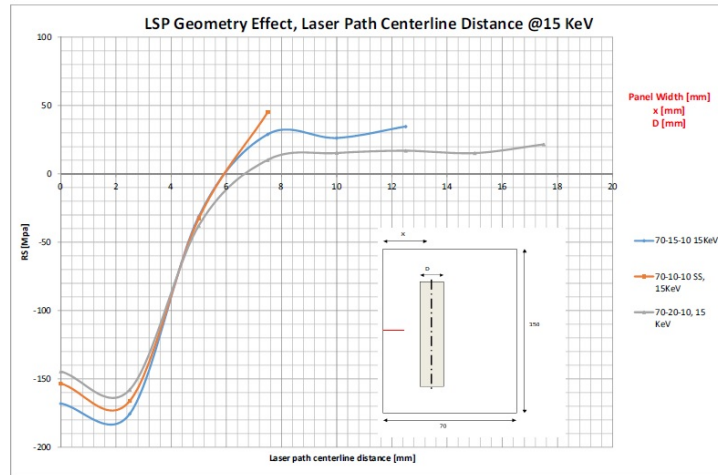


Figure 7.22: Laser Pattern Distance from Edge Effect, 15 KeV

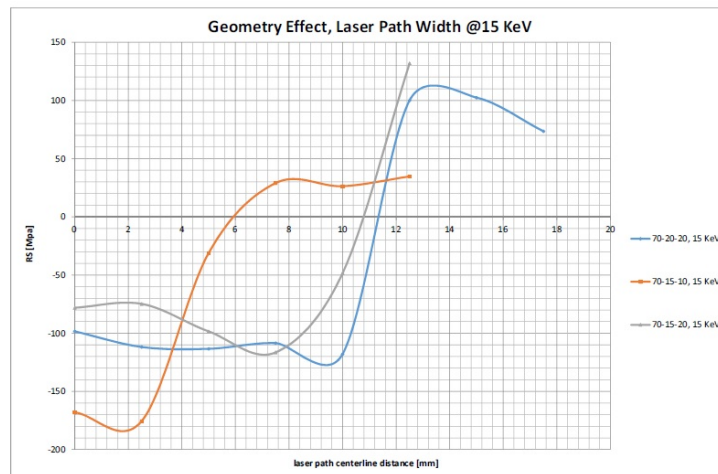


Figure 7.23: Laser Pattern Width Effect, 15 KeV

7.2. COMPARISON BETWEEN DIFFERENT LASER SET UP PARAMETERS

CHAPTER 7. EXPERIMENTAL RS MEASUREMENTS BY XRD

and distance from edge, exhibit the higher compressive residual stress for smaller laser pattern width.

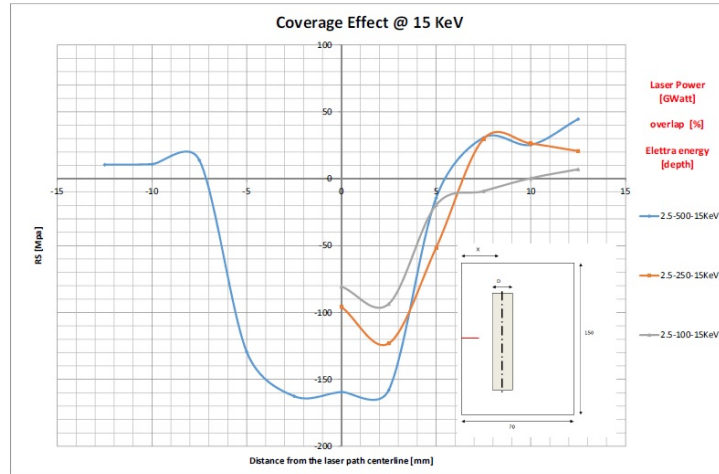


Figure 7.24: Coverage Effect, 15 KeV

Picture ?? shows that at 15 KeV, coupons characterized by the same laser parameters and power density, reached a higher compressive residual stress for the higher coverage.

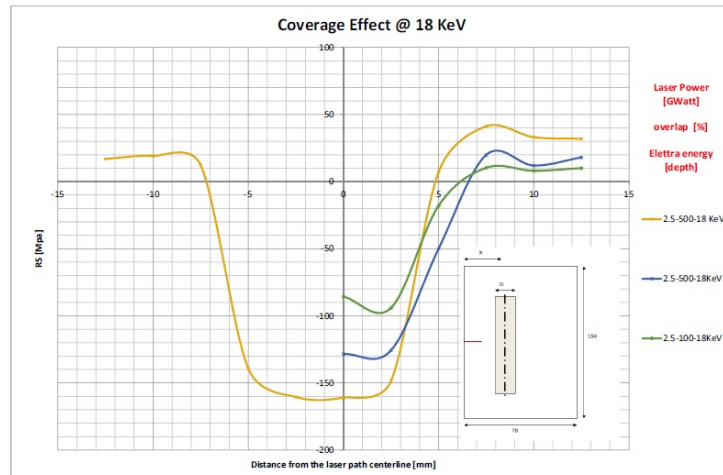


Figure 7.25: Coverage Effect, 18 KeV

Picture ?? analyzes the effect of the coverage parameter at 18 KeV energy level. Even at this coupon depth, at the same laser power, the higher compressive residual stress is associated with the higher coverage percentage.

In picture ?? all the results are close to each other. Nevertheless, coupon characterized by the same coverage percentage, showed the higher compressive residual stress for higher laser power used.

Also picture ??, showing residual stresses achieved at 18 KeV as energy level,

7.2. COMPARISON BETWEEN DIFFERENT LASER SET UP PARAMETERS

CHAPTER 7. EXPERIMENTAL RS MEASUREMENTS BY XRD

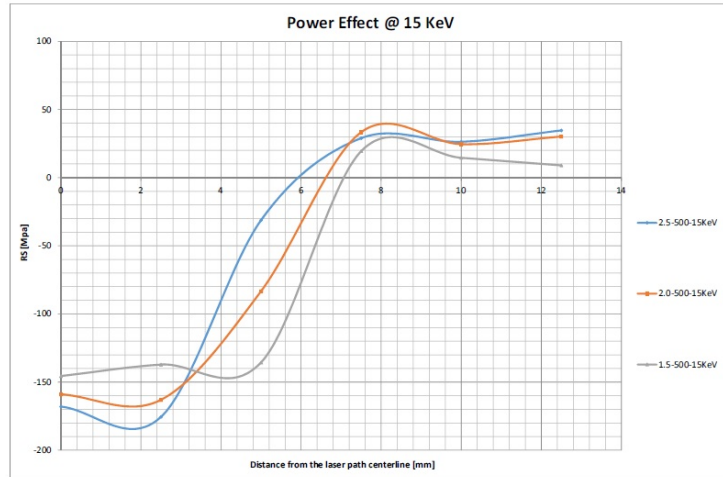


Figure 7.26: Laser power Effect, 15 KeV

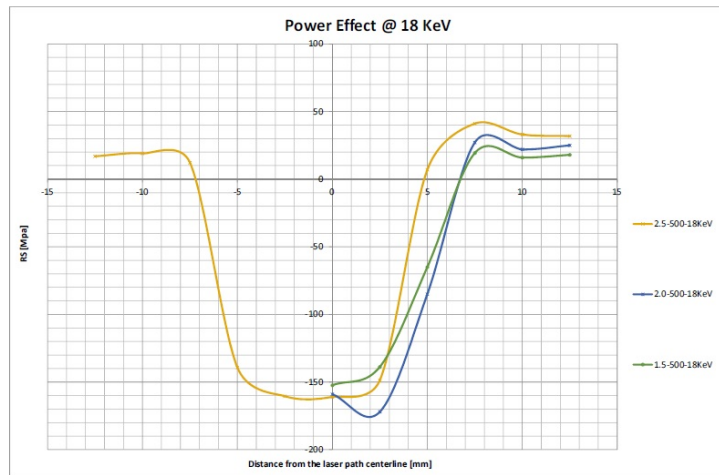


Figure 7.27: Laser Power Effect, 18 KeV

7.2. COMPARISON BETWEEN DIFFERENT LASER SET UP PARAMETERS

CHAPTER 7. EXPERIMENTAL RS MEASUREMENTS BY XRD

highlights that the results are very close to each other, namely the same, at this depth under the coupon surface.

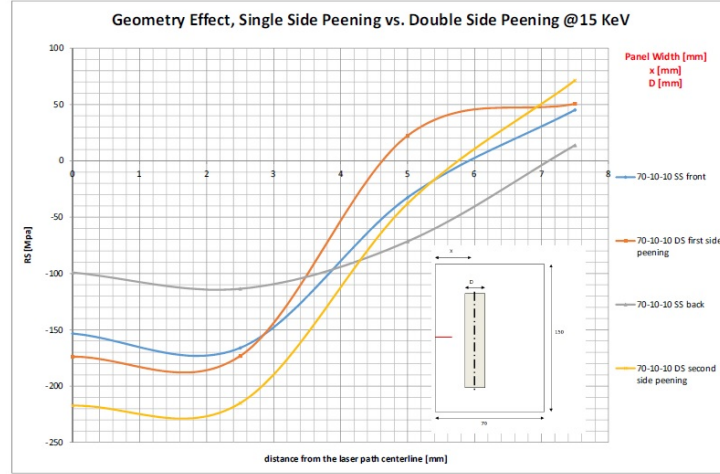


Figure 7.28: Single Side Shot vs Double Side Shot Configuration, 15 KeV

Picture ?? shows that double side shot coupon are characterized by the higher compressive residual stress field, when compared to the same parameters used on a single side shot specimen.

As can be seen in ??, on the first side peening the residual stress reaches a maximum in compression of -170 Mpa, while on the second side peening a value of -230 MPa is reached, and this in accordance with the fact that after the first side shot, the specimen shot surface curvature is concave, whereas the second one is convex. In order to reduce the coupon curvature, the Witwatersrand University performs laser peening with different parameters in respect to the first and second shot side; the laser power adopted for the first shot side is higher than that of the second one. Using this procedure it has been noted that after shooting the first side, the coupon shot surface comes convex; rotating the target on the other side and shooting it with a lower laser power reduces the curvature caused as a consequence of the first side shot.

Looking at the single side shot coupon, the compressive residual stress achieved on the shot surface is higher than that measured from the not shot one.

Picture ?? shows the measurement points on the coupon laser peened at Witwatersrand University:

while, ?? and ?? show the measurement points on the UPM coupon, both on the front and back side:

Picture ?? shows the residual stress field achieved on two coupons characterized by same material and dimensions, but shot peened at University of Madrid (UPM) and Witwatersrand University (SA). The specimen shot peened in Madrid is characterized by two laser peened pattern whereas that shot peened at Witwatersrand University shows just one laser pattern; anyway, the distance between the laser path and the coupon edge is the same for both configurations, 15 mm. Both the coupons have been laser peened on both sides. Regarding the specimen shot peened in Madrid, nor laser power nor coverage percentage are known. To properly compare the achieved results, knowledge of the above mentioned

7.2. COMPARISON BETWEEN DIFFERENT LASER SET UP
 CHAPTER 7. EXPERIMENTAL RS MEASUREMENTS BY XRD

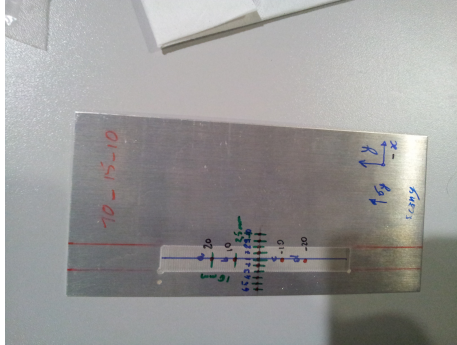


Figure 7.29: measurement points on WITS coupon

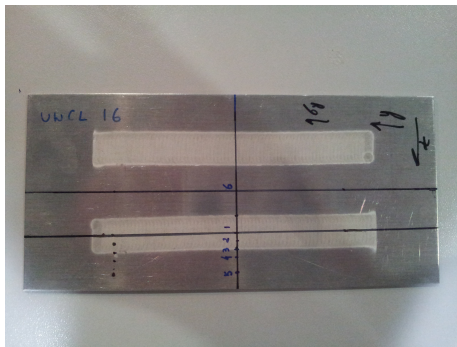


Figure 7.30: measurements points on UPM coupon, front side

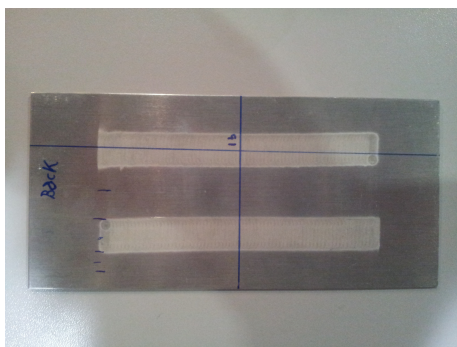


Figure 7.31: measurement point on the UPM coupon, back side

7.2. COMPARISON BETWEEN DIFFERENT LASER SET UP

CHAPTER 7. EXPERIMENTAL RS MEASUREMENTS BY XRD

UPM	15	0	3	6	9	14.5
Side 1	-2.67	-129.1	-121.2	8.81	16.22	18.9
Side 2		-111.4				

WITS 70-10-10	0	2.5	5	7.5
Side 1	-173.94	-173.32	22.32	50.57
Side 2	-217.32	-215.14	-37.99	71.34

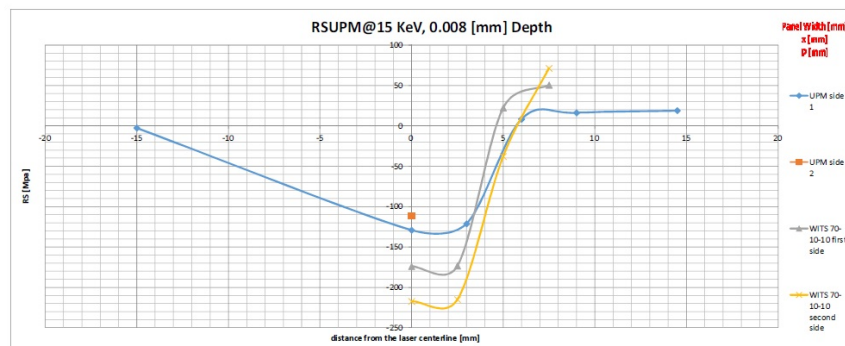
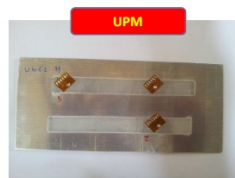


Figure 7.32: Residual Stress achieved at UPM vs Residual Stress achieved at WITS, 15 KeV

7.2. COMPARISON BETWEEN DIFFERENT LASER SET UP
PARAMETERS

CHAPTER 7. EXPERIMENTAL RS MEASUREMENTS BY XRD

parameters is requested; but looking at the residual stress field achieved, the specimen shot peened at Witwatersrand University, shows the higher compressive residual stresses and confirms the trend showing higher compressive residual stress on the second side peened surface. Coupon shot peened in Madrid shows lower compressive residual stresses and the opposite behavior in respect to the Witwatersrand one, exhibiting higher compressive residual stresses on the first side peening. This last point plus the curvature of the target, make the author think that at UPM, the coupon has been shot peened on both sides with the same laser parameters. The specimen shot peened at Witwatersrand University show less curvature, but to achieve this result, different laser set up parameters are used when shooting the coupon on first and second side.

Bibliography

- [1] Paul S. Prevey. *X-Ray Diffraction Residual Stress Technique* Lambda Research, Inc.
- [2] D. Glaser. *MSc Thesis*, Witwatersrand University, March 2014.
- [3] M.E.Fitzpatrick, A.T.Fry, P.Holdway, F.A.Kandil, J.Shackleton and L.Suominen. *Measurement Good Practice Guide No.52, Determination of Residual Stress by X-Ray Diffraction - Issue 2*, September 2005.

CHAPTER 8

Analytical Fatigue Predictions

The analytical prediction of crack growth in thin specimens, based on Terada model, has been carried out with the residual stresses measured at Elettra. The different LSP configurations tested for energy level 12KeV, corresponding to 0.004 mm depth, through the thickness direction are reported in ??:

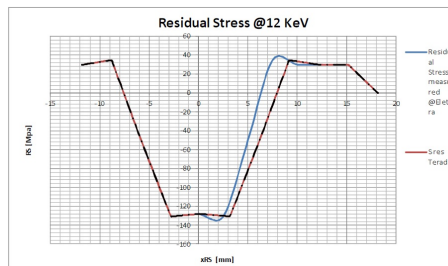


Figure 8.1: LSP configurations tested at 12KeV, 0.004 mm depth, thickness

In this figure is reported the shot configuration followed by a summary of the residual stress field achieved by each coupon tested at this energy level ??, ??:

From the results achieved at Elettra it is highlighted that there is no equilibrium between the tensile and compressive residual stresses inserted in the coupon after the LSP treatment; the tensile and compressive residual stress achieved are not balancing, in the thickness portion analyzed by the this energy level.

To not be long winded, only the results connected to the configuration which seemed to give rise to the best and worst performance in terms of fatigue life are reported below in detail.

Calculation made with the Elettra unbalanced results show an increase in the component fatigue life which is estimated in the 261.66%, while, forcing an equilibrium distribution of tensile and compressive residual stresses by the summation of 24 MPa, a detrimental effect of the laser peening treatment can be quantified in the -24.12% of the component fatigue life.

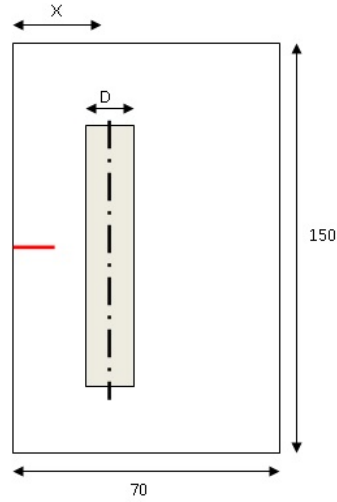


Figure 8.2: Edge Crack configuration

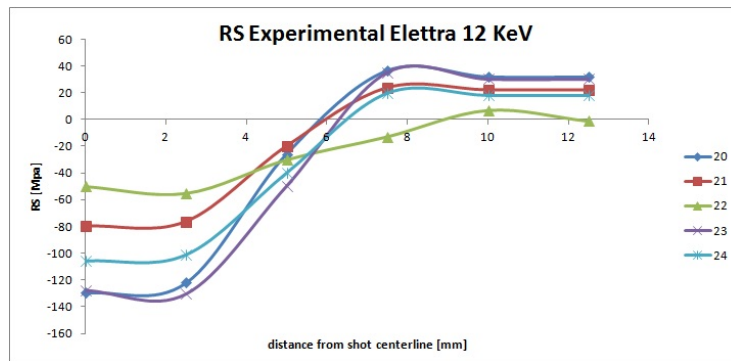


Figure 8.3: Residual Stress achieved by each LSP configuration tested at 12 KeV

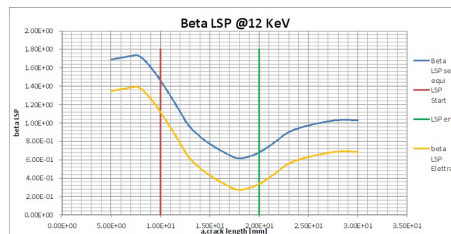


Figure 8.4: Beta Factor, configuration number 23, 12 KeV energy level

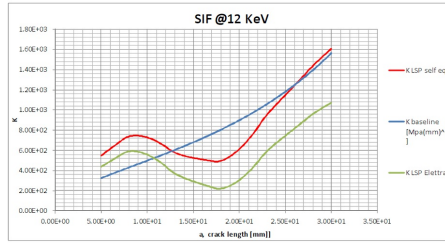


Figure 8.5: SIF, configuration 23, 12 KeV

From the pictures reported above, ??, ??, and correspondent to the beta factor and the stress intensity factor, it can be easily noticed that the curve representative of the Elettra experimental data, result in an increase of the component fatigue life, while that referring to the residual stress balanced solution, being always above the previously mentioned one, result in a faster FCP.

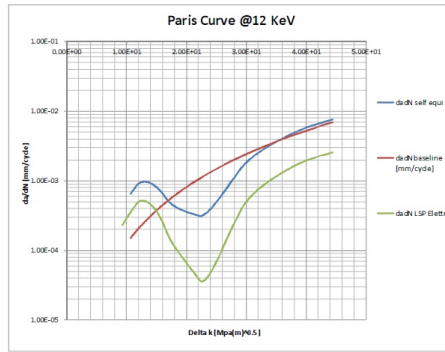


Figure 8.6: Paris Curve, configuration 23, 12 KeV

Looking at the Paris curve, ??, an increase in fatigue life is achieved when using the Elettra unbalanced residual stress field, since the curve is always above the baseline, while a detrimental effect is highlighted when using the balanced solution. The same trend is more evident when looking at the a - N curve, ??;

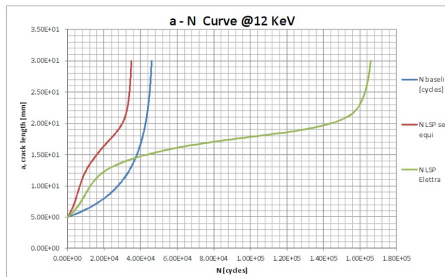


Figure 8.7: a N Curve, configuration 23, 12 KeV

Here, the number of cycles to fatigue is less than the baseline for the balanced

solution, while a steep increase is achieved when using the real residual stress distribution, measured at Elettra.

The number of cycles to fatigue for the half crack length to go from 5 to 30 mm is:

- **45898 cycles for the baseline**
- **34828 cycles for the forced balanced solution**
- **165996 cycles relative to the Elettra residual stress measurements**

The unbalanced residual stress field achieved can be due to the specimen geometry, $150 * 70 * 1.4$ mm, which can be too small to guarantee the recovery of the equilibrium, being the shot pattern close to the coupon edge; or to the reached thickness by the provided energy level.

The worst solution in terms of fatigue life is that of coupon 21. The effect of the laser treatment is a benefit of only the 12.7% in respect to the baseline, whereas the detrimental effect achieved when using the balanced residual stress field is of -28.77%. As can be seen in ??, the difference with the above mentioned best solution, is not in term of laser pattern geometry, since the the distance from the edge of the laser path, as well as its width are the same, but the laser parameters. The different laser set up can be summarized as follows ??, and ??:

- best solution:

Laser Power [GW/cm ²]	Overlap percentage
2.0	500

Table 8.1: Coupon 23 Laser Set up Parameters

- worst solution:

Laser Power [GW/cm ²]	Overlap percentage
2.5	250

Table 8.2: Coupon 21 Laser Set up Parameters

The fatigue plots reported below, ??, ??, ??, ?? and ?? are referred to the introduction in the prediction model of the residual stress field achieved at Elettra plus 11 MPa in order to reach the equilibrium state between the tensile and compressive stresses. Picture ??:

Picture ?? shows the beta trend for both the residual stress field as measured at Elettra, and that achieved by forcing a balanced solution between compressive and tensile stresses. The picture shows that the curve referring to the balanced residual stresses is above that coming from Elettra measurements, thus leading to a worst performance in terms of fatigue life.

Looking at the SIF curve depicted in ??, the curve coming from Elettra measurements is below the baseline, showing a possible improvement in terms of fatigue life, whereas that coming from the balanced solution, forced to achieve

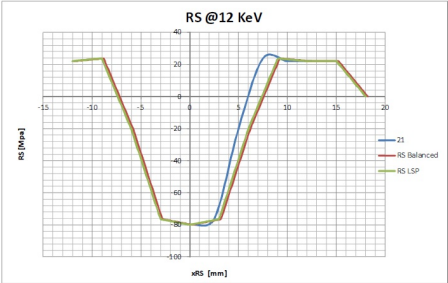


Figure 8.8: rs 21

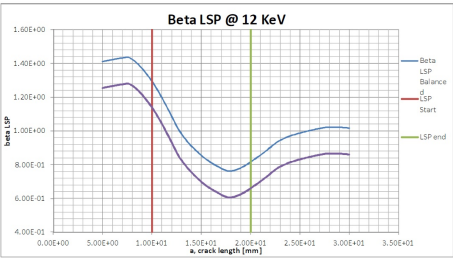


Figure 8.9: beta 21

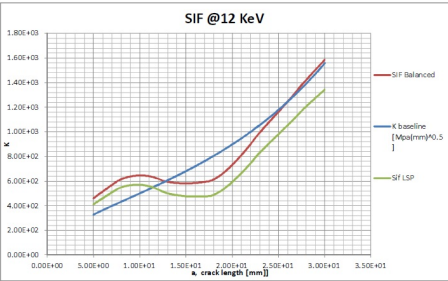


Figure 8.10: sif 21

equilibrium between compressive and tensile residual stresses, shows the typical decrease when reaching the laser pattern, but lies above the baseline when approaching the aside tensile residual stresses, thus showing a detrimental effect on fatigue life.

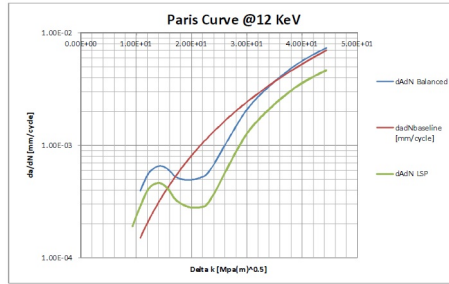


Figure 8.11: paris 21

The same trend can be seen in ?? showing a detrimental effect on fatigue life when moving from the Elettra measured residual stresses to that forced to reach an equilibrium solution between compressive and tensile RS.

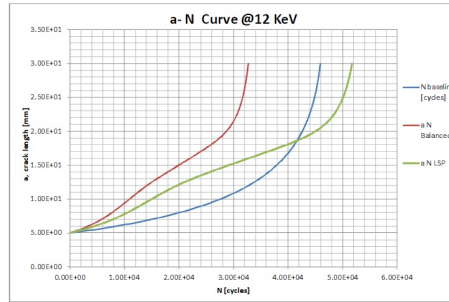


Figure 8.12: an 21

a - N curve, ??, confirms the above mentioned trend, thus, residual stresses measured at Elettra give an increase in terms of fatigue life, whereas the forced balanced solution results in a detrimental effect. This aspect can be summarized in the cycles to fatigue of the as measured and balanced solution giving:

- baseline cycles = 45900
- Elettra RS cycles = 51800
- Balanced solution cycles = 32700

In the following pictures are reported the results achieved in terms of fatigue life prediction of coupon measured at 15 KeV as energy level, so to a major depth in coupon thickness in respect to the previously reported results.

Picture ?? shows the residual stress field achieved at Elettra for coupon number 3, and that obtained by forcing an equilibrium solution between compressive and tensile residual stresses, achieved by adding 40 MPa to the measured ones.

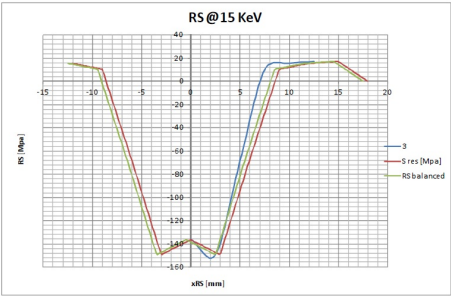


Figure 8.13: 3 rs

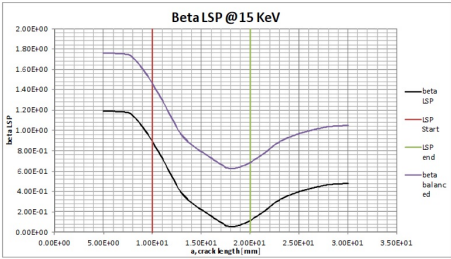


Figure 8.14: beta 3

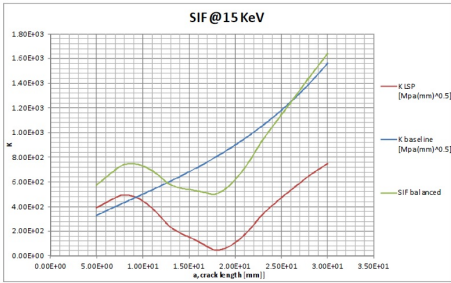


Figure 8.15: sif 3

As can be seen in ??, beta balanced parameter is always above the curve referring to the measured values of residual stress.

Picture ?? shows that the SIF curve referred to the RS measured at Elettra is always below the baseline, thus showing a beneficial effect in terms of fatigue life; whereas when forcing the equilibrium solution between compressive and tensile RS, the SIF curve shows the typical beneficial effect when approaching the shot pattern, but goes above the baseline when reaching the aside tensile residual stress state, thus showing a faster FCP.

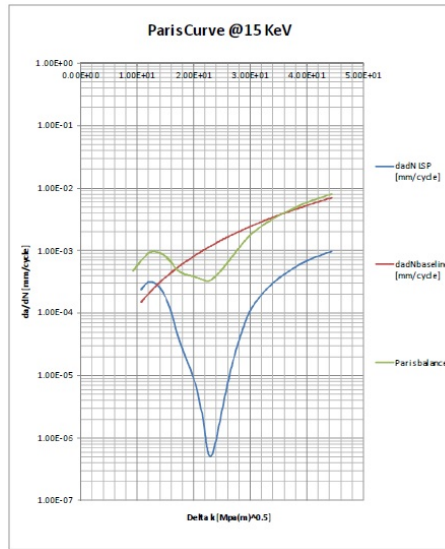


Figure 8.16: 3 paris

Picture ?? shows the Paris Curve for coupon number 3. Also in this case the curve resulting from the residual stresses measured at Elettra is always below the baseline, thus showing a benefit in terms of fatigue life. The forced balanced solution, results instead in a decrease in fatigue life performances, since after going below the baseline when approaching the compressive residual stress field in correspondence to the laser pattern, goes again above it, thus showing a faster FCP.

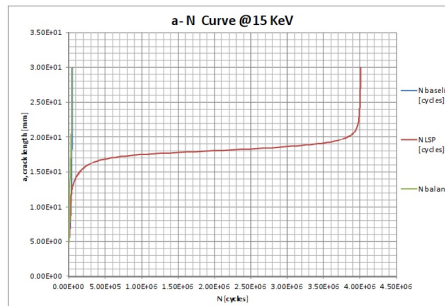


Figure 8.17: 3 an all

Since a big difference in terms of cycles to fatigue has been highlighted for this configuration, different $a - N$ curves have been reported to compare the various solutions. Figure ?? shows a big increase in terms of fatigue life, estimated via the residual stresses measured at Elettra, whereas the balanced solution, reported in ?? shows a detrimental effect in terms of fatigue life. This can be summarized in the following:

- baseline cycles = 45900
- Elettra RS cycles = 4000000
- Balanced solution cycles = 33800

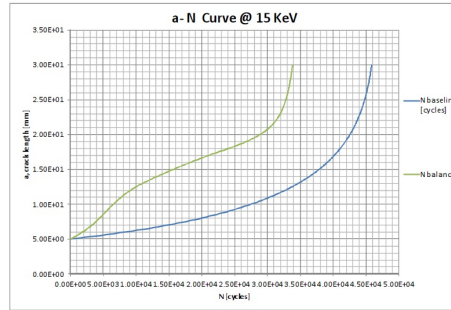


Figure 8.18: 3 an part

Up to now, results referred to coupon number 3 have been reported; specimen 3 has been measured at 15 KeV as energy level. This target has proved to be the best one in terms of fatigue life in respect to the other coupons measured at this same energy level. Now, results referred to coupon 11 are going to be investigated. Coupon 11 proved to be the worst one in terms of fatigue life, referring to the other coupons measured at 15 KeV. The differences between the two configurations are summarized in the following tables, ?? and ??:

- best solution:

Coupon Number	Laser Parameters [GW/cm ²], overlap percentage	geometry Configuration
3	2.5-500	70-15-10

Table 8.3: Coupon 3 Laser Set up Parameters

- worst solution:

Picture ??, shows the residual stresses obtained for coupon number 11 at Elettra facility, compared with that coming from Terada modeling method and that superimposed forcing a balance solution between tensile and compressive residual stresses, by adding 40 MPa to the measured values.

?? also in this case, the trend is confirmed, with the beta curve generated by the balanced residual stresses above that coming from Elettra measurements.

CHAPTER 8. ANALYTICAL FATIGUE PREDICTIONS

Coupon Number	Laser Parameters [GW/cm ²], overlap percentage	geometry Configuration
11	2.5-500	70-20-20

Table 8.4: Coupon 11 Laser Set up Parameters

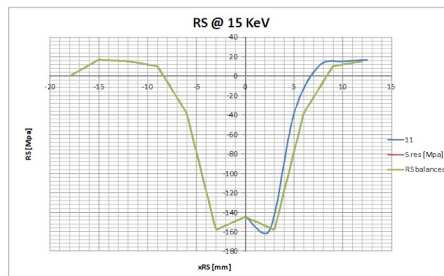


Figure 8.19: rs 11

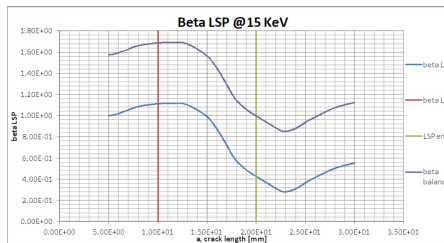


Figure 8.20: beta 11

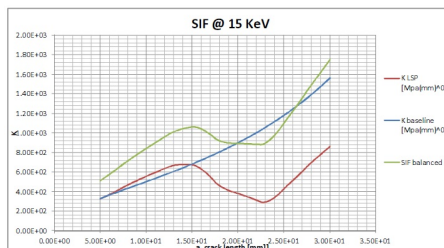


Figure 8.21: sif 11

Picture ?? shows the SIF trend; SIF curve obtained from Elettra measurements is below the baseline, showing an improvement in fatigue life, whereas that extrapolated from the balanced residual stress field is above the baseline implying an increase in FCP.

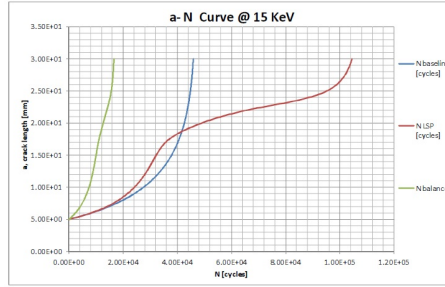


Figure 8.22: an 11

Picture ?? highlights the previously mentioned trend in terms of cycles to fatigue. Curve representing the data measured at Elettra shows an improvement in fatigue life which can be quantified in 127%, while that obtained from the balanced residual stress values results in a detrimental effect quantifiable in the -63.7 %. In terms of cycles to fatigue, this can be summarized as follows:

- **baseline cycles = 45900**
- **Elettra RS cycles = 104000**
- **Balanced solution cycles = 16700**

Picture ?? represents the residual stresses coming from Elettra measurements compared with that estimated by Terada model and that coming from a super-imposed equilibrium solution between compressive and tensile residual stresses reached by adding 38 MPa to the measured values.

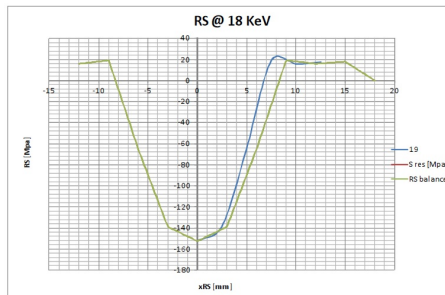


Figure 8.23: 19 rs

Picture ??, shows that even at depth reached by 18 KeV as energy level, the balanced curve is above that coming from Elettra measurements.

Picture ?? is referred to the SIF parameter, and also in this case a beneficial effect is obtained from Elettra measured residual stress, while a detrimental solution in terms of FCP is that achieved with the balanced RS field, which

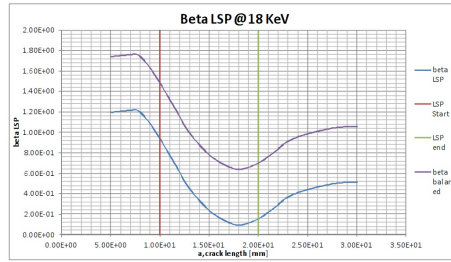


Figure 8.24: 19 beta

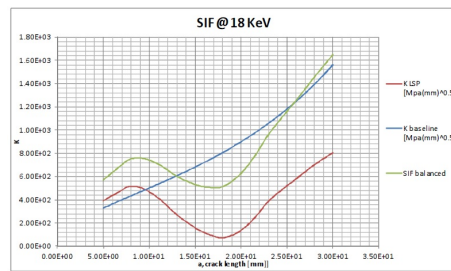


Figure 8.25: 19 sif

is above the baseline before and after the shot pattern border, this where the tensile RS is acting to restore equilibrium to the compressive state found in correspondence to the shot path.

Picture ??, shows the same trend as the SIF one. So, same considerations in terms of fatigue life can be carried out.

Picture ??, shows a great improvement in fatigue life in terms of cycles to fatigue of the data coming from Elettra measurements. To see the detrimental effect induced by the balanced solution an other plot is reported ??.

The beneficial and detrimental effect on the component fatigue life can be thus summarized:

- **baseline cycles = 45900**
- **Elettra RS cycles = 1590000**
- **Balanced solution cycles = 33400**

While coupon 19 resulted in fatigue life best performance in respect to the coupons tested at this same energy level, coupon 17 was the worst one; in fact, while coupon 19 resulted in a beneficial effect quantifiable in 3365 %, coupon 17 resulted in a benefit of only 90%. Reported in the tables ?? and ?? below, are the main differences between the two configurations:

- **best solution:**
- **worst solution:**

In ??, the balanced residual stress field has been obtained by adding 21 MPa to the RS field measured at Elettra.

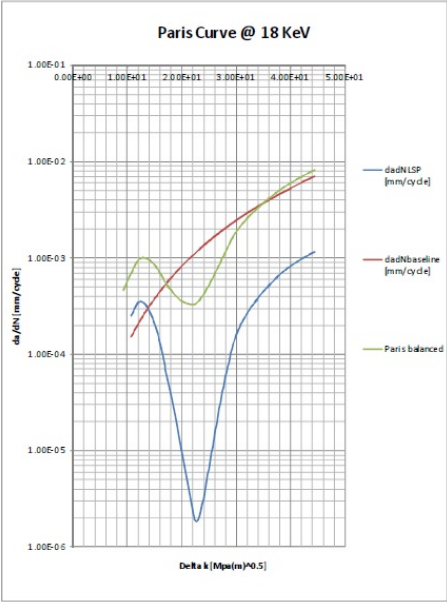


Figure 8.26: 19 paris

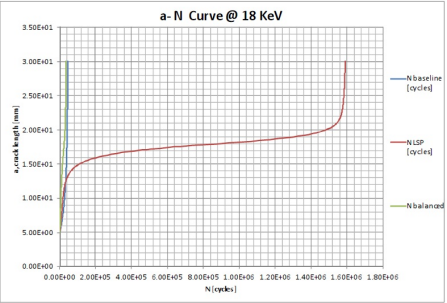


Figure 8.27: 19 an all

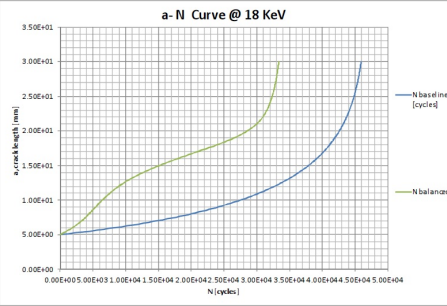


Figure 8.28: 19 an part

Coupon Number	Laser Parameters [GW/cm ²], overlap percentage	geometry Configuration
19	1.5-500	70-15-10

Table 8.5: Coupon 19 Laser Set up Parameters

Coupon Number	Laser Parameters [GW/cm ²], overlap percentage	geometry Configuration
17	2.5-100	70-15-10

Table 8.6: Coupon 17 Laser Set up Parameters

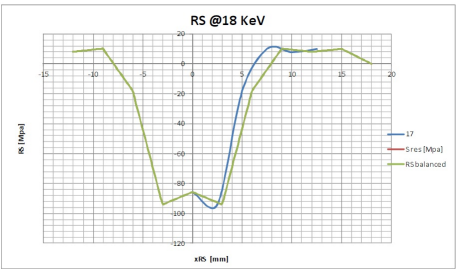


Figure 8.29: rs 17

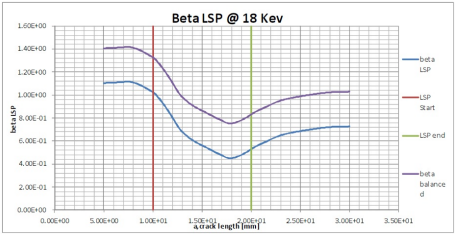


Figure 8.30: 17 beta

This case ??, as all the previous ones shows the beta curve obtained from the balanced solution above that coming from experimental measurements at Elettra, this leading to a detrimental effect in terms of fatigue life.

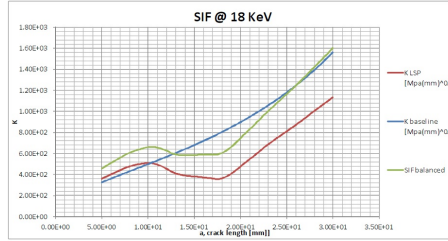


Figure 8.31: 17 sif

Picture ?? shows the beneficial effect of compressive residual stress in correspondence to the laser pattern, but while the RS field measured at Elettra leads to a beneficial effect in terms of fatigue life, with the correspondent curve below the baseline one, that coming from the balanced RS field shows a detrimental effect in terms of FCP.

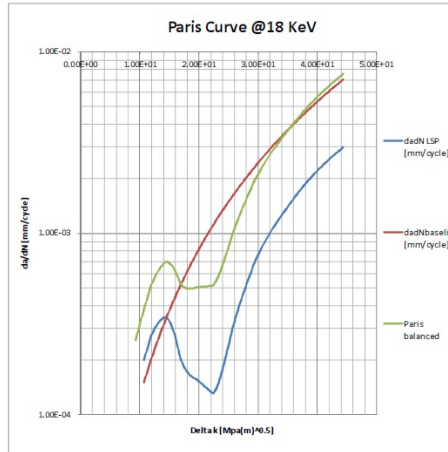


Figure 8.32: 17 paris

Same considerations can be obtained by Paris curve in ??.

Picture ?? shows beneficial and detrimental effects of the residual stress field analyzed in terms of cycles to fatigue. The trend can be summarized as follows:

- **baseline cycles = 45900**
- **Elettra RS cycles = 87100**
- **Balanced solution cycles = 32600**

From the reported results it has been further analyzed if a less compressive residual stress field, which gives rise to a less tensile residual stress magnitude, which is responsible for faster crack propagation, can result in a better performance in terms of fatigue life. Concern about this aspect is linked to the

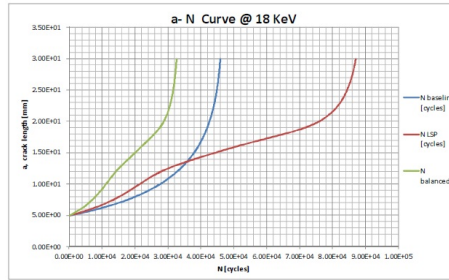


Figure 8.33: 17 an

chance that a lower compressive residual stress state can act as an obstacle to the approaching crack. On the opposite, a higher compressive residual stress field acts as a stronger crack growth opponent, but the tensile state acting aside the laser pattern, being higher, can accelerate the crack such that the further compressive RS can non longer slow down the crack propagation. This aspect is now analyzed more in detail in relation to the previously reported results.

At 12 KeV the achieved results are summarized in ??:

Coupon Number	Laser Parameters [GW/cm ²], overlap percentage	Geometry Configuration [mm]	Higher Compressive RS [MPa]	Cycles to Fatigue, Elettra	Cycles to Fatigue, balanced
23	2.0-500	70-15-10	-80	165996	34828
21	2.5-250	70-15-10	-131	51800	32700

Table 8.7: Comparison on fatigue performance between coupons 23 and 21, 12 KeV

At 15 KeV the achieved results are summarized in ??:

Coupon Number	Laser Parameters [GW/cm ²], overlap percentage	Geometry Configuration [mm]	Higher Compressive RS [MPa]	Cycles to Fatigue, Elettra	Cycles to Fatigue, balanced
3	2.5-500	70-15-10	-149	4000000	33800
11	2.5-500	70-20-10	-158	104000	16700

Table 8.8: Comparison on fatigue performance between coupons 3 and 11, 15 KeV

At 18 KeV the achieved results are summarized in ??:

Result obtained for energy level 15 KeV seem to invert the trend for which at a higher compressive residual stress corresponds a longer fatigue life, but in that case there is not a high difference in compressive residual stress value between the two analyzed solutions. In all other cases, obtained for 12 and 18 KeV energy level, where the difference in compressive residual stress magnitude is bigger

Coupon Number	Laser Parameters [GW/cm ²], overlap percentage	Geometry Configuration [mm]	Higher Compressive RS [MPa]	Cycles to Fatigue, Elettra	Cycles to Fatigue, balanced
19	2.5-100	70-15-10	-152	1590000	33400
17	1.5-500	70-15-10	-94	87100	32600

Table 8.9: Comparison on fatigue performance between coupons 19 and 17, 18 KeV

between the two analyzed solutions, it is highlighted that the best performance in fatigue life is always associated to the higher compressive residual stress. for coupons tested at 12 and 18 KeV the geometric configuration is the same, this means same distance from the laser pattern to the coupon edge, thus same space to recover equilibrium, same distance from crack tip and same shot pattern width. Coupon 11, which is the worst one in terms of predicted fatigue life, is that showing the higher compressive residual stress, but is also the one having the laser pattern of same dimension as the others, but farther from the specimen edge, thus from the crack tip; this case the crack accelerates such that even the higher compressive residual stress reached by LSP treatment is not able to act as an obstacle, resulting in a detrimental effect on fatigue life.

Bibliography

- [1] Donald R. Askeland. *The Science and Engineering of materials* Third Edition, 1996.
- [2] Stefano Coratella. *Seminar in Residual Stresses Measurement Techniques*, University of Bologna, 26 November 2014.

CHAPTER 9

Friction Stir Welding

9.1 Welded joints

Welded joints are possible sources of defects leading to fatigue failure. Stress concentrations arise on and near the welded area due to thermal effects ??, ??:

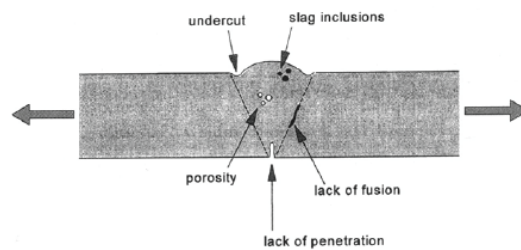


Figure 9.1: possible defects in welding

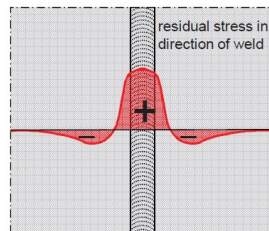


Figure 9.2: residual stress induced by welding

A very effective way to reduce the thermal stresses is the application of laser shock peening on the welded area.

In this chapter an analytical prediction of Fatigue Life of a FSW plus LSP treated specimen has been conducted and compared with the experimental results find in the literature [?].

9.2 Background

The analytical predictions are based on [?]. The mentioned paper deals with the prediction of fatigue life of a component including a crack approaching a residual stress field induced by friction stir welding and laser shock peening. The residual stress distribution is represented as:

$$\sigma_y = \sigma_0 \frac{1 - x^2}{1 + x^4} \quad (9.1)$$

Once the residual stress distribution has been defined, the stress intensity factor for the crack located in the residual stress field can be described as follows:

$$K \pm a = \frac{1}{\pi a} \int_{-a}^a \sigma_y(\xi) \sqrt{\frac{a \pm \xi}{a \mp \xi}} d\xi \quad (9.2)$$

The reported equation for stress intensity factor is valid for a symmetric crack ??:

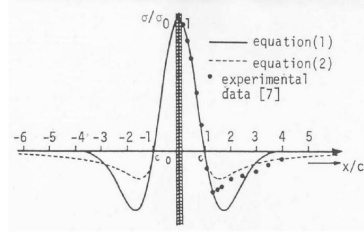


Figure 9.3: Symmetric Crack Configuration

as described in the paper, when the crack is eccentric, the stress intensity factor can be calculated replacing $(x+L)$ in σ_y equation, ??

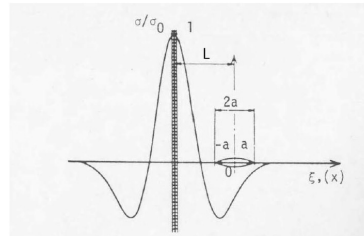


Figure 9.4: Eccentric Crack Configuration

Where L is the distance between the welded center line and the crack center line. The evaluation is conducted using the following integration formula:

$$\int_{-a}^a \sigma_y(\xi) \sqrt{\frac{a \pm \xi}{a \mp \xi}} d\xi = 2a \sum_{i=1}^n w_i \sigma_y(y_i) \quad (9.3)$$

where $y_i = \mp a(1 - 2x_i)$, $w_i = \frac{2\pi x_i}{2n+1}$ and $x_i \cos^2\left(\frac{(2i-1)\pi}{2(2n+1)}\right)$

9.3 Analytical Model

The investigated configuration is that reported in ??

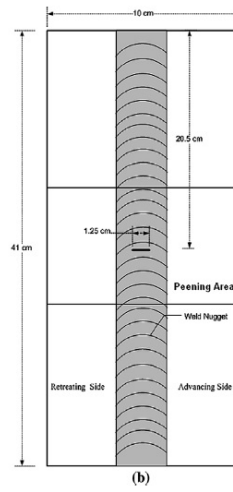


Figure 9.5: Investigated Configuration

According to [?]the investigated material is Al 7075-T7351.

Material	Yield Stress [MPa]	Ultimate Strength [MPa]	Total Elongation [%]
FSW 7075-T7351	226	339	5.5

Table 9.1: FSW Al 7075-T7351

Input parameters required are:

- R, loading ratio
- External Load
- $\sigma_y LSP$, maximum compressive residual stress at the laser center-line
- $\sigma_y FSW$, maximum tensile residual stress at the weld center-line
- a_0 initial crack length
- a_e final crack length
- Specimen Width
- Laser Shock Peening pattern width

- Friction Stir Welding pattern width
- distance between the crack center-line and the FSW path center-line
- distance between the crack center-line and the LSP path center-line

In the case of interest, the above mentioned parameters used, are that reported in [?], except for the external load, which, not being reported was supposed to be 30 MPa.

9.4 Output parameters and Comparison with the Experimental Results

As output parameters, the model gives a percentage of the effect of the double treatment (FSW and LSP) in terms of fatigue life, which in this case is estimated in 62% benefit in respect to the baseline.

The model provides also the residual stress distribution for FSW, LSP, FSW plus LSP, and eventually their comparison with the experimental results, ??

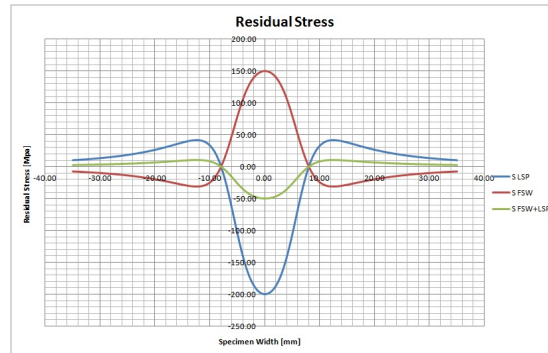


Figure 9.6: Residual Stress Distribution for FSW, LSP, FSW plus LSP as estimated by the model

Third output provided by the model is the Stress Intensity Factor, in terms of comparison between that referred to the baseline and that to the one predicted by the model for the FSW plus LSPeened specimen ??

The model provides also a fatigue crack propagation estimation which has been reported in the following picture in terms of comparison between baseline, predicted and experimental one, ??

A comparison in terms of fatigue life in respect to the baseline can be done only if the Paris Coefficients of the pristine material are given.

Finally the model gives an estimation of the fatigue crack propagation rate in terms of comparison between the baseline, the analytical prediction and the experimental results as in ??

A good correlation of the analytical model with the experimental results can be noted. The effectiveness of LSP treatment in the welded area has been proved. This solution can be implemented on actual loaded joints in order to improve the effectiveness.

9.4. OUTPUT PARAMETERS AND COMPARISON WITH THE EXPERIMENTAL RESULTS CHAPTER 9. FRICTION STIR WELDING

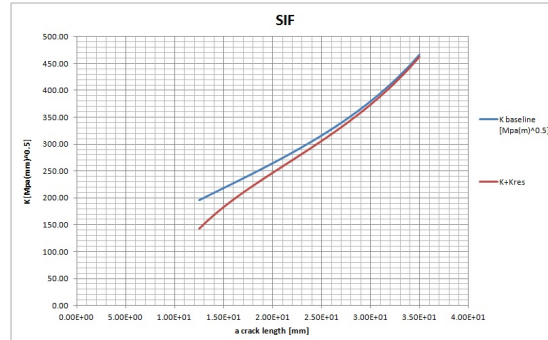


Figure 9.7: Stress Intensity Factor, comparison between the baseline and the predicted one

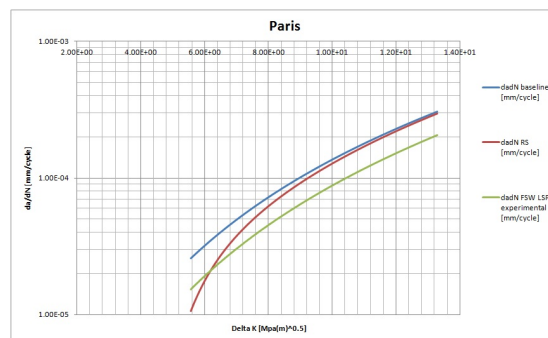


Figure 9.8: Paris Curve

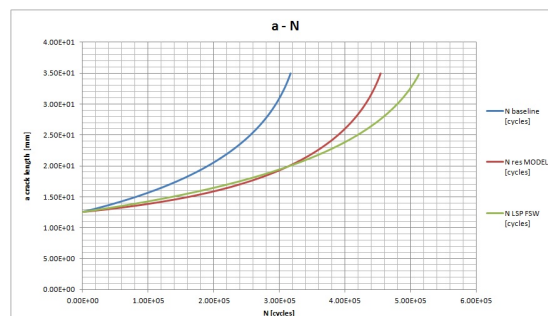


Figure 9.9: Fatigue Crack Propagation Rate

Bibliography

- [1] Omar Hatamleh. *Laser and shot peening effects on fatigue crack growth in friction stir welded 7075-T7351 aluminum alloy joint* 2009.
- [2] Hiroyuki Terada. *Stress Intensity Factor Analysis and Fatigue Behavior of a Crack in the Residual Stress Field of Welding* 2005.
- [3] Omar Hatamleh. *A Comprehensive investigation on the effects of laser and shot peening on fatigue crack growth in friction stir welded AA 2195 joints* 2009.

Bibliography

- [1] Omar Hatamleh. *Laser and shot peening effects on fatigue crack growth in friction stir welded 7075-T7351 aluminum alloy joint* 2009.

CHAPTER 10

LSP in LEAF

Aim of this chapter is to provide an overview on what already exists in terms of an analytical tool developed within Fatigue and Damage Tolerance research group for fatigue crack propagation prediction in stiffened panels, adding the effect of friction stir welding and laser shock peening treatments.

10.1 Introduction

Airframe are mainly composed of thin panels, known as skin, and reinforcing longitudinal and transversal objects, such as stringers, doublers, frames and tear straps. Damage Tolerance performances are mainly attributed to these stiffening elements. When introducing those reinforcing elements, a compromise has to be reached between low weight and high structural reliability. The stress state close to the crack tip in thin metallic structures can be studied by means of the stress intensity factor, usually referred as K in the linear elastic fracture mechanics approach. In 1969, Poe developed a method to predict the SIF on thin flat skin characterized by equally spaced riveted stiffeners with a propagating crack. This model was then extended by Swift to account for rivets flexibility and bonded stiffeners.

Masterlab laboratory has developed an analytical tool called LEAF, Linear Elastic Analysis of Fracture, to predict the fatigue crack propagation of pressurized metallic fuselages characterized by various fastening systems and damage scenarios. In a design phase, analytical tools are preferred to the FEM ones since require less computational time and costs. Thanks to the work carried on by previous students, LEAF has been validated on several experimental results, thanks to Airbus GmbH collaboration.

Fatigue phenomenon has been responsible of several failures due to cyclic loading. The first studies to investigate fatigue were developed by August Wohler in the second half of 1800. Wohler showed that fatigue occurs by crack growth from surface defects until the structural component cannot longer sustain the applied cyclic load. He also introduced the concept of S-N curve which relates

the applied stress to the number of cycles leading the component to failure. This curves are important, since including also the initiation time of defects; based on that are the chosen loading conditions applied to the fatigue tests carried out in this work of thesis.

Structures and materials are subjected to degradation during operational lifetime. Corrosive environments can facilitate the nucleation of fatigue defects. Damages can also be caused by accidental impact or introduced as a result of deficient processes of production and assembly, thus highlighting that also new aircraft entered into service may not be free from defects.

Damage Tolerance regulation is described in 571 part 25 of the European Aviation safety Agency (EASA) and the American Federal Aviation regulation (FAR).

Damage Tolerance Philosophy is mainly based on the following two principles:

1. how the resistance of a structure is affected by the presence of a damage (RS)
2. how long does the damage take to propagate due to fatigue (FCP)

Starting from the two reported principles it is highlighted the need to detect and repair the damage before it reaches critical dimensions (a_{cr}). If the PSE is not easily detectable, thus it is impossible to define an inspection time, the damage tolerance philosophy cannot longer be applied; this way, the application of the safe-life approach, thus no defects occurring in the structure during all its service time, is recommended.

One of the disadvantages in the adoption of the safe life approach is the increase in the structural weight; two examples of safe life components in civil aviation are the landing gear and the engine mounts.

As already mentioned, fatigue life predictions are mainly based on the linear elastic fracture mechanics approach; this limits the study to those materials which have a linear elastic relationship between stresses and strains during the crack propagation, or the fatigue failure must occur before the intact part of material becomes plastic.

In LEFM, the fracture analysis can be carried out by means of the stress intensity factor K , which describes the state of stress near the crack tip:

$$\sigma_{ij}(r, \theta) = \frac{k}{\sqrt{2\pi r}} f_{ij}(r, \theta) \quad (10.1)$$

where:

- (r, θ) are the polar coordinates of a system whose origin is placed at the crack tip
- σ_{ij} is the stress tensor near the crack tip
- f_{ij} is a trigonometric tensor function

The SIF can be expressed as:

$$K = \beta \sigma \sqrt{2\pi a} \quad (10.2)$$

where:

- β is the geometric correction factor
- σ is the applied remote stress
- a is half crack length

The geometric correction factor β takes into account several effects such as stiffeners, fuselage radius and so on.

failure occurs when the SIF value exceeds the toughness value, referred as K_c . The fracture toughness, as other engineering parameters like the Young modulus, must be obtained from experimental tests. K_c depends on thickness and width of the body, as well as on the component material.

In presence of a crack, at the crack tip, the plastic material is surrounded by the material remained elastic and, thus, deformations are possible only on the free surface of the panel.

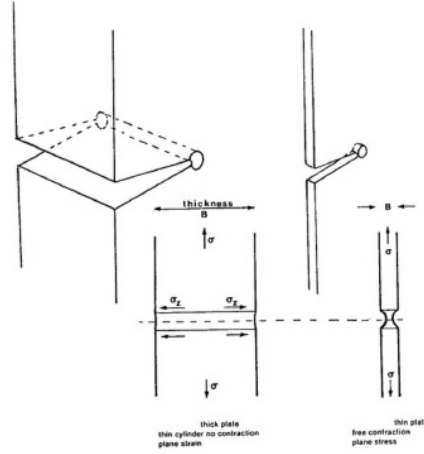


Figure 10.1: Deformation of the plastic zone for thick and thin panels

The thicker is the panel, the lower is the deformation because there is a higher amount of surrounding elastic material which restrains the deformations, and vice-versa. Based on this the following definitions:

- Plane strain state, which is representative of a thick panel and characterized by σ_{zz} different from zero
- Plane stress state, which is representative of a thin panel where σ_{zz} is equal to zero

Based on these two state definitions, it can be understand that for a thin cracked panel, the fracture toughness is much higher compared to that of a thick panel.

For any structure with known β and K_c , for a given crack length equal to $2a$, it is possible to determine the stress at which failure will occur, thus:

$$\sigma_c = \frac{K_c}{\beta\sqrt{2\pi a}} \quad (10.3)$$

The above equation represents the residual strength.

Nevertheless, this approach cannot be applied easily to thin panels, such as that object of this work of thesis, since K_c varies strongly with the thickness and cannot be considered as a material property.

As reported in the picture ??:

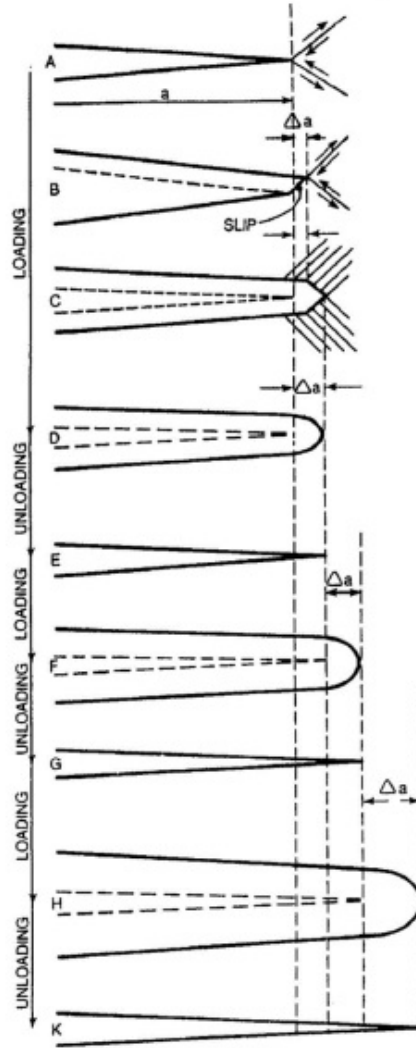


Figure 10.2: Crack Propagation Mechanism

A plastic deformation is a sliding of the atomic planes of the material due to a shear stress, phase B of ???. The progress of the sliding over complementary planes produces a rounded crack tip (phase B to D) pf ???. The first sliding step produces a small increase Δa of the crack. During the relaxation phase (or phase of compression), the crack tip returns sharp. In the later stage, the loading phase is repeated causing the increment Δa of the crack.

In the case of cyclic loading the main parameters leading the FCP are:

•

$$\Delta\sigma = \sigma_{max} - \sigma_{min} \quad (10.4)$$

•

$$R = \frac{\sigma_{min}}{\sigma_{max}} \quad (10.5)$$

As a consequence:

$$\Delta K = \beta \Delta\sigma \sqrt{2\pi a} \quad (10.6)$$

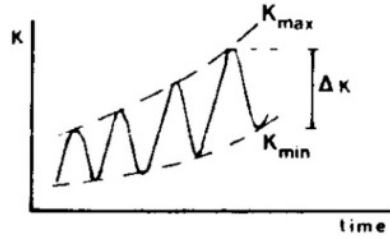


Figure 10.3: SIF vs time

As reported in ??, it can be note that a constant amplitude $\Delta\sigma$ produces a SIF ΔK which increases with time.

Generally fatigue crack propagation is measured in mm/cycle and can be expressed as:

$$\frac{da}{dN} = f(\Delta K, R) \quad (10.7)$$

a typical trend is shown in ??:

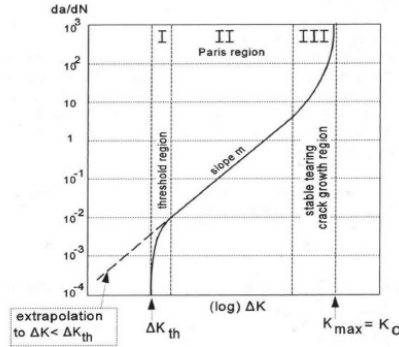


Figure 10.4: Fatigue crack propagation rate vs SIF (double logarithmic scale)

where three regions can be defined:

- First region is representative of a threshold value ΔK_{th} below which the propagation is just at atomic, thus microscopic scale
- Second region is defined by a linear relation between the crack growth rate and the ΔK , on double logarithmic scale

- in the third region, fatigue crack propagation increases steeply until it reaches a vertical asymptote, where the SIF equals the value of fracture toughness K_c

The FCPR relation considering only the linear region, follows the trend described by Paris law:

$$\frac{da}{dN} = C(\Delta K)^n \quad (10.8)$$

where the C and n parameters must be determined experimentally. The number of loading cycles N that a fatigue crack takes to propagate from an initial crack length a_0 to a certain crack length a_i can be obtained by integrating the reciprocal of the crack growth rate per unit cycle, as:

$$N = \int_{a_0}^{a_i} \left(\frac{1}{\frac{da}{dN}} \right) da \quad (10.9)$$

this way, knowing the a_{cr} the interval time for inspection corresponding to N_{cr} can be established, thus answering to the second question of the damage tolerance philosophy.

Looking at a stiffened structure as that reported in picture ??:

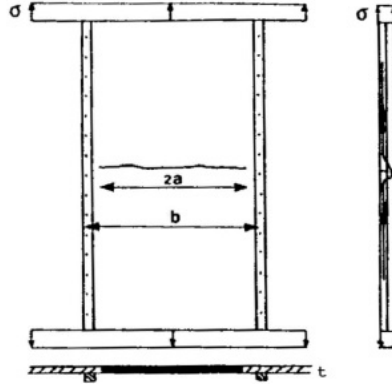


Figure 10.5: Stress distribution between skin and stiffeners

it is possible to understand how stiffeners create a secondary load path which, in the presence of a crack, reduce the state of stress acting on the skin. For example, consider the panel characterized by Young modulus E and t thickness, fastened by a stringer of elastic modulus E_s and cross section A_s , subjected to a remote stress σ and severed along the stiffeners bay (width b), by a crack $2a$. In stiffened panels the crack tip stress is transferred from the skin to the stiffener and back to the skin again. Therefore, under the same crack length $2a$ and the same remote stress σ , a stiffened panel has a SIF lower than the unstiffened one. The effect of the stiffeners on the SIF is expressed by means of the following:

$$\beta_s = \frac{K_{stiff}}{K_{unstiff}} \quad (10.10)$$

that is purely a geometric effect.

The skin SIF reduces when the crack approaches the stiffener, whose stress is increased as:

$$L_s = \frac{F}{\sigma_s A_s} \quad (10.11)$$

where :

- L_s is the load concentration factor
- F is the force reacted by the stringer
- σ_s is the remote stress applied to the stringer

The stiffener of a fuselage increases when increasing the section and the elastic modulus of the stiffeners.

Circumferential and longitudinal stresses which arise due to the fuselage pressurization, can be approximated by boiler formulas as:

$$\sigma_\phi = \frac{\Delta p R_f}{t_f} \quad (10.12)$$

$$\sigma_\chi = \frac{\sigma_\phi}{2} \quad (10.13)$$

where:

- Δp is the difference between the internal and external pressure
- R_f is the fuselage radius
- t_f is the fuselage skin thickness

A further contribution to fuselage loads is given by the bending stress, which originates from the superimposition of the distributed weight of the airframe and the vertical acceleration due to gust and manoeuvrings. The bending stresses can be represented by the classical butterfly distribution, decreasing linearly from the fuselage crown (subjected to tension) to the belly (subjected to compression).

Pressurization stresses are constant along the fuselage length whereas the bending stress reaches its maximum in correspondence to the wing attachments, where the wing lift loads are reacted by the fuselage.

Typical fuselage scenarios are that reported in picture ??:

LEAF analytical tool, developed by previous students has been validated by means of the comparison with the experimental results in different damage scenarios, as that reported in picture ??:

The tool LEAF can account for different configurations, such as:

- effects of rivets
- integral and adhesive bonded stringers on FCP performances
- bonded doublers placed in the middle of the stringer bays
- presence of debonding at the interface between the cracked skin and the doublers

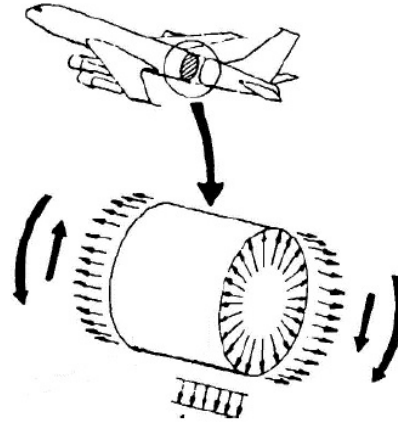


Figure 10.6: Fuselage stress components; hoop plus bending

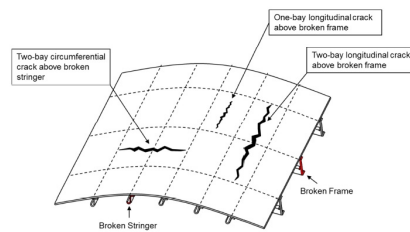


Figure 10.7: Typical fuselage damage scenarios

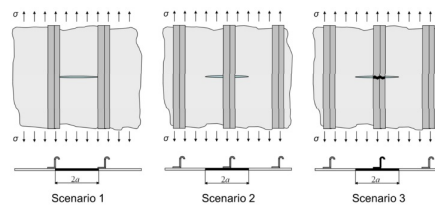


Figure 10.8: LEAF investigated damage scenarios

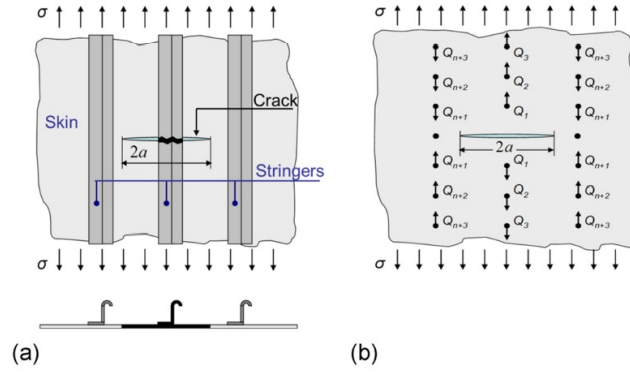


Figure 10.9: Stiffened panel with crack propagating beyond broken stringer; (a) sketch, (b) modeled loading condition

The analytical approach adopted in LEAF can be summarized as follows.
??:

Consider a crack propagating along a stiffened panel, with remote stress acting parallel to the stiffeners as reported in ??. SIF can be divided into two components by the superimposition principle:

- the SIF due to the remote stress applied to the cracked sheet
- the SIF due to the load carried by the stiffeners

Each Stiffener can be modeled by a concentrated force Q_j located at its center line; the complete solution is mathematically represented as:

$$K_{stiff} = K_{unstiffened} + \sum_{j=1}^{N_F} K_j Q_j \quad (10.14)$$

Thus the sum of:

- SIF associated to a through the thickness crack in an unstiffened infinite flat panel loaded by σ stress
- SIF associated to a through the thickness crack in an unstiffened infinite flat panel due to a set of four concentrated forces (Q_j), placed symmetrically in respect to the crack origin

The K equations ($K_{unstiff}$ and K_j) of a crack propagating orthogonally in respect to the stiffeners, and to the remote stress, are available in the literature. To calculate the SIF for the stiffened panel, the force reacted by the stiffeners must be known.

Stiffeners act as skin crack retarders, reducing the crack growth rate, and stoppers, arresting unstable fast crack propagation. At the basis of this behavior is the capability of the stiffeners to transfer the load from the cracked skin to the stiffener. The effectiveness of the stiffeners as crack retarders has been investigated by several authors in the past; in 1970, Poe compared the fatigue crack propagation crack in flat wide panels with bolted and integral stiffeners subjected to a constant amplitude fatigue load.

Poe developed a method to evaluate the magnitude of the concentrated Q_j , based on the compatibility of the displacement parameter between the cracked skin and the stiffeners at the same location. Based on the compatibility method, the displacement of skin and stiffeners can be expressed by means of the compliance coefficients, which represent the displacement per applied unit force or stress. The compliance matrix A_{ij} of a general elastic body can be expressed as the displacement of the point (x_i, y_i) due to a force Q_{ij} located at (x_j, y_j) ; in the same way, the displacement of point (x_i, y_i) per unit of applied remote stress can be represented by the compliance vector B_i . Again, invoking the superimposition principle, the displacement field in the cracked skin can be expressed as the sum of the part due to the concentrated forces and that due to the remote skin stress. The same for the displacement of the stiffeners at the same location. At this point, the compatibility between skin and stiffeners displacement has to be superimposed, and this lead to a system of linear equations in the unknown force. The flexibility of the jointing system can be accounted by adding an additional compliance matrix A_{ij}^{joint} of the jointing system, being it either riveted or adhesively bonded.

As depicted in ??:

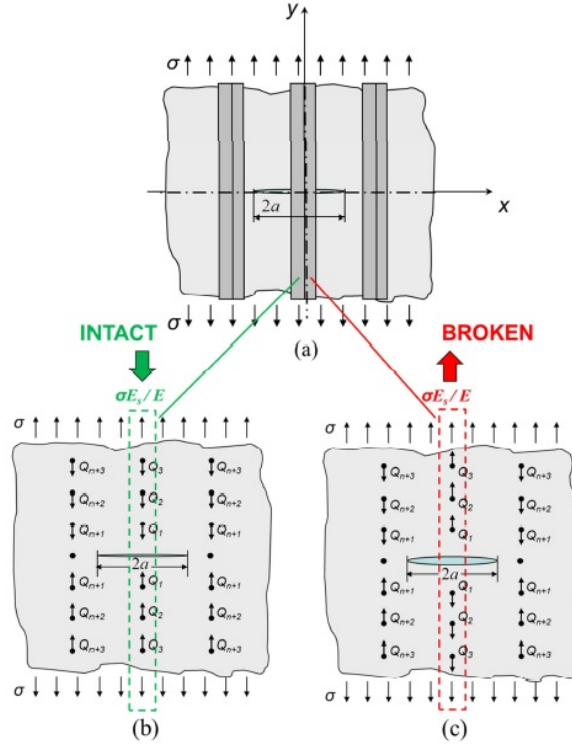


Figure 10.10: Reaction forces directions for intact and broken stiffeners

The load transfers from the broken skin to the intact stiffener increasing its stress in the y direction, according to ??.

In case of an intact stiffener, to satisfy equilibrium, the forces reacted from the cracked skin are directed in the y negative direction, thus resulting in a

reduction of the stress field in front of the propagating crack. Therefore the SIF contributions associated to an intact stiffener are negative, as $K_j Q_j < 0$. This way, it can be concluded that intact stiffeners act as crack retarders.

On the opposite, a broken stiffener subjected to a remote stress results in a tensile state of stress acting on the propagating skin crack. Therefore the SIF contributions associated to a broken stiffener are positive, thus $K_j Q_j > 0$, accelerating the crack growth.

As reported before, since the SIF is usually regarded as a geometric effect, also for the stiffeners it is expressed in terms of geometric correction factor β , as:

$$\beta_s = \frac{K_{stiff}}{K_{unstiff}} \quad (10.15)$$

Additional elements acting as crack retarders are the doublers and tear straps, which are placed under the main stiffener and contribute to a further reduction in fatigue crack propagation. Doublers and tear straps are flat elements usually made of aluminum, titanium, or fiber metal laminates, that is a material composed by metal and composite layers, typically glass fibers.

Also in this case, to account for doublers and tear straps, an additional compliance matrix can be used, where its coefficients are function of their cross section and elastic modulus.

If the doubler is placed under the stiffener, its effect is represented by an equivalent stiffening element, characterized by the overall amount of cross section area and elastic modulus, that is:

$$A_{eq} = A_d + A_s \quad (10.16)$$

and

$$E_{eq} = \frac{A_d E_d + A_s E_s}{A_d + A_s} \quad (10.17)$$

LEAF analytical tool has been validated through an extensive test campaign, submitted by Airbus GmbH, focused on seven stringer panels characterized by different geometries and skin materials. Studies conducted by previous students, demonstrated the ability of LEAF to predict the benefit in fatigue life provided by an intact stiffened structure.

As can be easily predicted, a lower rivet pitch leads to a lower fatigue skin propagation rate, thus to a longer fatigue life. Since the one bay damage scenario proved to be the critical one, this has been chosen as the sizing criterion for the damage tolerance design philosophy. Within this configuration, the higher tensile stresses are those acting in the middle of the skin bay, which in turn result as an area prone to crack nucleation.

Nevertheless a broken stiffener can be representative of a flight condition resulting from accidental impact; this case the crack propagating on both sides of the broken stiffener has been investigated highlighting its detrimental effect on fatigue life.

LEAF confirmed the riveted joints to be less effective than both adhesively bonded and integral joints.

Previous analyses proved the displacement compatibility method upon which LEAF is based to be non reliable in fatigue crack growth prediction, when the skin crack tip is propagating above the bonded stiffener. This can be due to

the inadequacy of the displacement compatibility method to capture the real mechanism driving the skin crack propagation above the adhesively bonded stiffener.

Since the fuselage is subjected to a bi-axial state of stress due to pressurization loads, the original displacement compatibility equations have been modified to account for the bi-dimensional skin displacement field. This has been again achieved by means of the superimposition principle, dividing the contributions to:

- effect of the skin stress acting orthogonally to the propagating crack, that is parallel to the stiffening element
- effect of the skin stress acting parallel to the propagating crack, that is orthogonally to the stiffening element

An other important factor affecting the fatigue propagation in stiffened structures, is the secondary bending induced by the stiffening elements eccentricity. As can be seen in ??:

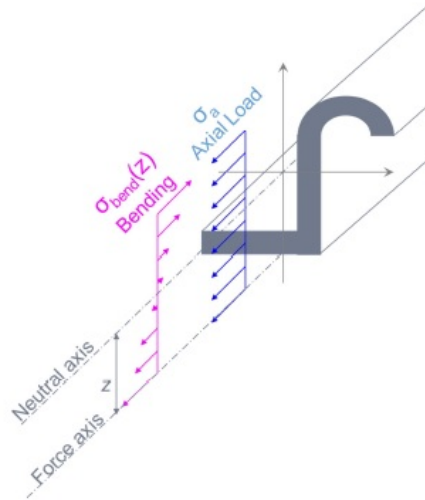


Figure 10.11: Secondary bending effect due to stiffeners eccentricity

as the skin crack propagates, the force reacted from the stiffener, acts at a distance z_0 from the neutral axis, causing the bending stress to be superimposed to the stiffeners axial stress. This way, the resulting increase in the skin stress increases the SIF, thus leading to a faster crack growth rate. This secondary bending effect has been modeled within LEAF.

The model implemented in the Matlab for fatigue life prediction of laser peened components and validated with experimental results, has been introduced in the analytical tool LEAF, ??:

The user interface is reported in ??:

The LSP treatment can be easily enabled by the user. The introduction of laser shock peening treatment in LEAF gives the chance to enlarge the distance between stiffeners, thus reducing the amount of needed holes, which

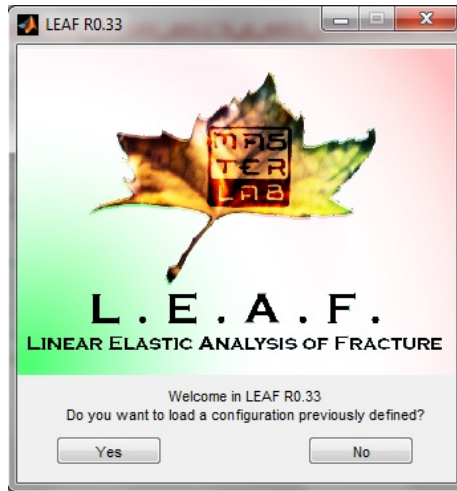


Figure 10.12: LEAF logo

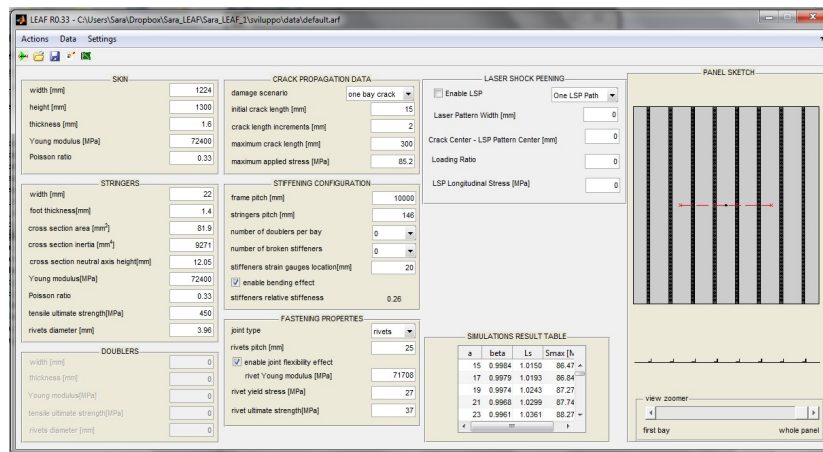


Figure 10.13: LEAF interface, including LSP treatment

are areas subjected to the higher stresses, thus prone to fatigue, and the overall structural weight. Resulting in a compressive residual stress state, and knowing the areas more prone to fatigue, it is possible, according to the prediction made by the analytical validated model, to introduce laser peening stripes between the stiffeners and resulting in a crack growth slow down.

Next step will be the introduction in LEAF of the friction stir welding treatment analytical model. This way it will be possible to predict the fatigue behavior of a FSW and LSP component. Since both function can be enabled by the user it will be possible to implement as well a model involving the presence of just LSP or FSW treatment, and check the effects of the both on fatigue, detrimental in case of FSW, beneficial for LSP.

Results are given in terms of propagating crack dimension, β geometric factor, maximum stress, most highly loaded stiffener stress intensity factor.

Results are provided as plot and as txt or excel documents, which are easy to handle in subsequent analyses.

Bibliography

- [1] Gianluca Molinari. *Fatigue Crack Propagation in pressurized metallic fuselages*, Scuola di ingegneria e architettura, universit di Bologna, 2013.
- [2] U. Zerbst, M. Heinimann, C. Dalle Donne, D. Steglich. *Fracture and damage mechanics modelling of thin-walled structures - An overview*, Engineering Fracture Mechanics, Volume 76, Issue1, pp 5-43, 2009.
- [3] T. Swift. *The application of fracture mechanics in the development of the DC-10 fuselage*, Fracture Mechanics of Aircraft Structures, AGARD-AG-176, H.Liebowitz, Ed. AGARD Advisory Group for Aerospace Research and Development, pp 226- 287, 1974.
- [4] T. Swift. *Fracture Analysis of Adhesively Bonded Cracked Panels*, Journal of Engineering Materials and Technology, Vol. 100, pp 10-15, 1978.
- [5] G. Molinari, I. Meneghin, M. Melega, E. Troiani. *Parametric damage tolerance design of metallic aeronautical stiffened panels*, The Aeronautical Journal, Vol. 116, 2012.
- [6] I. Meneghin and M. Pacchione. *Investigation on the design of bonded structures for increased damage tolerance*, in Proceedings of the 25th Symposium of the International Committee on Aeronautical Fatigue, 2009.
- [7] Anonymous. *Damage tolerance and fatigue evaluation of structure*, FAR Part 25 Sect. 571, Federal Aviation Administration, 1997.
- [8] D. Broek , *The Practical Use of Fracture Mechanics*, Springer, 1989.
- [9] S. Timoshenko. *The theory of plates and shells*, McGraw-Hill, 1964.
- [10] W. Flugge. *Stress problems in pressurized cabins*, NACA-TN-2612, 1952..
- [11] Anonymous. *Damage tolerance and fatigue evaluation of structure*, FAR 25.571-1D, Federal Aviation Administration, 2011.
- [12] C.C. Jr. Poe. *Fatigue crack propagation in stiffened panels*, *Damage Tolerance in Aircraft Structures*, ASTM STP 486, pp 79-97, 1971.

- [13] J. Schijve. *Crack stoppers and ARALL laminates*, TU Delft Tech. Report LR-589, 1989.
- [14] I. Meneghin, M. Pacchione, P. Veermer. *Investigation on the design of bonded structures for increased damage tolerance*, in Proceedings of the 25th Symposium of the International Committee on Aeronautical Fatigue, 2009.
- [15] C.C. Jr. Poe. *Stress intensity factor for a cracked sheet with riveted and uniformly spaced stringers*, NASA TR-R-358, 1971.
- [16] C.C. Jr. Poe. *The Effect of Broken Stringers on the Stress Intensity Factor for a Uniformly Stiffened Sheet Containing a Crack*, NASA TM X-71947, 1973.
- [17] G. Dowrick and D.J. Cartwright. *Biaxial stress effects in a reinforced cracked sheet*, *International Journal of Strain Analysis*, Vol. 19, pp. 61-69, 1984.
- [18] T. Swift. *Fracture Analysis of stiffened structures, Damage Tolerance of Metallic Structures: analysis Methods and Applications*, ASTM STP 842, pp 69-107, 1984..
- [19] T. Swift. *The application of fracture mechanics in the development of the DC-10 fuselage*, In *Fracture Mechanics of Aircraft Structures*, AGARD-AG-176, H.Liebowitz, Ed. AGARD Advisory Group for Aerospace Research and Development, pp 226- 287, 1974.
- [20] T. Swift and D.Y. Wang. *Damage Tolerant Design Analysis Methods and Test Verification of Fuselage Structures*, Air force Conference on Fatigue and Fracture of Aircraft Structures and Materials, AFFDL-TR-70-144, 1969.
- [21] R.W. Peters and P. Kuhn. *Bursting Strength of Unstiffened Pressure Cylinders with Slits*, NACA TN-3993, 1957.
- [22] R.B. Anderson and T.L. Sullivan. *Fracture Mechanics of Through-Cracked Cylindrical Pressure Vessels*, NASA TN D-3252, 1966.
- [23] P. Kuhn. *TNotch Effects on Fatigue and Static Strength*, Presented at the Symposium on Aeronautical Fatigue Sponsored by the International Committee on Aeronautical Fatigue (ICAF) and the Structures and Materials Panel of the Advisory Group for Aeronautical Research and Development (AGARD), 1963.
- [24] E.S. Folias. *An axial crack in a pressurized cylindrical shell*, *International Journal of Fracture Mechanics*, Vol. 1 , pp. 104-113, 1965.
- [25] E.S. Folias. *A Circumferential Crack in a Pressurized Cylindrical Shell*, *International Journal of Fracture Mechanics*, Vol. 1 , pp. 1-22, 1967.

CHAPTER 11

Conclusions

11.1 Conclusions

The laser shock peening is widely supposed to be a very effective solution in extending fatigue life of bulk metallic components. Unfortunately, lack of data for thin panels, typical of aerospace structures, reduces the viability of this technique in many applications. To extend the knowledge of LSP effects, a time and cost saving approach (when compared with standard experimental activities) involving numerical and analytical simulations and predictions has been developed. From the results of the present work, LSP is confirmed as an effective method to introduce significant compressive residual stresses in fatigue sensitive areas also of thin metallic structures, postponing fatigue crack nucleation. The application of the numerical FE simulation to LSP showed to be extremely difficult as a consequence of the parameters involved in the process. An optimized ABAQUS/Explicit model was developed and calibrated by means of experimental results. The numerical investigations led to a reliable finite element model, valid even for complex geometries. The standard Johnson-Cook material model has been compared with a new kinematic hardening model, that showed its effectiveness in residual stress prediction. All those new settings have been applied to numerical analyses with different geometry models to verify its robustness for different thicknesses. The calibration of the model with experimental results was based on stress and displacement measurements. Displacement calibrations showed an excellent correlation between experimental and numerical results, while stress calibrations highlighted numerical discontinuities problems that however disappear in multiple spots or multiple layers configurations. The stress calibration was achieved using the experimental data from an extensive test campaign done at Elettra facilities. XRD measurement of the residual stresses in thin aluminum panels confirmed the numerical FEM results. Simulations globally show good fitting with those experimental results proving the numerical model to be reliable for prediction of detailed effects of LSP. Furthermore, another goal of the thesis was to investigate the enhancement in fatigue crack propagation

performances induced by LSP on structures which are representative of aircraft fuselage skin. The experimental data obtained on simple specimen showed no improvement achieved with some configurations of the LSP treated pattern. Using the previously validated FEM approach to predict the residual stress profile along the entire width of the LSP treated specimen, together with an analytical crack propagation model, a comparison of the FCP predicted performances has been done with the experimental data available, showing a good agreement. The model was then used to make predictions about the best peening configuration to achieve benefit in terms of fatigue crack propagation life after LSP treatment. This lead to the conclusion that, to extend component fatigue crack propagation life, the laser shot has to be placed close to the crack origin and a larger shot pattern has to be used. In this case, LSP can be very effective in enhancing fatigue life performances.

CHAPTER 12

Appendix

12.1 Metallography

Aim of this appendix is to provide an overview on crystallographic structure, as well as hardness and roughness, of Al 2024-T351 used for the laser treated coupon. A comparison of the grains refinement of the pristine material with the treated ones is provided analyzing both different laser peening strategies and also different material directions. Coupons are LT machined, and the baseline, according to the picture ??:

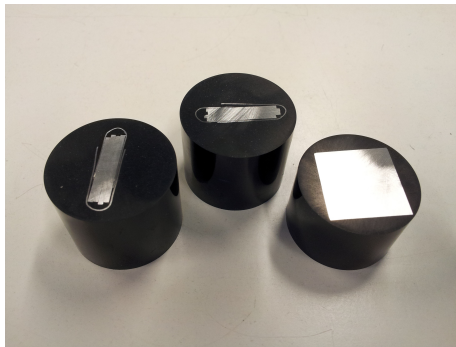


Figure 12.1: Baseline coupons, analyzed views, top, side, plane

is analyzed in plane, from top (expected round grains) and side (expected elongated grains). The same views, are analyzed for the shot configuration, adding an analysis of both in plane first side and second side peening. Since a great difference in the achieved residual stress profile is highlighted between different choice of scanning and stepping directions, both the laser configurations shown in picture ??, have been analyzed in the four previously mentioned views.

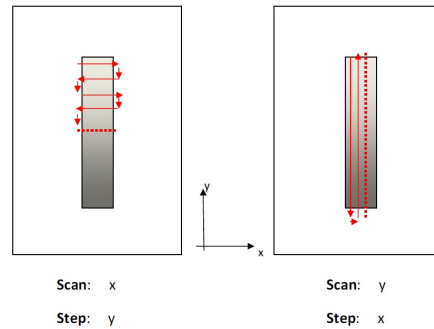


Figure 12.2: Scanning and stepping configurations analyzed

12.2 Microstructure in Aluminum Alloys

Aluminum is one of the mostly used material in aeronautical industry due to its ductility, which allows to obtain complicated shapes through plastic forming in easy implementable and low cost processes.

Aluminum is characterized by the so called stacking-fault energy, that is, during plastic deformations, a large number of dislocations annihilate and rearrange following the phenomenon of dynamic recovery. The occurring of this phenomenon makes it possible to compensate the formation of dislocations during hardening, and relieves the accumulated energy, thus giving rise to a steady state condition defined by a constant value of flow stress.

Microstructural examination shows that the dislocations density rises to a steady state level resulting in sub-grain structure which is smaller for higher stresses.

This is of primary interest in fatigue, since the grain size determines both the mechanical and aesthetical properties of the analyzed component.

A coarse grain size leads to undesired ductility, low strength and orange peel surface aspect. Moreover, grain texture influences material anisotropy.

Since during extrusion the grain size varies within the profile, depending on the machining direction, known as LT and TL, this has to be evaluated when implementing fatigue tests, since longer grains perpendicular to the crack growing direction (ie. LT machining and crack propagating in TL direction) constitute an obstacle resulting in lower FCP.

An other aspect to be taken into account especially when dealing with thick components, is that grains across the profile thickness are no longer the same; going from the core to the surface of the profile, this changes can be problematic especially when dealing with exposure to corrosive environment.

12.2.1 Specimen Preparation

Depending on temperature history and subjected strain, each specimen shows a particular microstructure. This way it is interesting to evaluate the specimen microstructure after laser treatment, since even if regarded as adiabatic, it involves plasma at high temperatures and is also characterized by high strain rates, such as 10^6 sec^{-1} . In order to see the coupon microstructure through the microscope, each sample has to be prepared, starting from its cutting from the

original component. The all preparation procedure is mainly composed of four phases, which are:

- embedding
- grinding
- polishing
- etching

This procedure is not difficult but needs to be carefully exploited, since especially in case of a large number of coupon, they have to be correctly identified; moreover, each machine is characterized by a specific operating time and settings. Embedding of the specimens has been done with an automatic machine and an epoxy resin. Sample diameter dimension is 30 mm. The pressure is set at 4 bar and the thermal cycle goes up to 160 °C. It lasts for 7 minutes and then decreases by means of a dedicated water circuit. The embedding procedure can be summarized as follows:

- Carefully clean all the machine surfaces
- Position the cut coupons in place on the machine plate
- Lower the plate
- Fill the cavity hosting the coupon with the epoxy resin
- tighten the machine coverage
- pull up the coupon
- set the pressure value at 4 bar
- start the machine

The thermal cycle, which keep the sample at 160 ° C for 7 minutes has been previously set according to the chosen epoxy resin. At the end of the described process the coupon has to be taken out and a siglum has to be assigned to each target. Before moving to the next phase, a 3 mm diameter hole has to be drilled on the back surface until the aluminum target is reached. Conductivity has to be checked.

Grinding is done by means of an other machine composed of a rotating plate upon which discs of different grades of abrasive paper are placed. A water nozzle is directed towards the coupon which is pressed on the grinding paper for the time needed to achieve a cleaned surface. This part of the procedure has to be carefully exploited especially for laser peened coupon in the in plane direction, since the major laser treatment effects characterize only few micrometers under the treated surface, even if a compressive residual stress field, thus a grain alteration, can be appreciated up to thicknesses of 1 mm. The grinding procedure consisted of four steps in which the abrasive papers with decreasing grain size have been adopted for the side and top views, and are reported in ??:

Samples have been taken in place on the rotating abrasive discs manually. The first two steps lasted 30 second, whereas the last two, one minute; at the

Grind Step	Paper grit size	Particle diameter
1 st	P 180	82 μm
2 nd	P 320	46.2 μm
3 rd	P 600	25.8 μm
4 th	P 1200	15.3 μm

Table 12.1: Sanding paper used for side and top view coupons

end of each step a visual inspection has been done to check the surface flatness of the surface. After each step the coupon have been washed with water but attention has been paid to not touch them any longer by hand, and after by alcohol, to avoid corrosion. After they've been dried by air.

the coupons have been further polished. During polishing the abrasive medium is no longer sanding paper, but a liquid suspension of alumina on a lubricant. The process required two steps, once again decreasing the abrasive particle size. A summary of the adopted strategy is reported in ??:

Polish Step	Disc plate	Suspension
1 st		Alumina 1 μm
2 nd		Alumina 0.05 μm

Table 12.2: Polishing steps

Each polishing step lasted for two minutes.

Whereas the plane view has been only polished, in the attempt to not damage or alter the laser effect which is more pronounced on the coupon surface.

Once the samples have been polished to the end, the coupon surface is ready to be treated with a reagent. This procedure makes it possible to observe grain boundaries with a microscope. The etchant used is a Barker's reagent, a solution made of 300 ml water and 8 ml fluoboric (HBF_4 acid. During etching a current flow is set between the back hole drilled on the back side of the coupon and the reagent. Tension is set to constant 20 V and current at 0.2 Amp for 1 minute. Because the Barker's reagent has to be kept at temperature below 20 °C to avoid burning the specimen, the container was stored in a fridge when not in use.

After the application of this procedure the coupons can be analyzed by polarized light. Doing so grain boundaries can be seen. Even if a naked eye cannot see the difference, in polarized light, wave have only one vibration direction, while in normal light all directions are equally probable. When the polarized light hits the specimen, its orientation is altered depending on the spatial orientation of grains. Then, if the light is filtered through a polarized filter, it's transmitted depending on the orientation of the filter itself, giving rise to false colors. The different colours seen on the screen can be associated to the different grains within the specimen with a resolution down to 15 °.

A large area characterized by the same colour can represent either one big grain or lot of them with the same direction. Areas not subjected to residual strains show uniformly shaped grains. Elongated or deformed grains shapes result from machining processes or mechanical or thermal treatments. High

strain rates processes result in finer grains. Attention must be paid in the result interpretation to not occur in misleading conclusions maybe due to erroneous polish and etching procedures.

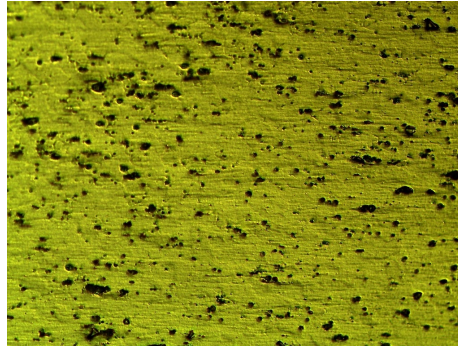


Figure 12.3: Acid effect on coupon

Picture ??, shows bubbles arising in the coupon after acid application.

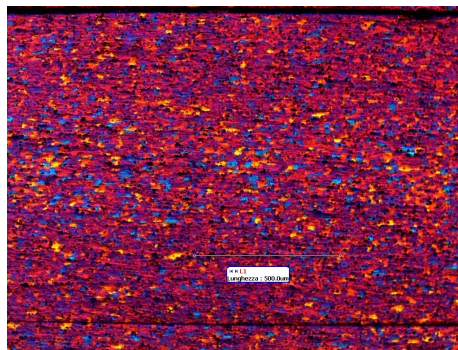


Figure 12.4: Optics measurement reference

Picture ?? shows a reference scale with which it is possible to compare the grain sizes reported in the various pictures and referred to the same optic, that is 5x.

Picture ?? shows the grains size of untreated Al 2024-T351. All grains are similar in dimension, as expected.

Picture ?? shows grains which are a bit elongated in the machining, thus LT, direction, as expected.

Picture ??, ?? and ?? are referred respectively to a non shot, border of the shot, and shot area. All the images are taken with the same optics, that is 20x. On the opposite of what expected there seem to be no difference in grains shape and dimensions between the laser peened and unpeened areas. Since LSP is a process involving high strain rates, it was expected to have smaller grains' dimensions in correspondence to the peened area. No further informations are available in the literature about this phenomenon.

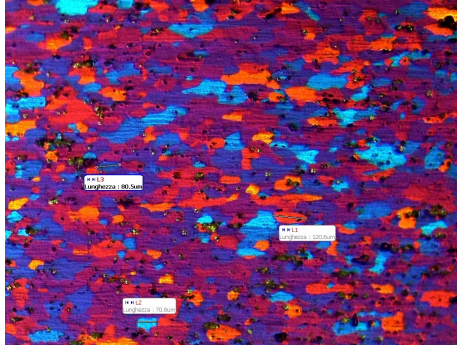


Figure 12.5: Grains measure at 20x for Al 2024-T351, untreated area

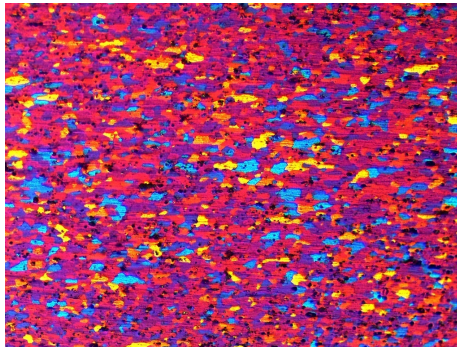


Figure 12.6: Elongated grains in untreated Al 2024-T351 coupon, 10x optic

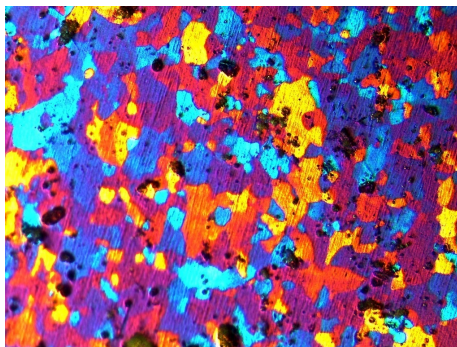


Figure 12.7: Grains shape outside the treated area, 20x

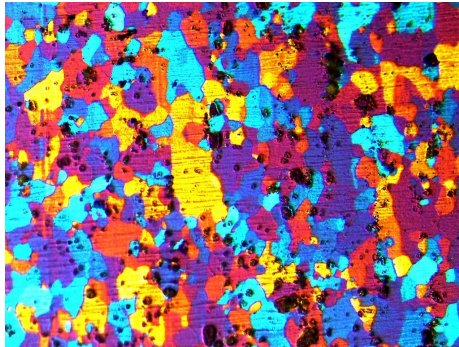


Figure 12.8: Grains shape aside the laser shot, 20x optics

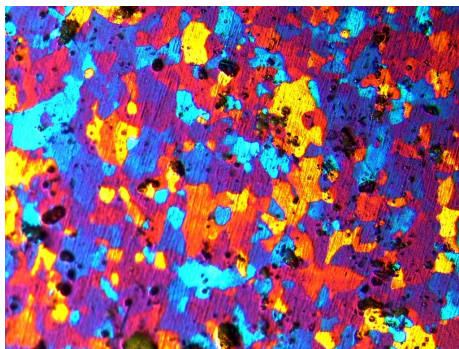


Figure 12.9: Grains shape of laser peened area, 20x

12.3 Hardness and Roughness Coupon Characterization

12.3.1 Testing Procedure: hardness

The tested coupon is one of that used to implement crystallographic analysis, thus embedded in a resin plate; this allowed to better fix the component to the hardness testing machine.

The coupon surface has been perfectly cleaned paying attention to not alter it.

The hardness machine working principle can be described as follows.

A diamond indenter in the shape of a pyramid with square base and specific angle between opposite faces at the vertex, is forced to the surface of the test piece. By subsequent measurement of the diagonal length of the indentation left on the surface after removal of the test piece, the Vickers hardness can be calculated.

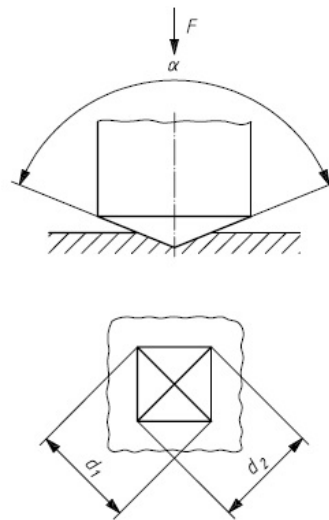


Figure 12.10: Vickers Test Principle

The Vickers hardness is proportional to the quotient obtained dividing the test force by the sloping area of the indentation, which can be identified with the pyramid having at the vertex the same angle as the indenter.

The Vickers Hardness has to be indicated as the Vickers value obtained from measurement, plus an indication of the applied force and test duration time.

The Vickers machine is reported in ??:

The tested coupon, shot peened in UPM, and highlighting the presence of both a pristine and a treated area is reported in ??:

A picture of the component within the machine while measuring is reported in ??:

The hardness value can be calculated by use of the table values given with the testing machine. The choice of using the coupon embedded within the resin gave

12.3. HARDNESS AND ROUGHNESS COUPON CHARACTERIZATION

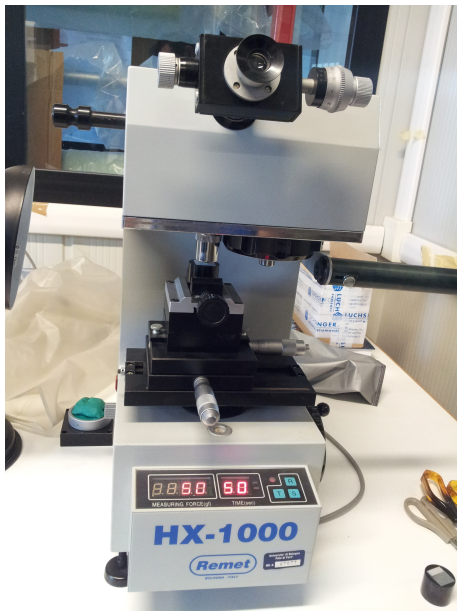


Figure 12.11: Vickers Testing Machine at Lab

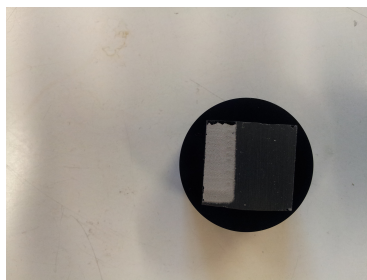


Figure 12.12: Coupon devoted to Vickers Test

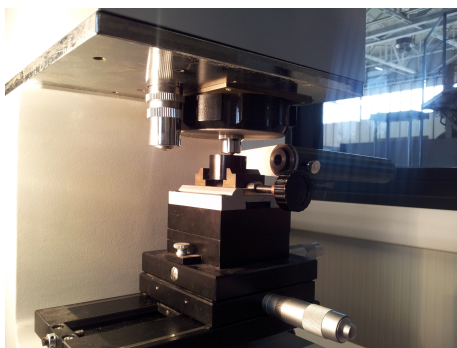


Figure 12.13: Vickers measurement

12.3. HARDNESS AND ROUGHNESS COUPON CHARACTERIZATION

the chance to better fix it to the machine during testing procedure; moreover the coupon has been treated so to be smooth, free from oxide and lubricants. Temperature during tests was within the range recommended by the regulations.

A force of 100 gr has been applied for a time interval of 10 sec.

The obtained hardness values are:

- Pristine Area: 100HV0.1-10
- Treated Area: 132HV0.1-10

Laser shock peening treatment resulted in an increase of the hardness parameter, as expected.

12.3.2 Roughness

Roughness has been measured both for coupons laser peened in UPM and at Witwatersrand University.

The specimen shot peened at UPM is $150 * 70 * 1.4$ mm, unclad, laser peening directions are reported below:

- scanning direction: y
- stepping direction: x

where, ??:

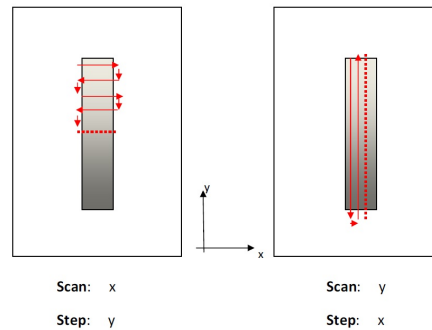


Figure 12.14: Laser Scanning and Stepping direction definition

The coupon is characterized by two side peening.

The achieved values of roughness values are:

- Unpeened material, $0.18 \mu\text{m}$
- Peened Material, Shot Side 1, $2.56 \mu\text{m}$
- Peened Material, Shot Side 1, $2.6 \mu\text{m}$

As expected the treated area is characterized by a higher roughness value. The roughness is equal on both peened sides, as expected, being the coupons treated with the same laser parameters on both the surfaces.

The roughness measured on the coupons laser peened at Witwatersrand university, are referred to a coupon with same material and geometry of that

12.3. HARDNESS AND ROUGHNESS COUPON CHARACTERIZATION

peened at UPM. The shot geometry is the same for all the analyzed configurations. Laser spot diameter equal to 1.5 mm for all the configurations. The only difference is that the coupon shot peened in SA are treated on one side only. Roughness due to different laser peening parameters configurations have been measured, that are:

- 2 GW/cm², overlap 500, roughness 1.95 μm
- 1.5 GW/cm², overlap 500, roughness 2.02 μm
- 2.5 GW/cm², overlap 100, roughness 1.91 μm
- 2.5 GW/cm², overlap 250, roughness 2.01 μm

The achieved values are all close to each other, but as expected, at the same laser power energy, a higher roughness value is obtained for higher overlap value.

All the Witwatersrand University roughness values are lower than that coming from the UPM treated coupon, but no comparison can be made, since the UPM laser parameters are not known. The residual stress field magnitude achieved, as reported in an other section of this work of thesis shows the same or a bit higher compressive RS values for coupons treated at WITS, thus making the author think the same, or similar, laser parameters have been used in both Universities.

Bibliography

- [1] International Standard. *Metallic Materials- Vickers Hardness Test- Part1: Test method*, ISO 6507-1, 2005.